



## 저작자표시-비영리-변경금지 2.0 대한민국

이용자는 아래의 조건을 따르는 경우에 한하여 자유롭게

- 이 저작물을 복제, 배포, 전송, 전시, 공연 및 방송할 수 있습니다.

다음과 같은 조건을 따라야 합니다:



저작자표시. 귀하는 원저작자를 표시하여야 합니다.



비영리. 귀하는 이 저작물을 영리 목적으로 이용할 수 없습니다.



변경금지. 귀하는 이 저작물을 개작, 변형 또는 가공할 수 없습니다.

- 귀하는, 이 저작물의 재이용이나 배포의 경우, 이 저작물에 적용된 이용허락조건을 명확하게 나타내어야 합니다.
- 저작권자로부터 별도의 허가를 받으면 이러한 조건들은 적용되지 않습니다.

저작권법에 따른 이용자의 권리는 위의 내용에 의하여 영향을 받지 않습니다.

이것은 [이용허락규약\(Legal Code\)](#)을 이해하기 쉽게 요약한 것입니다.

[Disclaimer](#)

공학박사 학위논문

**Synthesis of Tin and Cobalt  
Oxide-Carbon Nanocomposites for  
Lithium Ion Battery Anodes**

리튬이온전지 음극물질용  
산화주석 및 산화코발트-탄소  
나노복합체의 제조

2016년 2월

서울대학교 대학원

화학생물공학부

이 동 준



## **Abstract**

# **Synthesis of Tin and Cobalt Oxide-Carbon Nanocomposites for Lithium Ion Battery Anodes**

Dong Jun Lee

School of Chemical and Biological Engineering

The Graduate School

Seoul National University

Developing lithium ion battery (LIB) electrodes with high-energy-density and improved stability is of primary importance to meet the challenges in electronics and automobile industries in the near future. High-capacity anode materials, including transition metal oxides, Si, Sn, and SnO<sub>2</sub>, generally suffer from a huge volume expansion during cycling, resulting in poor stability. For commercialization, the development of a facile and scalable synthetic method should be also considered. This dissertation includes the facile fabrication of

functional hybrid nanomaterials that effectively reduce mechanical stress-induced electrode degradation.

Firstly, I report a simple synthetic method of carbon-based hybrid cellular nanosheets that exhibit outstanding electrochemical performance for many key aspects of lithium ion battery electrodes. The hybrid cellular nanosheets consisted of carbon cellular nanosheets loaded with SnO<sub>2</sub> nanoparticles. The as-synthesized carbon nanosheets have well-ordered empty cubic cells encapsulated by carbon walls. I loaded SnO<sub>2</sub> nanoparticles in the carbon cellular nanosheets by “ship-in-a-bottle” vapor deposition method and tested the performance of the resulting SnO<sub>2</sub>-carbon nanosheets as LIB anode materials. When the hybrid nanosheets are cycled, the volume expansion of SnO<sub>2</sub> is confined in the cells and the mechanical integrity is maintained, resulting in superior cycling stability. The sheet-like structure of the carbon nanosheets contributes to the short lithium ion diffusion length and facilitates electron transport through the carbon networks. As a result, the hybrid cellular nanosheet exhibited excellent battery performance, 914 mAh g<sup>-1</sup> of average capacity over 300 cycles and a capacity reduction of only 20% at a high current density of 3000 mA g<sup>-1</sup>.

Secondly, various metal (oxy)hydroxide nanoplates with hexagonal shapes were fabricated by a simple and straightforward synthetic method. For their application as LIB anodes, polydopamine is coated on the nanoplates and the resulting hybrid materials are converted to mesoporous CoO@carbon core-shell nanoplates. Through evaluation of the carbon-thickness-dependent electrochemical performance, it is concluded that a proper amount of carbon coating is necessary for preventing conversion-induced degradation and improving battery performance.

**Keywords:** lithium ion battery, anode materials, nanocomposite, metal oxide nanoparticles, energy storage.

**Student Number:** 2009-21011

# Contents

<b>Chapter 1. Introduction: Conversion Reaction Based Oxide Nanomaterials for Lithium Ion Battery Anode Materials.....</b>	<b>1</b>
1.1 Introduction.....	1
1.2 Nanostructured Metal Oxides for Lithium Ion Battery Anodes .....	6
1.2.1 Iron Oxide.....	6
1.2.2 Manganese Oxide .....	12
1.2.3 Cobalt Oxide.....	19
1.2.4 Zinc Oxide .....	30
1.2.5 Ruthenium Oxide.....	33
1.2.6 Tin Oxide .....	37
1.2.7 Mixed Metal Oxides .....	43
1.3 Summary and Outlook .....	51
1.4 References .....	55

<b>Chapter 2. Hybrid Cellular Nanosheets for High-Performance Lithium Ion Battery Anodes .....</b>	<b>75</b>
2.1 Introduction.....	75
2.2 Experimental Section .....	79
2.3 Result and Discussion .....	84
2.4 Conclusion .....	112
2.5 References .....	114
 <b>Chapter 3. Facile Synthesis of Hexagon-shaped Metal (oxy)hydroxide Nanoplates and their Applications for Lithium Ion Battery Anode Materials.....</b>	 <b>121</b>
3.1 Introduction.....	121
3.2 Experimental Section .....	125
3.3 Result and Discussion .....	129
3.4 Conclusion .....	161
3.5 References .....	163
 <b>Bibliography .....</b>	 <b>169</b>
 <b>국문 초록 (Abstract in Korean) .....</b>	 <b>175</b>



## List of Tables

<b>Table 3.1</b>	CHN elemental analysis data for CoO@C .....	151
------------------	---	-----

## List of Figures

- Figure 1.1** Schematic illustration of the conversion reaction of a metal oxide in a lithium-ion battery ..... 5
- Figure 1.2** (a) Schematic illustration of synthetic procedure for a sea urchin-like porous C-Fe<sub>3</sub>O<sub>4</sub> nanocomposite. TEM images of (b) prepared and (c) sectioned C-Fe<sub>3</sub>O<sub>4</sub> nanocomposite. (d) Cycle performance and (e) rate properties of sea urchin-like C-Fe<sub>3</sub>O<sub>4</sub> nanocomposite. (from Ref. [62] J. E. Lee, S.-H. Yu, D. J. Lee, D.-C. Lee, S. I. Han, Y.-E. Sung, T. Hyeon, *Energy Environ. Sci.* **2012**, 5, 9528)..... 11
- Figure 1.3** Schematic representation of proposed reaction mechanism of Mn<sub>3</sub>O<sub>4</sub>. (from Ref. [72] M. A. Lowe, J. Gao, H. D. Abruña, *J. Mater. Chem. A* **2013**, 1, 2094)..... 17
- Figure 1.4** (a) Schematic of preparation of Mn<sub>3</sub>O<sub>4</sub>/RGO. (b,c) TEM images of Mn<sub>3</sub>O<sub>4</sub>/RGO. (d) Rate properties of Mn<sub>3</sub>O<sub>4</sub>/RGO. (from Ref. [70] H. Wang, L.-F. Cui, Y. Yang, H. S. Casalongue, J. T. Robinson, Y. Liang, Y. Cui,

H. Dai, *J. Am. Chem. Soc.* **2010**, *132*, 13978).....18

**Figure 1.5** (a) Schematic evolution of mesoporous hollow  $\text{Co}_3\text{O}_4$  sphere and SEI formation on long-term cycling. SEM images of hollow  $\text{Co}_3\text{O}_4$  spheres (b) before cycling, (c) after 90 cycles, and (d) after 850 cycles at 1.12 C. The red dashed squares in (e) indicate the cracks in the SEI layers. The scale bars represent (b,c) 200 nm and (d) 100 nm. (e) The entire lithiation-induced reactivation process and cycling performance. (from Ref. [111] H. Sun, G. Xin, T. Hu, M. Yu, D. Shao, X. Sun, J. Lian, *Nat. Commun.* **2014**, *5*, 4526).....28

**Figure 1.6** (a) Schematic illustration of preparation of CoO/graphene hybrid. (b) Photograph and (c) TEM image of CoO/graphene hybrid. (d) Reversible lithium extraction capacity of CoO/graphene hybrid electrode at 1 A  $\text{g}^{-1}$  for 5000 cycles and (e) for 500 cycles at different temperature. (from Ref. [146] X.-l. Huang, R.-z. Wang, D. Xu, Z.-l. Wang, H.-g. Wang, J.-j. Xu, Z. Wu, Q.-c. Liu, Y. Zhang, X.-b. Zhang, *Adv. Funct. Mater.* **2013**, *23*,

4345).....29

**Figure 1.7** (a) Schematic illustrations of metal-organic framework (left) and carbon-coated ZnO quantum dots derived from a metal-organic framework (right). (b) SEM image and (c) TEM image of carbon-coated ZnO quantum dots. Inset of (c) shows corresponding SAED pattern. (d) Voltage profiles and (e) cycle performance of carbon-coated ZnO quantum dots after heat treatment at 550 °C at a current density of 75 mA g<sup>-1</sup>. (from Ref. [157] S. J. Yang, S. Nam, T. Kim, J. H. Im, H. Jung, J. H. Kang, S. Wi, B. Park, C. R. Park, *J. Am. Chem. Soc.* **2013**, *135*, 7394).....32

**Figure 1.8** Schematic representations of (a) reaction pathway and (b) the phase distribution at each stage with voltage profile for initial discharge. (from Ref. [174] Y.-Y. Hu, Z. Liu, K.-W. Nam, O. J. Borkiewicz, J. Cheng, X. Hua, M. T. Dunstan, X. Yu, K. M. Wiaderek, L.-S. Du, K. W. Chapman, P. J. Chupas, X.-Q. Yang, C. P. Grey, *Nat. Mater.* **2013**, *12*, 1130) .....36

**Figure 1.9** Sn K-edge XANES and EXAFS spectra with corresponding voltage profile taken in (a) the first discharge region, (b) the middle discharge region, (c) the last discharge region, (d) the first charge region, and (e) the last charge region of first cycle. (f) Overall electrochemical reaction mechanism of mesoporous SnO<sub>2</sub> during first two cycles. (from Ref. [183] H. Kim, G. O. Park, Y. Kim, S. Muhammad, J. Yoo, M. Balasubramanian, Y.-H. Cho, M.-G. Kim, B. Lee, K. Kang, H. Kim, J. M. Kim, W.-S. Yoon, *Chem. Mater.* **2014**, 26, 6361).....42

**Figure 1.10** Charge/discharge profiles of (a) a simple mixture of Mn<sub>3</sub>O<sub>4</sub>, Fe<sub>3</sub>O<sub>4</sub>, and Co<sub>3</sub>O<sub>4</sub>, and (b) MnFeCoO<sub>4</sub>. (c) Differential capacity curves of a simple mixture of Mn<sub>3</sub>O<sub>4</sub>, Fe<sub>3</sub>O<sub>4</sub>, and Co<sub>3</sub>O<sub>4</sub>, and MnFeCoO<sub>4</sub> during initial discharge. (from Ref. [206] H. Kim, D.-H. Seo, H. Kim, I. Park, J. Hong, K.-Y. Park, K. Kang, *Chem. Mater.* **2012**, 24, 720) (d) The first discharge curves of Mn<sub>2</sub>O<sub>3</sub>, Mn<sub>2</sub>CoO<sub>4</sub>, Mn<sub>1.5</sub>Co<sub>1.5</sub>O<sub>4</sub> and MnCo<sub>2</sub>O<sub>4</sub>. (from Ref. [207]

P. Lavela, J. L. Tirado, C. Vidal-Abarca, *Electrochim. Acta* **2007**, 52, 7986) .....48

**Figure 1.11** (a) HRTEM image of a single  $\text{Mn}_3\text{O}_4$  nanocrystal. (b-f) HRTEM images of the hollow nanostructures synthesized by the reaction of  $\text{Mn}_3\text{O}_4$  nanocrystals with 1 mL of aqueous solutions of iron (II) perchlorate having different concentrations from 0.4 M to 1.6 M. The insets of (a-f) show the corresponding FT patterns. (g) First discharge curves and corresponding differential capacities, and (h) cycle performances of carbon-coated hollow  $\text{Mn}_{3-x}\text{Fe}_x\text{O}_4$ . (from Ref. [196] M. H. Oh, T. Yu, S.-H. Yu, B. Lim, K.-T. Ko, M.-G. Willinger, D.-H. Seo, B. H. Kim, M. G. Cho, J.-H. Park, K. Kang, Y.-E. Sung, N. Pinna, T. Hyeon, *Science* **2013**, 340, 964).....49

**Figure 1.12** (a) Schematic representation of preparation of ferrite/carbon nanosheets. (b,c) TEM images of ferrite/carbon nanosheets. The inset of (c) indicates highly crystalline nature of the nanosheets. (d,e) TEM images of ferrite/carbon nanosheets after 10 cycles. (f) Cycle

performance and (g) rate properties of ferrite/carbon nanosheets. (from Ref. [197] B. Jang, M. Park, O. B. Chae, S. Park, Y. Kim, S. M. Oh, Y. Piao, T. Hyeon, *J. Am. Chem. Soc.* **2012**, *134*, 15010).....50

**Figure 2.1** (a,d) Graphic illustrations and (b,e) the corresponding TEM images of the carbon cellular nanosheets before and after etching  $\text{MnFe}_2\text{O}_4$  nanocubes. Pictures in (c,f) show that powder of the nanosheets was not attracted by a magnet after acid etching.....87

**Figure 2.2** Carbon and  $\text{SnO}_2$ -carbon cellular nanosheets. (a) SEM image, (b) TEM image and (c) cross-sectional SEM image of carbon cellular nanosheets. The scale bars in (b) and (c) are 100 and 200 nm, respectively. Schematic illustration of (d) a plant leaf, (e) its top and (f) cross-sectional structures resembling the carbon cellular nanosheets.....88

**Figure 2.3** (a) Large-area TEM image and (b) electron diffraction pattern of carbon cellular nanosheets. (c) Fast-Fourier-

transform (FFT) pattern of (a). (d) Small-angle X-ray scattering (SAXS) pattern of carbon cellular nanosheets. FFT pattern and SAXS pattern confirm the periodic mesostructure of cellular carbon nanosheets .....89

**Figure 2.4** Carbon and SnO<sub>2</sub>-carbon cellular nanosheets. (a) TEM image of a SnO<sub>2</sub>-carbon hybrid cellular nanosheet showing SnO<sub>2</sub> NPs in the cells. (b) Statistical analysis of the size of SnO<sub>2</sub> NPs (blue), side length of the cells (black), and the thickness of the carbon walls (red) .....90

**Figure 2.5** Structure analysis of carbon and SnO<sub>2</sub>-carbon cellular nanosheets. For all panels, blue indicates carbon cellular nanosheets and red represents SnO<sub>2</sub>-carbon cellular nanosheets. (a) N<sub>2</sub> adsorption-desorption isotherms and (b) the pore size distributions from the isotherm curves. (c) XRD plots. The diffraction peaks from SnO<sub>2</sub>-carbon nanosheets are indexed to tetragonal SnO<sub>2</sub>. (d) Raman spectra. The bands at around 1600 cm<sup>-1</sup> and 1360 cm<sup>-1</sup> are assigned to G and D bands of graphite structure .....93



<b>Figure 2.6</b>	Structure analysis of carbon and SnO <sub>2</sub> -carbon cellular nanosheets. For all panels, blue indicates carbon cellular nanosheets and red represents SnO <sub>2</sub> -carbon cellular nanosheets. XPS spectra from (a) Sn 3 <i>d</i> and (b) C 1 <i>s</i> . The peaks are assigned by curve fittings indicated in different colors. (c) Wide-scan XPS spectra and (d) TGA curves of hybrid cellular nanosheets (red) and carbon cellular nanosheets (blue) .....	94
<b>Figure 2.7</b>	TGA curves of hybrid cellular nanosheets with various contents of SnO <sub>2</sub> .....	95
<b>Figure 2.8</b>	(a-d) TEM images, (e) SAED pattern, and (f) XRD pattern of SnO <sub>2</sub> nanosheets. SAED and XRD pattern are well indexed to tetragonal SnO <sub>2</sub> .....	100
<b>Figure 2.9</b>	Electrochemical characterization of SnO <sub>2</sub> -carbon, carbon, and SnO <sub>2</sub> nanosheets for lithium ion battery anodes. (a) Cycling performance of the three kinds of nanosheets at a current density of 200 mA g <sup>-1</sup> . (b) Voltage profiles of SnO <sub>2</sub> -carbon nanosheets corresponding to the SnO <sub>2</sub> -	

carbon data in (a). In (b), the current density was 200 mA g<sup>-1</sup>. (c) Voltage profiles of SnO<sub>2</sub>-carbon nanosheets at three current densities in the 2nd cycle. The black profile curves in (b,c) are identical..... 101

**Figure 2.10** Initial charge-discharge voltage profiles of SnO<sub>2</sub>-carbon hybrid cellular nanosheets at a current density of 200 mA g<sup>-1</sup> ..... 102

**Figure 2.11** Electrochemical characterization of SnO<sub>2</sub>-carbon, carbon, and SnO<sub>2</sub> nanosheets for lithium ion battery anodes. (a) Cyclic voltammograms of the nanosheets. The scan rate was 0.1 mV s<sup>-1</sup>. The shift in the current peak positions is indicated with arrows. (b) *In situ* Sn K edge XANES data of SnO<sub>2</sub>-carbon and SnO<sub>2</sub> nanosheets measured during the 1st cycle at the current density of 200 mA g<sup>-1</sup> and the voltage range of 0.01–3.0 V (vs. Li<sup>+</sup>/Li). OCV indicates the XANES patterns measured just before starting the cycle..... 103

**Figure 2.12** Standard XANES data of Sn metal, SnO, and SnO<sub>2</sub> ..... 104

**Figure 2.13** TEM analysis on the structural change of hybrid cellular nanosheets. Schematics of the morphology of SnO<sub>2</sub> NPs and SnO<sub>2</sub>-based active material structure in the carbon cells (top) and TEM images of hybrid cellular nanosheets (bottom) (a) before cycling, (b) after lithiation, and (c) de-lithiation..... 107

**Figure 2.14** TEM analysis on the structural change of hybrid cellular nanosheets. TEM images of hybrid cellular nanosheets after (a) lithiation and (b) de-lithiation. TEM images of hybrid cellular nanosheets (c) before and (d) after one cycle of lithiation and de-lithiation from the same location. The red-dotted line indicates the same position on the nanosheet ..... 108

**Figure 2.15** TEM analysis on the structural change of hybrid cellular nanosheets. (a) Dark-field scanning TEM image of hybrid cellular nanosheets after 20 cycles. The inset shows TEM image after 20 cycles. (b) Dark-field scanning TEM image and (c) EDX mapping of Sn L<sub>III</sub> edge after 20 cycles. The EDX mapping was performed in the red-

dotted square in (b) .....	109
<b>Figure 2.16</b> Illustration of a SnO <sub>2</sub> -carbon hybrid cellular nanosheet and its features that contribute to the electrochemical performance .....	111
<b>Figure 3.1</b> (a) TEM and (b) high-resolution TEM image of hexagon-shaped Co(OH) <sub>2</sub> nanoplates. (c) Selected-area electron diffraction (SAED) pattern of a single nanoplate. (d) XRD data of Co(OH) <sub>2</sub> nanoplates .....	134
<b>Figure 3.2</b> TEM images of metal (oxy)hydroxide nanoplates with various combination. (a) Mn, (b) Fe, (c) Mg, (d) Co-Mn, (e) Co-Fe, (f) Mn-Fe, (g) Co-Mg, (h) Co-Mn-Fe, (i) Co-Mn-Fe-Mg. Scale bars in (a-i) indicate 100 nm .....	135
<b>Figure 3.3</b> XRD data of various metal (oxy)hydroxide nanoplates. (a) Mn, (b) Fe, (c) Mg, (d) Co-Mn, (e) Co-Fe, (f) Mn-Fe, (g) Co-Mg, (h) Co-Mn-Fe, and (i) Co-Mn-Fe-Mg .....	136
<b>Figure 3.4</b> (a-c) TEM image and (d-f) XRD data of nanoparticles obtained under an air atmosphere. (a,d) Cobalt, (b,e)	

	manganese, and (c,f) iron. Scale bars in (a-c) indicate 200nm.....	137
<b>Figure 3.5</b>	Dark-field STEM image and corresponding EDX elemental mapping images of various mixed-metal (oxy)hydroxide nanoplates. (a) Co-Mn, (b) Co-Fe, (c) Mn-Fe, and (d) Co-Mg.....	138
<b>Figure 3.6</b>	Dark-field STEM image and corresponding EDX elemental mapping images of various mixed-metal (oxy)hydroxide nanoplates. (a) Co-Mn-Fe and (b) Co- Mn-Fe-Mg.....	139
<b>Figure 3.7</b>	TEM image, SAED pattern, and corresponding EFTEM images of mixed-metal (oxy)hydroxide nanoplates. (a) Co-Mn and (b) Co-Fe.....	140
<b>Figure 3.8</b>	TEM image, SAED pattern, and corresponding EFTEM images of mixed-metal (oxy)hydroxide nanoplates. (a) Mn-Fe and (b) Co-Mg.....	141
<b>Figure 3.9</b>	TEM image, SAED pattern, and corresponding EFTEM	

images of mixed-metal (oxy)hydroxide nanoplates. (a) Co-Mn-Fe and (b) Co-Mn-Mg .....	142
<b>Figure 3.10</b> TEM image, SAED pattern, and corresponding EFTEM images of mixed-metal (oxy)hydroxide nanoplates. (a) Mn-Fe-Mg and (b) Co-Mn-Fe-Mg .....	143
<b>Figure 3.11</b> (a-c) TEM image of Co(OH) <sub>2</sub> @polydopamine with (a) 1.5 nm, (b) 3.8 nm, and (c) 6.5 nm. (d-f) TEM image of (d) CoO@C-1, (e) CoO@C-2, (f) CoO@C-3 after heat treatment. Scale bars in (a-f) indicate 50 nm .....	148
<b>Figure 3.12</b> (a-f) TEM images of Co(OH) <sub>2</sub> @polydopamine core-shell nanoplates with various thickness of polydopamine shell. Scale bars in (a-f) indicate 50 nm .....	149
<b>Figure 3.13</b> XRD patterns of CoO@C with various carbon shell thickness .....	150
<b>Figure 3.14</b> Large-scale synthesis of CoO@C-3. From a single batch, ~1.5 g of CoO@C could be obtained .....	152
<b>Figure 3.15</b> N <sub>2</sub> adsorption and desorption isotherm and pore size	

distribution of (a) CoO@C-1, (b) CoO@C-2, and (c) CoO@C-3.....	153
--	-----

<b>Figure 3.16</b> Electrochemical performances of CoO@C-1, CoO@C-2, and CoO@C-3. (a) Cycling performance at a current density of 200 mA g <sup>-1</sup> . (b) Rate performance at various current densities from 100 to 1600 mA g <sup>-1</sup> .....	158
--	-----

<b>Figure 3.17</b> (a-f) TEM images of (a-c) CoO@C-1 and (d-f) CoO@C-3 after 50 cycles. (g) Dark-field STEM image and elemental mapping of (h) Co K edge and (i) oxygen K edge of CoO@C-3 after cycles .....	159
--	-----

<b>Figure 3.18</b> Cycling performance and TEM image of (a) MnO@C and (b) Fe <sub>3</sub> O <sub>4</sub> @C .....	160
---	-----

# **Chapter 1. Introduction:**

## **Conversion Reaction Based Oxide Nanomaterials for Lithium Ion Battery Anode Materials**

### **1.1 Introduction**

Over the past two decades, rechargeable lithium ion batteries (LIBs) have become one of the most important power sources for portable electronic devices because LIBs exhibit many advantageous features including long life span, high reaction voltage, low self-discharge, wide temperature window, and lack of a memory effect.<sup>[1-5]</sup> Recently, they have also been incorporated into the development of hybrid electric vehicles (HEVs), plug in hybrid electric vehicles (PHEVs), and electric vehicles (EVs).<sup>[4-6]</sup> To be commercially successful in various EVs and to meet the increasing energy and performance expectations in electronic devices, LIBs should have increased energy densities. The most straightforward way to accomplish this objective is to develop high-voltage cathodes and high-capacity anodes.<sup>[7-13]</sup> However, developing high-voltage cathodes (~5.0 V) is extremely



challenging because conventional organic electrolytes are unstable at the high voltages.<sup>[7,8]</sup> Consequently, tremendous efforts have been devoted to developing high-capacity anode materials for LIBs.<sup>[9-13]</sup> Various nanomaterials, including  $\text{Li}_4\text{Ti}_5\text{O}_{12}$  and  $\text{SnO}_2$  nanoparticles, have been employed as anode materials, and some have shown superior electrochemical properties.<sup>[14-20]</sup> Among them, nanostructured transition metal oxides such as iron oxide and manganese oxide have attracted a great deal of attention due to their high theoretical capacity since the early 2000s.<sup>[21-24]</sup> The reaction between lithium and nano-sized transition metal oxides, the so-called “conversion reaction,” is shown in Equation 1.

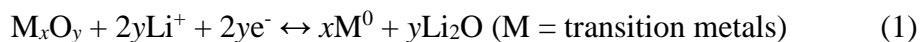


**Figure 1.1** shows a schematic illustration of the conversion reaction of transition metal oxides for LIB anodes. From Equation 1,  $2y$  lithium ions can be stored per formula unit of metal oxide through a conversion reaction, causing a structural change and amorphization of transition metal oxides that involves large volume expansion. At the end of lithiation, nanoscale transition metal clusters are embedded in the lithium oxide ( $\text{Li}_2\text{O}$ ) matrix. During de-lithiation, these transition metal clusters are oxidized to form amorphous transition metal oxide.

The theoretical capacity ( $q$ ) of the electrode materials can be described as follows:

$$q = Q_m/m \quad (2)$$

where  $Q_m$  is the total quantity of charge that can be stored in an electrode molecule, and  $m$  is the molecular weight (g) of the electrode materials. Because  $Q_m$  can be obtained by multiplying the number of moles of stored electrons ( $n$ , which is equal to  $2y$  in Equation 1) and the Faraday constant ( $F = 96485 \text{ C mol}^{-1} = 26801 \text{ mAh mol}^{-1}$ ), Equation 2 can be converted as follows.

$$q = nF/m = 26801(n/m) [\text{mAh g}^{-1}] \quad (3)$$

Most conversion reaction-based transition metal oxides have much higher theoretical capacities than graphite ( $372 \text{ mAh g}^{-1}$ ), and some can exceed  $1000 \text{ mAh g}^{-1}$ . Despite the high theoretical capacity, conversion reaction-based oxide nanomaterials should be further optimized to overcome other unsatisfactory electrochemical properties including voltage hysteresis.<sup>[22,23]</sup> A difference in voltages exists between the discharge and charge profiles, causing huge round-trip energy density inefficiency. In addition, very large volume changes occur during charge and discharge leading to cycle fading. A low initial Coulombic efficiency and rate capability should also be

improved. Exploitation of nanostructured materials can effectively alleviate the strain derived from the volume change, resulting in enhanced specific capacity retention. Furthermore, nanostructured materials can provide large electrode–electrolyte contact areas and shorten diffusion length of lithium ion in the active materials, leading to a high rate capability.<sup>[24-29]</sup> To address these issues, various metal oxide nanostructures having many different morphologies and compositions have been investigated as LIB anodes. In chapter I, I summarize recent progress on the development of nanostructured metal oxides for LIB anodes. All potentials in this review are given versus  $\text{Li}^+/\text{Li}$ .

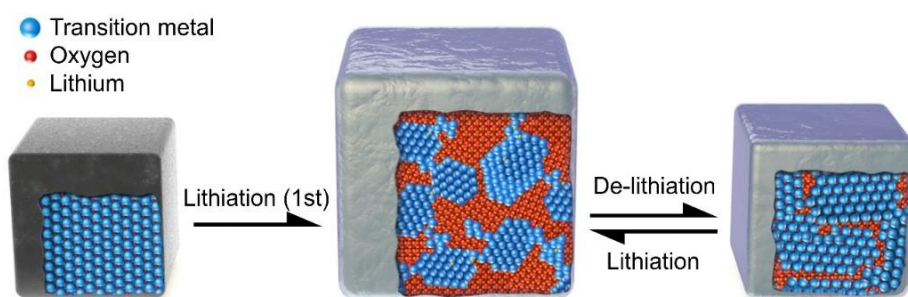


**Figure 1.1.** Schematic illustration of the conversion reaction of a metal oxide in a lithium-ion battery.

## 1.2 Nanostructured Metal Oxides for Lithium Ion Battery Anodes

### 1.2.1 Iron Oxide

Iron oxide has attracted much attention as anode materials for LIBs because of its very high theoretical capacity (924 mAh g<sup>-1</sup> for Fe<sub>3</sub>O<sub>4</sub> and 1007 mAh g<sup>-1</sup> for Fe<sub>2</sub>O<sub>3</sub>), low cost, and environmental benignity. Conversion reactions in iron oxide were first observed in the 1980s using molten salt electrolytes.<sup>[30]</sup> However, the electrochemical reversibility of these electrodes was much lower than the theoretical expectation. A breakthrough occurred in the 2000s that improved the electrochemical reversibility when nanometer-scale iron oxide was introduced.<sup>[21]</sup>

The  $\alpha$ -Fe<sub>2</sub>O<sub>3</sub> (hematite) and Fe<sub>3</sub>O<sub>4</sub> (magnetite) are the most explored iron oxides. The conversion reaction involves severe structural reorganization and volumetric changes.<sup>[31]</sup> As shown in a typical voltage profile of iron oxide, a plateau at about 0.8 V corresponding to the full reduction of FeO<sub>x</sub> to a Fe<sup>0</sup>/Li<sub>2</sub>O mixture occurs followed by electrolyte decomposition that provides additional capacity and interfacial storage.<sup>[32]</sup> Moreover, the initial cycle exhibits

a different profile from subsequent cycles, which is related to activation processes and an irreversible capacity loss.

Various shaped  $\alpha$ -Fe<sub>2</sub>O<sub>3</sub> nanostructures have been evaluated to improve the electrochemical properties. Hollow nanostructured  $\alpha$ -Fe<sub>2</sub>O<sub>3</sub> has been shown enhanced electrochemical performances while alleviating volume expansion during cycling effectively.<sup>[33-42]</sup> Hard templates (silica<sup>[33]</sup>) and soft templates (organic nanotube,<sup>[34]</sup> quasi-emulsion,<sup>[36]</sup> and metal-organic-framework<sup>[37,38]</sup>) have been utilized frequently followed by etching processes, such as calcination or soaking, to create hollow interior structures.  $\alpha$ -Fe<sub>2</sub>O<sub>3</sub> microboxes derived from Prussian blue microcubes exhibited a reversible capacity of 945 mAh g<sup>-1</sup> after 30 cycles.<sup>[38]</sup> However, hollow structures sacrifice volumetric specific capacities due to low tap densities of active materials. Therefore, a thick electrode with a high mass loading is needed, but a thick electrode makes it difficult to provide effective electrical pathway during cycling.

Another strategy for enhancing battery performance is making composites with carbonaceous materials. Carbon can provide mechanical strength against deformation and act as electron-transfer channels between the current collector and active materials. Moreover,

a carbon coating on the electrode surface can prevent excessive formation of a solid electrolyte interphase (SEI) layer.<sup>[42]</sup> Many  $\alpha$ -Fe<sub>2</sub>O<sub>3</sub> compounds and carbon structures, such as reduced graphene oxide (RGO),<sup>[43]</sup> carbon nanotubes (CNTs),<sup>[44]</sup> and carbon matrices,<sup>[45,46]</sup> showed good battery performance, including capacity retention and rate capability.

Mesoporous  $\alpha$ -Fe<sub>2</sub>O<sub>3</sub> nanostructures also have been employed as anode materials. Mesoporous silica NPs<sup>[47]</sup> and metal-organic frameworks (MOF)<sup>[48]</sup> are typically used as templates. For example, mesoporous  $\alpha$ -Fe<sub>2</sub>O<sub>3</sub> prepared using an Fe-containing MOF exhibited a capacity of 911 mAh g<sup>-1</sup> after 50 cycles at a 0.2 C-rate.<sup>[49]</sup> The capacity of mesoporous  $\alpha$ -Fe<sub>2</sub>O<sub>3</sub> increased slowly during the initial cycles. This increase might be caused by the reversible formation of a gel-like layer at low potentials,<sup>[50]</sup> or incomplete de-conversion reactions owing to the presence of electrically disconnected regions in the electrode.<sup>[22]</sup> A capacity of 424 mAh g<sup>-1</sup> was achieved when cycled at 10 C.  $\alpha$ -Fe<sub>2</sub>O<sub>3</sub> nanostructures deposited on current collectors, such as copper<sup>[50]</sup> and nickel foil,<sup>[51]</sup> have been also evaluated for LIB anodes. These nanostructures maintain direct electric contact with current collectors, allowing omission of carbon additives in the

electrode. There are still limitations in the film thickness, however, resulting in a low volumetric specific capacity.

Magnetite has problems similar to other conversion reaction-based transition metal oxides, including volume expansion, excessive SEI formation, and low Coulombic efficiency. Hence, various nanostructures have been tested to overcome these problems. Such nanostructures include hollow structures,<sup>[52]</sup> mesoporous structures,<sup>[53]</sup> nanocomposites with graphene,<sup>[54-57]</sup> carbon nanotubes,<sup>[58,59]</sup> carbon matrixes,<sup>[60-66]</sup> and nanostructures deposited on metal current collectors.<sup>[67]</sup> Lee *et al.* reported that excessive SEI formation can be minimized by changing the geometric configuration.<sup>[54]</sup> 10-nm-sized iron oxide NPs<sup>[68]</sup> are assembled to secondary particles and calcined in an inert gas to form mesoporous iron oxide nanoparticle clusters (MIONCs). By comparing the electrochemical properties with random aggregates of iron oxide nanoparticles (RAIONs), the MIONCs exhibited enhanced cyclic stability and Coulombic efficiency. The MIONCs exhibited a thin and compact SEI layer on their surfaces and maintained their original morphology even after 20 cycles, while RAIONs were buried under an excessive SEI layer.

Although diverse hierarchical nanostructures have been



synthesized via a template method, they require complicated procedures including fabrication of templates, impregnation of precursors, and removal of template. It remains a challenge to develop facile and scalable syntheses of hierarchical nanostructures. A hierarchical C/Fe<sub>3</sub>O<sub>4</sub> nanocomposite has been developed by a simple one-pot reaction.<sup>[63]</sup> The synthetic route involves mixing of iron chloride with sodium dodecyl sulfate (SDS) solution, followed by addition of pyrrole without any washing steps (**Figure 1.2a**). The residual Fe<sup>3+</sup> ions acted as an oxidant for polymerization of pyrrole. After calcination in argon, the resulting C/Fe<sub>3</sub>O<sub>4</sub> nanocomposite exhibited a sea urchin-like morphology with diameters of hundreds of nanometers (**Figure 1.2b**). The interior of the C/Fe<sub>3</sub>O<sub>4</sub> nanocomposite was composed of a nanoporous structure with irregular nano-sized subunits (**Figure 1.2c**). The C/Fe<sub>3</sub>O<sub>4</sub> nanocomposite showed a capacity of 800–1000 mAh g<sup>-1</sup> at a current of 100 mA g<sup>-1</sup> up to 100 cycles, demonstrating high reversibility (**Figure 1.2d**). At an increasing current of 2500 mA g<sup>-1</sup>, the C/Fe<sub>3</sub>O<sub>4</sub> nanocomposite delivered 418 mAh g<sup>-1</sup> (**Figure 1.2e**).

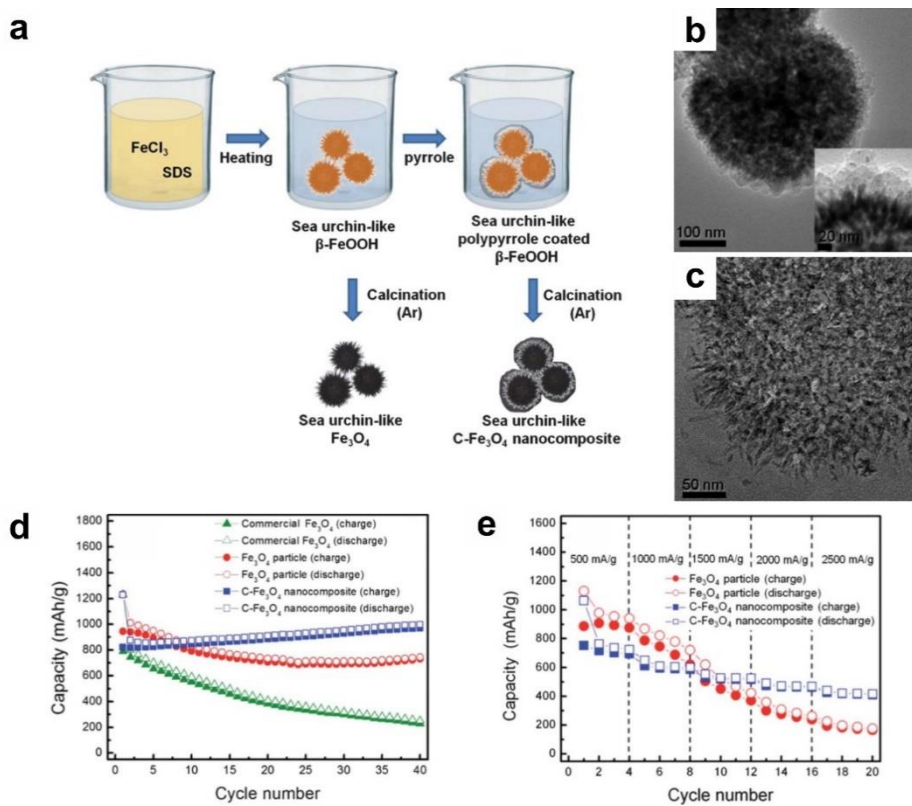


**Figure 1.2.** (a) Schematic illustration of synthetic procedure for a sea urchin-like porous C-Fe<sub>3</sub>O<sub>4</sub> nanocomposite. TEM images of (b) prepared and (c) sectioned C-Fe<sub>3</sub>O<sub>4</sub> nanocomposite. (d) Cycle performance and (e) rate properties of sea urchin-like C-Fe<sub>3</sub>O<sub>4</sub> nanocomposite. (from Ref. [62] J. E. Lee, S.-H. Yu, D. J. Lee, D.-C. Lee, S. I. Han, Y.-E. Sung, T. Hyeon, *Energy Environ. Sci.* **2012**, 5, 9528)

### 1.2.2 Manganese Oxide

Manganese oxide has been investigated because of its high theoretical specific capacity, low reaction potential (0.2–0.5 V during the initial discharge),<sup>[22]</sup> and low voltage hysteresis (<0.8 V) compared with other transition metal oxides.<sup>[69]</sup> Manganese oxide has a variety of crystallographic structures, which include cubic rock salt (MnO, 756 mAh g<sup>-1</sup>), inverse spinel (Mn<sub>3</sub>O<sub>4</sub>, 937 mAh g<sup>-1</sup>), hexagonal corundum (Mn<sub>2</sub>O<sub>3</sub>, 1019 mAh g<sup>-1</sup>), and a manganese dioxide structure (MnO<sub>2</sub>, 1223 mAh g<sup>-1</sup>).<sup>[24]</sup> Although manganese oxide has many advantages for use as an anode in LIBs, fully utilization of manganese oxide is difficult. Manganese oxide has extremely low electrical conductivity ( $\sim 10^{-7}$ – $10^{-8}$  S/cm for Mn<sub>3</sub>O<sub>4</sub>) that hampers its usage and commercialization as an electrode material.<sup>[70]</sup>

Understanding the reaction mechanism during charge/discharge cycling is very important for improving electrode stability as mentioned in the previous section. However, the structural and chemical changes during a conversion reaction make it difficult to investigate the reaction mechanism. In addition, the sensitivity of the reaction intermediates and products to ambient conditions impose limitations on *ex situ* techniques. Therefore, various *in situ* techniques

such as *in situ* transmission electron microscopy (TEM),<sup>[71]</sup> X-ray diffraction (XRD),<sup>[72]</sup> X-ray absorption spectroscopy (XAS),<sup>[73]</sup> and X-ray tomography,<sup>[74]</sup> have been recently adopted that reveal the events occurring during cycling. Lowe *et al.* analyzed the conversion reaction in a  $\text{Mn}_3\text{O}_4$  electrode using *in operando* XRD and XAS techniques and proposed the mechanism depicted in **Figure 1.3**. Zhang *et al.* investigated the morphology, mechanical strength, and the formation of SEI on a MnO film at different states of charge/discharge using atomic force microscopy and force spectroscopy.<sup>[75]</sup> It is noteworthy that the distribution of the SEI layer on the electrode surface was highly inhomogeneous and proper strategies to achieve controllable SEI layers can be developed by means of different nanomaterial synthetic methods.

A variety of manganese oxide nanostructures have been fabricated and tested in pursuit of high battery performance and stable cycling. Construction strategies are similar to those mentioned for iron oxide, including manganese oxide nanocomposites combined with conducting materials, such as carbon,<sup>[76-88]</sup> CNTs,<sup>[89-91]</sup> graphene,<sup>[92-96]</sup> N-doped carbon,<sup>[97-101]</sup> and reduced graphene oxide (RGO).<sup>[102-104]</sup> Controlling the morphology of manganese oxide has also been

demonstrated on mesoporous<sup>[73,105-108]</sup> and hollow structures.<sup>[109,110]</sup> Interestingly, some reports showed a U-shaped capacity and cycle number plots, in which the capacity decreased during the first few cycles and then increased slowly upon additional cycling.<sup>[79,97]</sup> In some cases, the capacity at the last cycle was much higher than the initial capacity.<sup>[94]</sup> This cycling behavior can be attributed to several factors including lithiation-induced reactivation<sup>[111]</sup> and generation of  $\text{Mn}^{4+}$  during the charge process. The latter occurs because  $\text{Mn}^{2+}$  was partly re-oxidized to a higher oxidation state.<sup>[77]</sup>

$\text{Mn}_3\text{O}_4$  has a much lower electrical conductivity than  $\text{Co}_3\text{O}_4$  and  $\text{Fe}_3\text{O}_4$ . In order to increase the electrical conductivity of  $\text{Mn}_3\text{O}_4$ ,  $\text{Mn}_3\text{O}_4$  NPs were grown on RGO using a two-step solution-phase method, resulting in the formation of  $\text{Mn}_3\text{O}_4$ -RGO hybrid material (**Figure 1.4a**).<sup>[70]</sup> About 10–20 nm-sized  $\text{Mn}_3\text{O}_4$  NPs with high crystallinity were uniformly distributed on the RGO sheets (~10 wt%) (**Figure 1.4b,c**). A specific capacity of about 810 mAh g<sup>-1</sup> was delivered at a current density of 40 mA g<sup>-1</sup> after 50 cycles (**Figure 1.4d**), which can be attributed to innate interactions between the graphene substrates and  $\text{Mn}_3\text{O}_4$  NPs. Moreover, good dispersion of the  $\text{Mn}_3\text{O}_4$  NPs on the RGO sheets can prevent aggregation during

cycling, which can facilitate the movement of charge carriers from current collectors through highly conducting 3D graphene networks.

Mn<sub>2</sub>O<sub>3</sub> has interesting properties for its use as an anode material for LIBs, such as a high theoretical capacity (1019 mAh g<sup>-1</sup>) and a relatively low operating voltage (average discharge voltage at 0.5 V and charge voltage at 1.2 V). These features can result in a higher energy density than that of other transition metal oxide-based anode materials. However, the low intrinsic conductivity of Mn<sub>2</sub>O<sub>3</sub> can cause poor capacity retention and low rate capability. To address this issue, various types of mesoporous Mn<sub>2</sub>O<sub>3</sub> nanostructures have been explored as anode materials<sup>[112-115]</sup> because large size voids can facilitate lithium ion diffusion and electrolyte access. Porous Mn<sub>2</sub>O<sub>3</sub> nanostructures were mainly synthesized by morphology-conserved phase transformation from Mn-containing precursors, such as MnCO<sub>3</sub>,<sup>[116]</sup> Mn(OH)<sub>2</sub>,<sup>[117]</sup> and Mn-glycolate.<sup>[118]</sup> Among these nanostructures, porous Mn<sub>2</sub>O<sub>3</sub> nanoplates retained a capacity of 813 mAh g<sup>-1</sup> after 50 cycles at a current density of 100 mA g<sup>-1</sup>, whereas the capacity of the bulk Mn<sub>2</sub>O<sub>3</sub> powder electrode degraded rapidly.<sup>[118]</sup> The improved electrochemical performance of the porous Mn<sub>2</sub>O<sub>3</sub> nanoplates can be attributed to the thin plate morphology and porous

structure. The thin plate morphology can provide abundant surface sites for electrochemical reactions and thereby increase specific capacity, while the porous structure can alleviate the electrode polarization during the discharge-charge process and thereby enhance the rate capability and capacity retention.

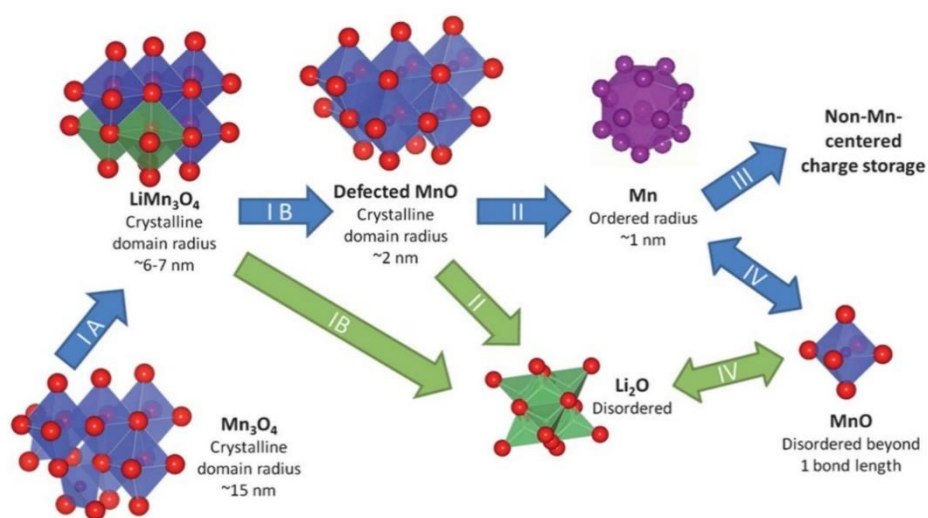


**Figure 1.3.** Schematic representation of proposed reaction mechanism of  $\text{Mn}_3\text{O}_4$ . (from Ref. [72] M. A. Lowe, J. Gao, H. D. Abruña, *J. Mater. Chem. A* **2013**, *1*, 2094)



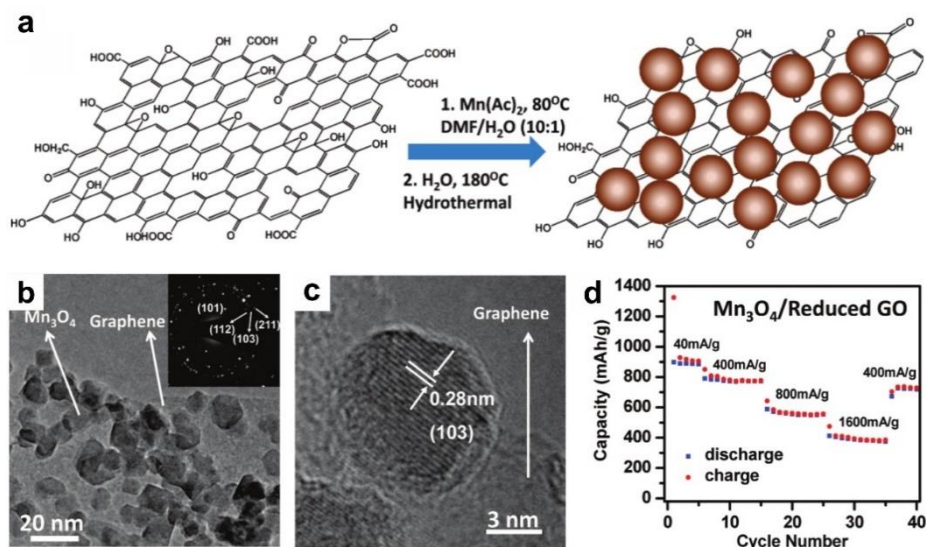
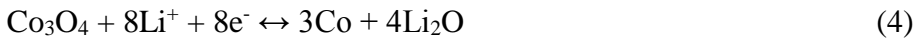


**Figure 1.4.** (a) Schematic of preparation of  $\text{Mn}_3\text{O}_4/\text{RGO}$ . (b,c) TEM images of  $\text{Mn}_3\text{O}_4/\text{RGO}$ . (d) Rate properties of  $\text{Mn}_3\text{O}_4/\text{RGO}$ . (from Ref. [70] H. Wang, L.-F. Cui, Y. Yang, H. S. Casalongue, J. T. Robinson, Y. Liang, Y. Cui, H. Dai, *J. Am. Chem. Soc.* **2010**, *132*, 13978)

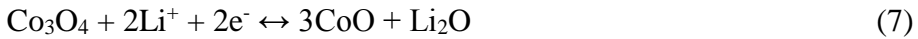
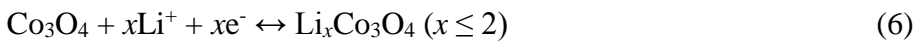
### 1.2.3. Cobalt Oxide

CoO and Co<sub>3</sub>O<sub>4</sub> are the main phases used as anode materials, in which the theoretical capacities are 715 and 890 mAh g<sup>-1</sup>, respectively.<sup>[119,120]</sup> The overall reactions for these two phases during cycling are shown in Equations 4 and 5.



These reactions induce large volume expansions of about 100%,<sup>[121]</sup> which cause the agglomeration of active materials and a deterioration of mechanical integrity leading to poor capacity retention. Voltage plateaus for the Co<sub>3</sub>O<sub>4</sub> electrode are observed at 1.3/0.8 V and 2.2 V during initial discharge and charge, respectively.<sup>[122]</sup> In the case of the CoO electrode, voltage plateaus during initial discharge and charge occur at 0.7 and 2.1 V, respectively.<sup>[119]</sup>

Many attempts have been made to discover the lithiation/de-lithiation pathway using a variety of methods. Larcher *et al.* reported that there are two different pathways during initial lithiation of Co<sub>3</sub>O<sub>4</sub>. These two pathways are described in Equations 6 and 7.<sup>[121]</sup>



They demonstrated that the lithiation pathway is governed by the morphology of the active materials and cycling conditions, such as current density and cycling temperature. During the first discharge, formation of lithium-inserted  $\text{Li}_x\text{Co}_3\text{O}_4$  is favored in large-sized  $\text{Co}_3\text{O}_4$  (higher on-surface current densities), while the smaller crystal sizes (lower current densities) lead to intermediate formation of  $\text{CoO}$ . Structural evolution and reaction pathways were also studied by *in situ* TEM.<sup>[123,124]</sup> Luo *et al.* reported atomic resolution observation of lithiation- and de-lithiation-induced phase conversion of 5 nm-sized  $\text{Co}_3\text{O}_4$  nanocubes.<sup>[123]</sup> In the early stage of lithiation, lithium ions diffuse into the spinel crystal structure, forming Li-intercalated  $\text{Li}_x\text{Co}_3\text{O}_4$  resulting in a small volume expansion (about 20%). Interestingly, this microscopic observation is consistent with Equation 6, as previous reports discovered. As more lithium ions are inserted into  $\text{Co}_3\text{O}_4$ , the lattice fringe disappears, indicating the amorphization of  $\text{Co}_3\text{O}_4$  and the conversion to small Co-Li-O clusters. In the final phase, the Co-rich clusters are further reduced, and Co metal clusters and  $\text{Li}_2\text{O}$  crystals nucleate and grow simultaneously. Co metal clusters are then interconnected and embedded into the  $\text{Li}_2\text{O}$  matrix.

For conversion reaction-based nanostructured metal oxides, a

gradual increase in capacity during the first few cycles is often observed. This capacity increase is more often observed in cobalt oxide. Sometimes unexpectedly high capacities exceeding the theoretical capacity were achieved for oxide materials. This phenomenon seems to occur owing to the following reasons such as formation of polymer/gel-like films,<sup>[125]</sup> defect-induced storage of lithium ions,<sup>[126]</sup> improved kinetics resulting from oxidation states higher than the initial state,<sup>[97]</sup> and capacitive behavior at the interface between metal nanoparticles and  $\text{Li}_2\text{O}$ .<sup>[127]</sup> It has been widely accepted that polymer/gel-like film can participate in reversible lithium storage and is a dominant factor to increase the capacity.<sup>[128]</sup> Such films are formed by electrochemically driven ring-opening polymerization of electrolytes,<sup>[125]</sup> and the polymerization activity will depend on the metal species. Thus, cobalt oxide might result in a large increase in the capacity because of its high catalytic activity compared with other metal species. Although the exact mechanism for these events remains unclear, studies are underway seeking to better understand the mechanisms, which should give new insights into the fabrication of anode materials with enhanced electrochemical performance.

Due to their attractive properties, various nanostructured cobalt

oxides have been developed. Wang *et al.* synthesized a highly ordered mesoporous  $\text{Co}_3\text{O}_4$  nanostructure using KIT-6 mesoporous silica as a hard template. These materials exhibited a high specific capacity of about  $1200 \text{ mAh g}^{-1}$  at a current density of  $50 \text{ mA g}^{-1}$  and  $700 \text{ mAh g}^{-1}$  at  $300 \text{ mA g}^{-1}$  at 100 cycles.<sup>[129]</sup> Wang *et al.* reported a facile synthesis of a  $\text{Co}_3\text{O}_4$  nanobelt array on titanium foil through thermal treatment of cobalt carbonate hydroxide nanobelts synthesized by a hydrothermal method.<sup>[130]</sup> The resulting nanobelt array delivered a reversible capacity greater than  $700 \text{ mAh g}^{-1}$  after 30 cycles. In addition, diverse  $\text{Co}_3\text{O}_4$  nanostructures, including nanowire/fibers/rods,<sup>[131-134]</sup> nanotubes,<sup>[122]</sup> hollow microspheres,<sup>[111,135-137]</sup> nanosheet/plates,<sup>[138,139]</sup> porous nanocapsules,<sup>[140]</sup> agglomerated nanoparticles,<sup>[141]</sup> and nanocages<sup>[142]</sup> have been investigated as LIB anodes.

Recently, Wang *et al.* reported a synthesis method for multishelled  $\text{Co}_3\text{O}_4$  hollow microspheres using polysaccharide-based carbonaceous microspheres and the hydrated cobalt ion ( $[\text{Co}(\text{H}_2\text{O})_6]^{2+}$ ) as a sacrificial template and precursor, respectively. These microspheres showed superior electrochemical performance in terms of capacity.<sup>[135]</sup> The number of shells in multi-shelled hollow spheres

are precisely controlled by varying the number of coordinated aquo groups within the cobalt ion ( $[\text{Co}(\text{H}_2\text{O})_x]^{2+}$ ,  $x = 3-6$ ), which changes the diffusion rate of the cobalt ion. Among multi-shelled hollow microspheres with a shell number range of 1 to 4, triple-shelled  $\text{Co}_3\text{O}_4$  microspheres showed a promising capacity of  $1616 \text{ mAh g}^{-1}$  at 30 cycles. This incredibly high capacity resulted from a combination of porous architecture, high surface area, and the interior cavities of multi-shelled microspheres.

When cycle number increases, the capacity of a cell monotonically decreases because electrode materials suffer from mechanical degradation. These ‘dead’ cells cannot be restored to their original functionality. However, it has been reported that this degradation can be controlled to restructure the mesoporous architecture of mesoporous  $\text{Co}_3\text{O}_4$  hollow spheres, and stabilize the SEI layer by high-rate lithiation-induced reactivation.<sup>[111]</sup> **Figure 1.5a** represents a schematic illustration of this reactivation process. During the first 90 cycles, the materials suffer from enormous capacity fading (**Figure 1.5e**). During this stage, the SEI layer repeatedly fragments, exfoliates, and changes its form, which makes the SEI layer thick and unstable. **Figure 1.5c** shows that SEI layers were cracked and very

thick due to repeated mechanical destruction and reformation. Surprisingly, after capacity fading, continuous lithiation at a high current density stimulated the reactivation of the electrode materials, gradually raising the specific capacity during the following cycles without any significant degradation. The scanning electron microscope (SEM) image in **Figure 1.5d** shows that the lithiation-induced reactivation process makes the SEI layer thinner and stable leading to a smooth and completely encapsulated SEI layer after 850 cycles.

As discussed in previous sections, it is widely accepted that the electrochemical performance of nanostructured metal oxides can be enhanced by making composites with carbonaceous materials that can accommodate volume changes and act as a current collector. For these reasons, cobalt oxide-based composites with various carbon substrates such as graphene,<sup>[143-149]</sup> carbon nanotubes,<sup>[150,151]</sup> mesoporous carbon,<sup>[152]</sup> and amorphous carbon,<sup>[153-155]</sup> have been developed. However, more precise control is needed to directly synthesize cobalt oxide nanoparticle-carbon composites because cobalt is easily reduced. Approaches to fabricate metal oxide-carbon nanocomposites include heat treatment of various inorganic–organic conjugated precursors.

This approach has been applied for other metal oxides.<sup>[98,156,157]</sup> However, when a cobalt-organic precursor is heated in inert gas or vacuum conditions, cobalt oxides are reduced to metallic Co via a carbothermal reduction process accompanied by the simultaneous conversion of the organic precursor to carbon. This process results in the formation of a Co-carbon nanocomposite rather than a cobalt oxide-carbon composite.<sup>[153,154]</sup> Although the activation temperature for carbothermal reduction of cobalt oxide is expected to be over 750 °C,<sup>[158]</sup> the high surface energy of the nanoparticles enabled them to be reduced at a temperature lower than 750 °C. After an oxidation step, the Co-carbon composite was converted to the cobalt oxide-carbon composite, which could be utilized as an anode material.

When a battery electrode is fabricated, active materials are mixed with conducting carbon and binder to enhance electrical conductivity and mechanical integrity, respectively. Normally, only a few weight percentage of these additives is typically incorporated into the micro-sized materials. However, over ten percent of additives should be added for nanomaterials because of their high surface area. The capacity of the whole electrode actually decreased, however, when this addition was done. Consequently, additive-free electrodes are



highly attracted for nanostructured materials. **Figure 1.6a** shows a schematic representation of the synthesis of a binder-free CoO-graphene composite electrode.<sup>[146]</sup> First,  $\alpha$ -Co(OH)<sub>2</sub> nanosheets with a thickness of ~2.6 nm are synthesized and mixed with graphene oxide prepared by Hummer's method.<sup>[159]</sup> Note that positively-charged  $\alpha$ -Co(OH)<sub>2</sub> nanosheets electrostatically interact with negatively-charged graphene oxide, producing a composite. When the composites are refluxed under reducing conditions, reduction of graphene oxide and growth/transformation of Co(OH)<sub>2</sub> occurs simultaneously, resulting in a  $\beta$ -Co(OH)<sub>2</sub>-graphene composite. Interestingly,  $\beta$ -Co(OH)<sub>2</sub> is completely coated on graphene due to electrostatic interactions. After drop-coating, drying, and sintering, binder-free CoO-graphene hybrid composites are fabricated on a Cu foil. The hybrid composite does not detach from the Cu foil even after bending, indicating that it has good adhesion and structural stability (**Figure 1.6b**). **Figure 1.6c** shows that CoO is uniformly and completely coated on graphene. Binder-free CoO-graphene hybrid composites have excellent electrochemical performance, showing capacities over 600 mAh g<sup>-1</sup> at a high current density of 1 A g<sup>-1</sup>, even after 5000 cycles, owing to its two-dimensional architecture and stable mechanical integrity (**Figure 1.6d**).

During discharge, CoO is converted to Co metallic clusters that are a few nanometers in size and  $\text{Li}_2\text{O}$ , and the reduced metallic clusters and highly conductive graphene layer might facilitate the good rate performance. As shown in **Figure 1.6e**, CoO-graphene hybrid composites exhibit high cycling stability at various operating temperatures from 0 to 55°C.

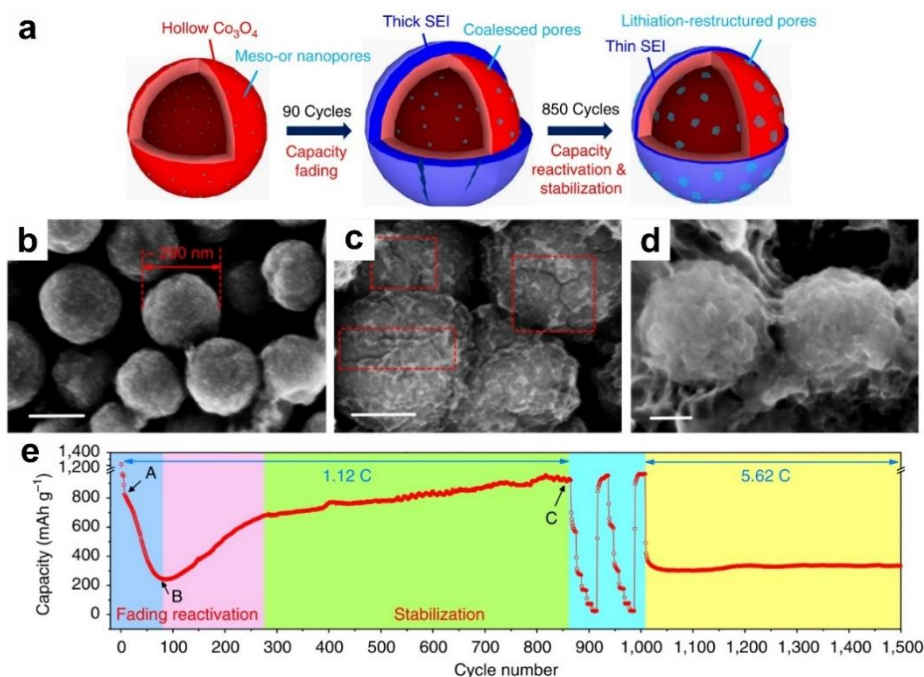


**Figure 1.5.** (a) Schematic evolution of mesoporous hollow  $\text{Co}_3\text{O}_4$  sphere and SEI formation on long-term cycling. SEM images of hollow  $\text{Co}_3\text{O}_4$  spheres (b) before cycling, (c) after 90 cycles, and (d) after 850 cycles at 1.12 C. The red dashed squares in (e) indicate the cracks in the SEI layers. The scale bars represent (b,c) 200 nm and (d) 100 nm. (e) The entire lithiation-induced reactivation process and cycling performance. (from Ref. [111] H. Sun, G. Xin, T. Hu, M. Yu, D. Shao, X. Sun, J. Lian, *Nat. Commun.* **2014**, 5, 4526)

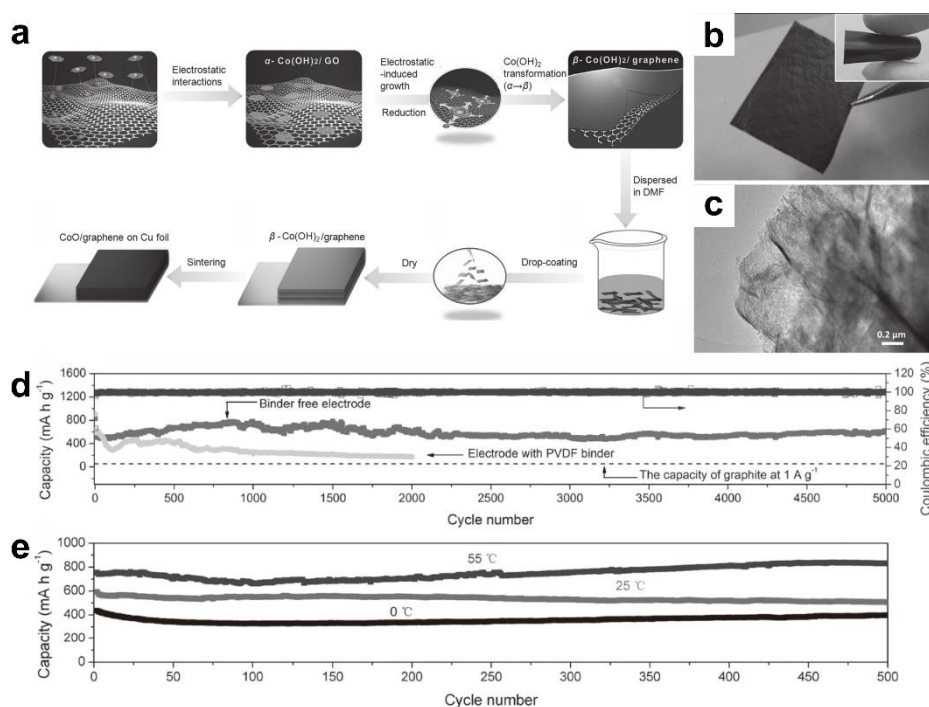


**Figure 1.6.** (a) Schematic illustration of preparation of CoO/graphene hybrid. (b) Photograph and (c) TEM image of CoO/graphene hybrid. (d) Reversible lithium extraction capacity of CoO/graphene hybrid electrode at 1 A g $^{-1}$  for 5000 cycles and (e) for 500 cycles at different temperature. (from Ref. [146] X.-l. Huang, R.-z. Wang, D. Xu, Z.-l. Wang, H.-g. Wang, J.-j. Xu, Z. Wu, Q.-c. Liu, Y. Zhang, X.-b. Zhang, *Adv. Funct. Mater.* **2013**, 23, 4345)

#### 1.2.4. Zinc Oxide

ZnO has been considered as an alternative anode material due to its high theoretical capacity (978 mAh g<sup>-1</sup>), natural abundance, low cost, and environmental benignity. The reaction mechanism of ZnO can be separated into two steps as show in Equations 6 and 7.<sup>[160-162]</sup>



During lithiation, ZnO undergoes a conversion reaction to form Li<sub>2</sub>O and nano-sized metallic zinc clusters. This step is followed by an alloying reaction between lithium and the as-generated Zn nanoparticles. The main drawback of ZnO electrodes is capacity fading upon cycling caused by a huge volume expansion (about 228%),<sup>[162,163]</sup> even at very low current densities.

Considerable efforts have been put to develop a nanostructured ZnO electrode to improve its cycle performance.<sup>[157,161-172]</sup> In particular, ZnO-carbon composite materials, including ZnO-graphene composites and carbon-coated ZnO, have shown better electrochemical properties.<sup>[157,161-172]</sup> For example, the ZnO/graphene nanocomposite prepared by high-energy ball milling exhibited high cycle stability during 500 cycles with an initial reversible capacity of

783 mAh g<sup>-1</sup>. Yang *et al.* synthesized ZnO quantum dots embedded in porous carbon derived from a metal–organic framework (isoreticular MOF-1) (**Figure 1.7a**).<sup>[157]</sup> 3.5-nm ZnO quantum dots are well embedded without agglomeration in micron-sized cubic carbon (**Figure 1.7b,c**). They delivered a very high initial discharge capacity of about 2300 mAh g<sup>-1</sup> (**Figure 1.7d**). The capacity decreased for the initial few cycles and then remained unchanged until the 50th cycle (**Figure 1.7e**). Recently, metal–organic framework-derived Zn@ZnO quantum dots/C core–shell nanorod arrays grown on a flexible carbon cloth showed excellent cycle performance during 100 cycles at a current density of 500 mA g<sup>-1</sup>.<sup>[166]</sup>

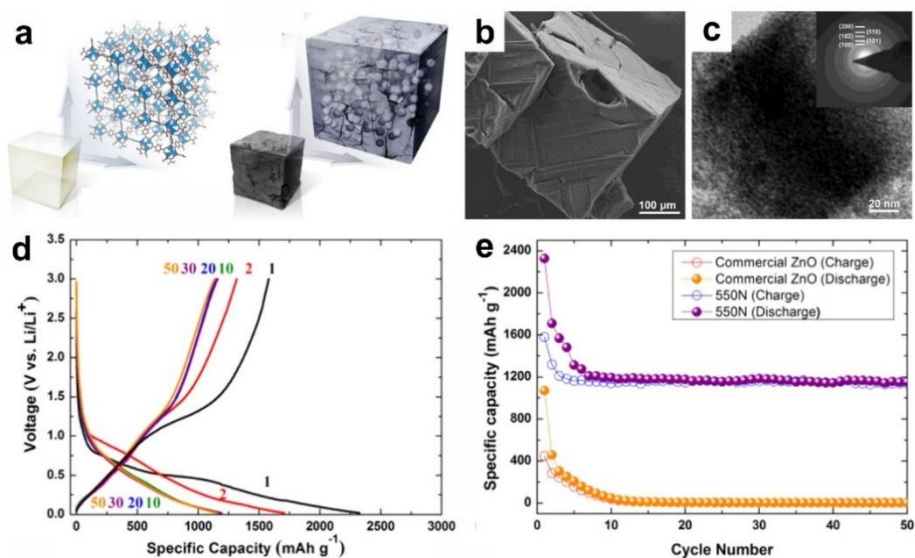


**Figure 1.7.** (a) Schematic illustrations of metal-organic framework (left) and carbon-coated ZnO quantum dots derived from a metal-organic framework (right). (b) SEM image and (c) TEM image of carbon-coated ZnO quantum dots. Inset of (c) shows corresponding SAED pattern. (d) Voltage profiles and (e) cycle performance of carbon-coated ZnO quantum dots after heat treatment at 550  $^{\circ}\text{C}$  at a current density of 75  $\text{mA g}^{-1}$ . (from Ref. [157] S. J. Yang, S. Nam, T. Kim, J. H. Im, H. Jung, J. H. Kang, S. Wi, B. Park, C. R. Park, *J. Am. Chem. Soc.* **2013**, 135, 7394)

### 1.2.5. Ruthenium Oxide

$\text{RuO}_2$  has a high electronic conductivity similar to  $\text{Fe}_3\text{O}_4$ .<sup>[31,173]</sup> There are two distinct plateaus in the first discharge curves of  $\text{RuO}_2$ . The first plateau at 2.1 V is associated with the lithium intercalation reaction with  $\text{RuO}_2$  to form the intermediate  $\text{Li}_x\text{RuO}_2$  phase ( $x \leq 1$ ).<sup>[174]</sup> The second plateau at about 0.8 V is due to the conversion reaction to form  $\text{Li}_2\text{O}$  and Ru metal clusters. Theoretically,  $\text{RuO}_2$  can store up to 4 lithium ions per formula unit ( $806 \text{ mAh g}^{-1}$ ). However, it has been reported that a much higher capacity (about  $1130 \text{ mAh g}^{-1}$ ) was delivered during the initial discharge.<sup>[175]</sup> Many researchers have proposed detailed reaction mechanisms for  $\text{RuO}_2$ , including mechanisms for the origin of its additional capacity.<sup>[173-178]</sup> For example, Balaya *et al.* have proposed an overall reversible reaction mechanism for  $\text{RuO}_2$  using high-resolution TEM (HRTEM), selected area electron diffraction (SAED), XRD, and Raman spectroscopy, which can be summarized in Equations 8, 9, and 10.<sup>[175]</sup>



Gregorczyk *et al.* have found that an intermediate crystal phase



for  $\text{Li}_x\text{RuO}_2$  formed during the first discharge. They reported that the reaction between amorphous  $\text{RuO}_2$  and  $\text{Ru/Li}_2\text{O}$  was partially reversible during the subsequent cycles.<sup>[173]</sup> Hu *et al.* have proposed that formation of  $\text{LiOH}$  and its reversible reaction to form  $\text{Li}_2\text{O}$  and  $\text{LiH}$  are responsible for the additional capacity of  $\text{RuO}_2$ , using solid-state nuclear magnetic resonance (NMR) spectroscopy and *in situ* synchrotron-based techniques (**Figure 1.8**).<sup>[174]</sup> Recently, Mao *et al.* observed a two-step process during the first lithiation of  $\text{RuO}_2$  nanowires using *in situ* TEM.<sup>[176]</sup> Kim *et al.* demonstrated that fast lithium storage occurs in the grain boundary of newly generated nano-sized Ru metal and  $\text{Li}_2\text{O}$  using *in situ* synchrotron-based techniques of TEM, X-ray photoelectron spectroscopy (XPS), and galvanostatic intermittent titration.<sup>[177]</sup>

Much research work on  $\text{RuO}_2$  has focused on determining reaction mechanisms. A few nanostructured  $\text{RuO}_2$  materials that show enhanced electrochemical properties have been reported. Still, the long-term cycle performance of  $\text{RuO}_2$  is not as good as other transition metal oxides. Gregorczyk *et al.* have prepared planar  $\text{RuO}_2$  films and three dimensional core-shell MWCNTs/ $\text{RuO}_2$  electrodes by atomic layer deposition (ALD).<sup>[179]</sup> Planar  $\text{RuO}_2$  films exhibited a very

high initial discharge capacity of about 1450 mAh g<sup>-1</sup> at C/200 and 1300 mAh g<sup>-1</sup> at C/20, but it decreased rapidly to ~400 mAh g<sup>-1</sup> after 40 cycles at C/20. Three dimensional core-shell MWCNTs/RuO<sub>2</sub> electrodes delivered about 1500 μAh cm<sup>-2</sup> at the first cycle. This result dropped to about 600 μAh cm<sup>-2</sup> after 20 cycles, and then remained stable until the 100th cycle.

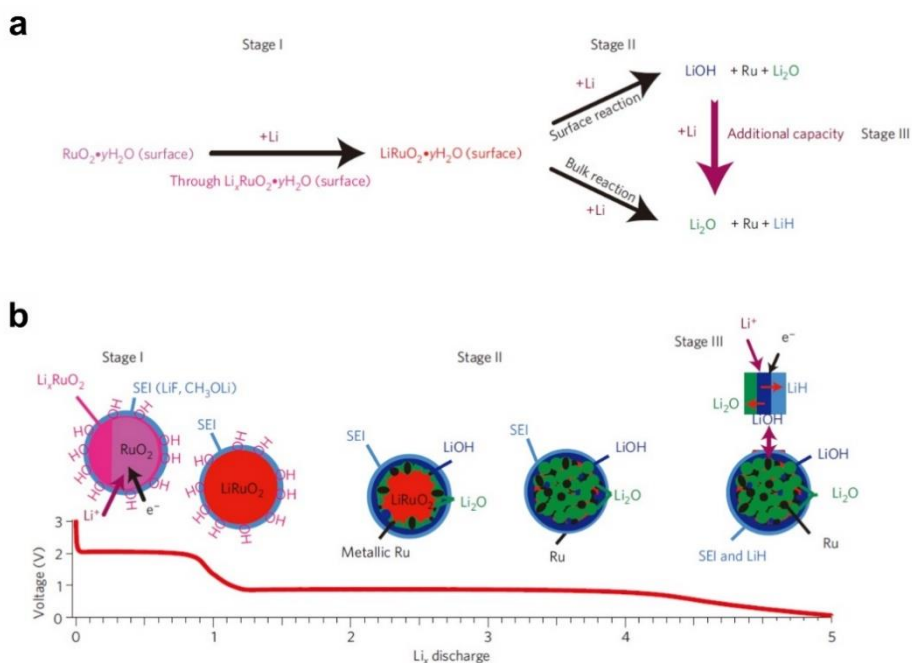


**Figure 1.8.** Schematic representations of (a) reaction pathway and (b) the phase distribution at each stage with voltage profile for initial discharge. (from Ref. [174] Y.-Y. Hu, Z. Liu, K.-W. Nam, O. J. Borkiewicz, J. Cheng, X. Hua, M. T. Dunstan, X. Yu, K. M. Wiaderek, L.-S. Du, K. W. Chapman, P. J. Chupas, X.-Q. Yang, C. P. Grey, *Nat. Mater.* **2013**, 12, 1130)

### 1.2.6 Tin Oxide

Tin dioxide ( $\text{SnO}_2$ ), an n-type semiconductor with a wide band gap (3.6 eV for a bulk material), has been utilized for gas sensor, substrates of catalyst, and sensitized solar cells.<sup>[180-182]</sup> Researchers have paid more attentions to  $\text{SnO}_2$  as LIB anode materials because of its high theoretical capacity and low voltage, which are advantageous for fabrication of high-energy-density battery. Electrochemical reaction of  $\text{SnO}_2$  with lithium ions are as follows:



Equation 11 corresponds to the conversion reactions of transition metal oxides and known to be irreversible, resulting in large irreversible capacity and low Coulombic efficiency during the first cycle. Equation 12, so-called “alloying reaction”, represents the reversible storage of lithium ion. Overall,  $\text{SnO}_2$  has theoretical irreversible capacity of  $711 \text{ mAh g}^{-1}$  from Equation 11 and reversible capacity of  $783 \text{ mAh g}^{-1}$  from Equation 12.

Recently, there are experimental evidences of the reversibility of the conversion reaction of  $\text{SnO}_2$ -based materials. Kim *et al.* reported synchrotron-based studies on the detailed lithiation/de-lithiation

mechanism of a  $\text{SnO}_2$  electrode and gave a direct evidence of the reversibility of the conversion reaction.<sup>[183]</sup> Mesoporous  $\text{SnO}_2$  was fabricated via impregnation method using KIT-6 mesoporous silica as a sacrificial template, and *in situ* XAS study was performed in order to analyze the oxidation states and the bonding types in Sn-derived materials. **Figure 1.9** shows Sn K-edge XAS data at separate regions of the first cycle. In the first discharge region, XANES spectra were apparently shifted to lower energy compared to pristine electrode, indicating  $\text{Sn}^{4+}$  was reduced to  $\text{Sn}^0$  through the conversion reaction (**Figure 1.9a**). **Figure 1.9b** represents XAS spectra in the middle discharge region. Compared to the first discharge region, there was little shift of XANES spectra where white line intensities were still decreasing. EXAFS spectra demonstrated that the amplitude of Sn–O peak declined and a Sn–Sn(Li) peak appeared. These results showed that both the conversion reaction and the alloying reaction simultaneously took place in the middle discharge region. In the last discharge region, decrease in edge energy would be expected because Sn is more electronegative than lithium. However, **Figure 1.9c** shows that XANES spectra were moved to high energy and it could be explained by charge transfer between Sn and lithium during the

alloying reaction. In addition, the intensity of the Sn–Sn peak in EXAFS spectra gradually decreased when more lithium was added to the electrode due to the lower scattering cross section of lithium compared to Sn. These XAS data exhibited that the alloying reaction was solely responsible for the capacity of the last discharge region. **Figure 1.9d** shows that the tendency observed in the last discharge region was reversed during the initial stage of charge, which indicated that only the de-alloying reaction took place. Interestingly, decreasing of Sn–Sn(Li) peak and increasing of Sn–O peak simultaneously started in the last charge region, representing the formation of SnO<sub>x</sub> (**Figure 1.9e**). This fundamental study on the reaction mechanism is not only helpful for better understanding of the complex reactions at SnO<sub>2</sub>-based nanoelectrode but useful for designing new electrode materials with unconventional high capacity.

Similar to other high-capacity anode candidates, SnO<sub>2</sub>-based electrodes also suffer from huge volume expansion/contraction during cycling. To address the issue, various nanostructures of SnO<sub>2</sub> have been developed, including nanoparticles,<sup>[184]</sup> nanosheets,<sup>[185]</sup> nanoboxes,<sup>[186]</sup> mesoporous structures,<sup>[187]</sup> hollow spheres,<sup>[188]</sup> and nanowires.<sup>[189]</sup> Although many examples have demonstrated the effectiveness of

nanostructured SnO<sub>2</sub> in terms of cycling stability, there is only limited success. By combining carbonaceous materials with SnO<sub>2</sub> nanostructures, cycling stability of SnO<sub>2</sub>-based anodes can be dramatically improved. Su *et al.* reported carbon-encapsulated SnO<sub>2</sub>-graphene nanosheets which had a reversible capacity over 800 mAh g<sup>-1</sup> after 100 cycles.<sup>[190]</sup> Wang *et al.* also fabricated nanocomposites of SnO<sub>2</sub>-RGO nanosheets and surrounding polydopamine-derived carbon. The sample showed high rechargeable capacity of 718 mAh g<sup>-1</sup> at the 200th cycle at a current density of 100 mA g<sup>-1</sup>.<sup>[191]</sup> Besides high performance of electrode materials, packing density of active material is also of great importance for practical applications. Liang *et al.* presented a synthetic method for bowl-like SnO<sub>2</sub>@carbon hollow particles that exhibited higher packing density compared to pristine hollow spheres. Owing to their unique structure, bowl-like hollow particles demonstrated 963 mAh g<sup>-1</sup> of reversible capacity after 100 cycles at a current density of 400 mA g<sup>-1</sup> and 850 mAh g<sup>-1</sup> even at an accelerated current density of 1600 mA g<sup>-1</sup>.<sup>[192]</sup> SnO<sub>2</sub> aggregates hybridized with polydopamine-derived carbon were suggested as a superior candidate for anode materials.<sup>[193]</sup>

When SnO<sub>2</sub> nanoparticles are located in a closed volume with a free space, volume expansion effect could be confined, which results in enhanced cycling stability. In addition to the confinement effect, increased conformal contact of Sn-based active materials with substrates can make conversion reaction of SnO<sub>2</sub> partially reversible. In this point of view, SnO<sub>2</sub>@CMK-5 composites with a high loading level of SnO<sub>2</sub> (>80 wt%) were tested as LIB anodes and exhibited enhanced electrochemical performance in terms of both capacity and cycling retention. The composites had very high specific capacity of 1039 mAh g<sup>-1</sup> after 100 cycles.<sup>[194]</sup> Jahel *et al.* reported ultrasmall SnO<sub>2</sub> nanoparticles confined in micro/mesoporous carbon that showed extremely long cycle life as anode materials. SnO<sub>2</sub> was incorporated into as-synthesized mesoporous carbon substrate using solution impregnation method. When the sample was galvanostatically cycled at a very high rate of 1400 mA g<sup>-1</sup> (equal to 1C), the electrode provided reversible capacity 443 mAh g<sup>-1</sup> even after 2000 cycles.<sup>[195]</sup>



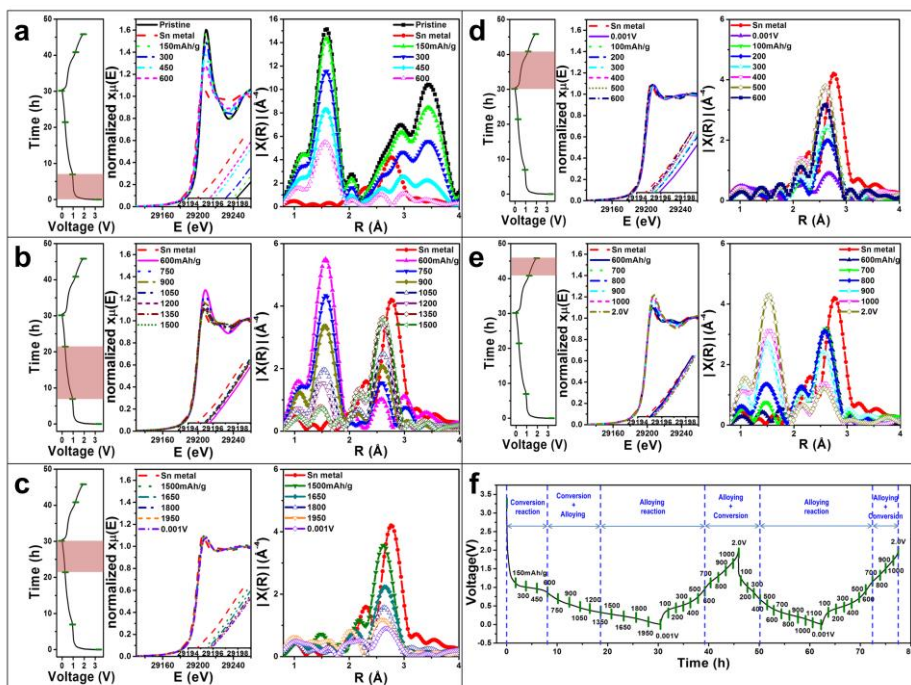


**Figure 1.9.** Sn K-edge XANES and EXAFS spectra with corresponding voltage profile taken in (a) the first discharge region, (b) the middle discharge region, (c) the last discharge region, (d) the first charge region, and (e) the last charge region of first cycle. (f) Overall electrochemical reaction mechanism of mesoporous SnO<sub>2</sub> during the first two cycles. (from Ref. [183] H. Kim, G. O. Park, Y. Kim, S. Muhammad, J. Yoo, M. Balasubramanian, Y.-H. Cho, M.-G. Kim, B. Lee, K. Kang, H. Kim, J. M. Kim, W.-S. Yoon, *Chem. Mater.* **2014**, 26, 6361)

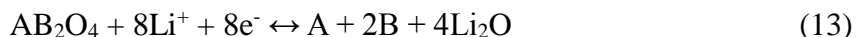
### 1.2.7. Mixed Metal Oxides

Mixed metal oxides containing  $A_xB_{3-x}O_4$  spinel structured oxides such as ferrite ( $AFe_2O_4$ ),<sup>[196-200]</sup> manganite ( $AMn_2O_4$ ),<sup>[201-202]</sup> and cobaltites ( $ACo_2O_4$ )<sup>[201-204]</sup> have shown interesting electrochemical properties as LIB anodes. Although they have multiple transition metal cations, they exhibit one plateau during initial lithiation, whereas composites of different transition metal oxides show multiple initial plateaus. For example, Kim *et al.* have shown that three distinct plateaus were observed in the initial discharge curve of a simple mixture of  $Mn_3O_4$ ,  $Fe_3O_4$ , and  $Co_3O_4$  (**Figure 1.10a**), whereas only one plateau was observed in a solid solution of  $MnFeCoO_4$  with a higher specific capacity (**Figure 1.10b**).<sup>[205]</sup> This phenomenon is more clearly observed in differential capacity curves (**Figure 1.10c**). In addition, potentials of this plateau can be varied by controlling the transition metal cations and their composition. As can be seen in **Figure 1.10d**, the potential shifts to higher values as the content of cobalt increases in Mn–Co mixed metal oxides.<sup>[206]</sup> It has been demonstrated that the potential of the plateau changed as the composition of the mixed-transition metal oxides change.<sup>[196]</sup> Hollow nanostructured metal oxides with tunable pore structures and compositions can be prepared

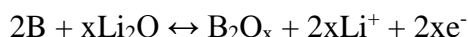
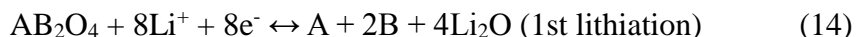
by galvanic replacement reaction. **Figure 1.11a** shows TEM images of the as-prepared  $\text{Mn}_3\text{O}_4$  nanocrystals with a side dimension of  $\sim 20$  nm and height of 10 nm. Various hollow nanoboxes with different ratios of  $\text{Mn}_3\text{O}_4/\gamma\text{-Fe}_2\text{O}_3$  (**Figure 1.11b-e**) and  $\gamma\text{-Fe}_2\text{O}_3$  nanocages (**Figure 1.11f**) were synthesized by the galvanic replacement reaction with  $\text{Mn}_3\text{O}_4$  nanocrystals and 1 ml of aqueous solutions of iron perchlorate having different concentrations. For battery applications, they were coated with polypyrrole *in situ* in the reaction mixture and carbonized at  $500^\circ\text{C}$ . These prepared carbon-coated hollow  $\text{Mn}_{3-x}\text{Fe}_x\text{O}_4$  nanoboxes and nanocages had different reaction voltages during initial discharge. The reaction voltages shifted from 0.400 to 0.818 V, proportional to the content of Fe in  $\text{Mn}_{3-x}\text{Fe}_x\text{O}_4$  (**Figure 1.11g**), indicating that the working voltage can be easily tailored. In addition, they all exhibited excellent cycle performance during 50 cycles with a high specific capacity of about  $1000\text{ mAh g}^{-1}$  (**Figure 1.11h**).

Several overall reaction mechanisms for mixed-transition metal oxides ( $\text{AB}_2\text{O}_4$ ,  $\text{A} = \text{Mn, Co, Ni, Cu, Zn, etc.}$ , and  $\text{B} = \text{Fe, Mn, and Co}$ ,  $\text{A} \neq \text{B}$ ) have been proposed, and they can be generally divided into two types as shown in Equations 13, 14, 15, and 16.

Type 1



Type 2

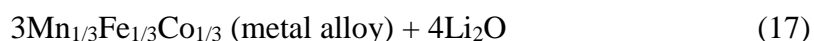
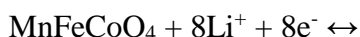


( $x = 2$  or  $3$  for ferrite,  $x = 2$  or  $8/3$  for manganite and cobaltite)

(16)

If  $A = Zn$ , then further alloying reactions occur reversibly. If  $A = Mg$  or  $Ca$ , then  $MgO$  and  $CaO$  are formed after the first lithiation, and the generated  $MgO$  and  $CaO$  do not participate in further reversible reactions. Two single-transition metal oxides have been reported in the de-lithiated state in many previous reports, which strongly supports the Type 2 mechanism (namely, a displacive redox mechanism).  $ZnO/Mn_3O_4$ <sup>[203]</sup> and  $ZnO/Fe_2O_3$ <sup>[200]</sup> domains were observed in  $ZnMn_2O_4$  and  $ZnFe_2O_4$  electrodes, respectively, at a charged state after 1 cycle by *ex situ* TEM. Similarly,  $ZnO/Co_3O_4$ <sup>[208]</sup> and  $FeO/Co_3O_4$ <sup>[209]</sup> were found in  $ZnCo_2O_4$  and  $FeCo_2O_4$ , respectively, at a charged state after 50 cycles by *ex situ* TEM. Liu *et al.* have shown the reversible conversion between polycrystalline  $MnO/Fe_3O_4$  and  $Li_2O/Mn/Fe$  after lithiation of  $MnFe_2O_4$  on graphene using *in situ*

TEM.<sup>[200]</sup> Other proposed mechanisms have been introduced as well. For example, Kim *et al.* suggested a reaction mechanism for the MnFeCoO<sub>4</sub> electrode based on *ex situ* TEM, XRD, and first principle calculations, which is summarized in Equation 17.<sup>[206]</sup>



Similar to many single-transition metal oxides, well-designed nanostructured materials can enhance electrochemical properties. Recently, self-assembled iron oxide/carbon hybrid nanosheets with a two-dimensional (2D) structure were developed by using a one-step preparation method using an iron-oleate complex and salt particles as a precursor and a template, respectively (**Figure 1.12a**).<sup>[197]</sup> The overall synthetic procedure includes mixing the iron-oleate complex and NaCl salt, followed by heat treatment in Ar, and washing with water. As shown in the SEM and TEM images, the resulting nanosheets contained uniform-sized iron oxide nanoparticles embedded in a carbon matrix and maintaining a highly ordered 2D-structure (**Figure 1.12b,c**). The size and composition of the hybrid nanosheets can be easily controlled by changing the relative amount of the iron-oleate precursor and other metal-oleate precursor, such as a

manganese-oleate complex. As a result, manganese-ferrite ( $\text{Mn}_x\text{Fe}_{3-x}\text{O}_4$ )/carbon nanosheets with different sizes and compositions were synthesized without changing morphology or structure. This method is quite simple and can be easily scaled up to multi-gram quantity. In the electrochemical testing of the ferrite/carbon nanosheets, a reversible capacity of  $600 \text{ mAh g}^{-1}$  after 50 cycles at a current density of  $100 \text{ mA g}^{-1}$  was observed (**Figure 1.12f**). Furthermore, at a very high rate of  $5000 \text{ mA g}^{-1}$ , 81.5% of the original capacity was maintained for manganese-ferrite/carbon nanosheets, attributable to the encapsulation of the conductive carbon nanosheets with highly ordered 2D structures (**Figure 1.12g**). Even after 10 charge/discharge cycles, the ferrite NPs retained their original size and morphology, and the 2D structure was maintained without deformation (**Figure 1.12d,e**). As a result, various metal oxide/carbon nanosheets can be synthesized by simple, inexpensive, and scalable methods.

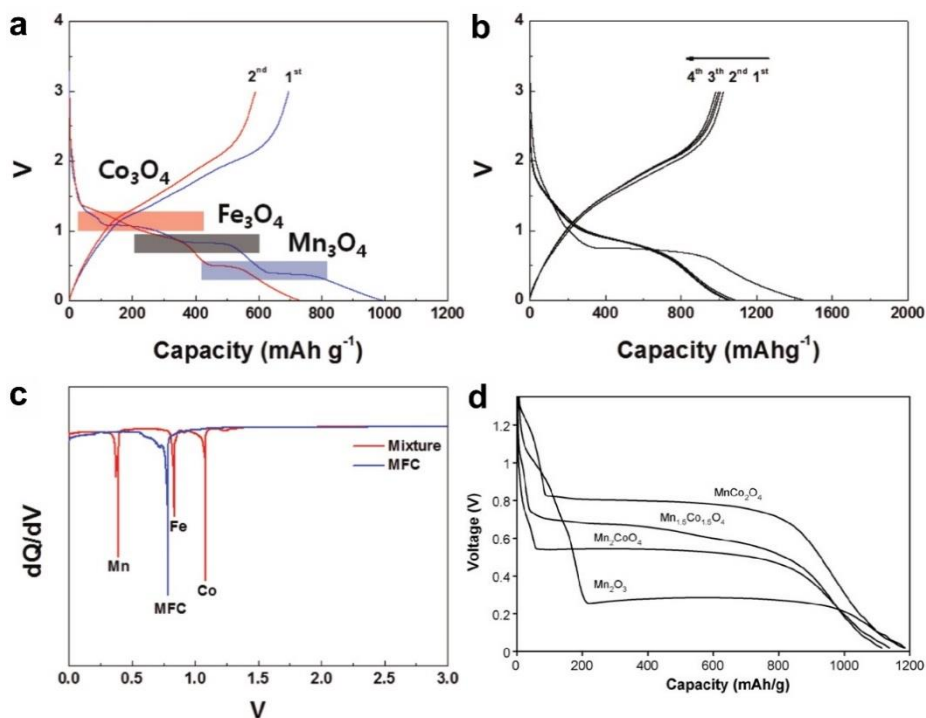


**Figure 1.10.** Charge/discharge profiles of (a) a simple mixture of  $\text{Mn}_3\text{O}_4$ ,  $\text{Fe}_3\text{O}_4$ , and  $\text{Co}_3\text{O}_4$ , and (b)  $\text{MnFeCoO}_4$ . (c) Differential capacity curves of a simple mixture of  $\text{Mn}_3\text{O}_4$ ,  $\text{Fe}_3\text{O}_4$ , and  $\text{Co}_3\text{O}_4$ , and  $\text{MnFeCoO}_4$  during initial discharge. (from Ref. [206] H. Kim, D.-H. Seo, H. Kim, I. Park, J. Hong, K.-Y. Park, K. Kang, *Chem. Mater.* **2012**, 24, 720) (d) The first discharge curves of  $\text{Mn}_2\text{O}_3$ ,  $\text{Mn}_2\text{CoO}_4$ ,  $\text{Mn}_{1.5}\text{Co}_{1.5}\text{O}_4$  and  $\text{MnCo}_2\text{O}_4$ . (from Ref. [207] P. Lavela, J. L. Tirado, C. Vidal-Abarca, *Electrochim. Acta* **2007**, 52, 7986)

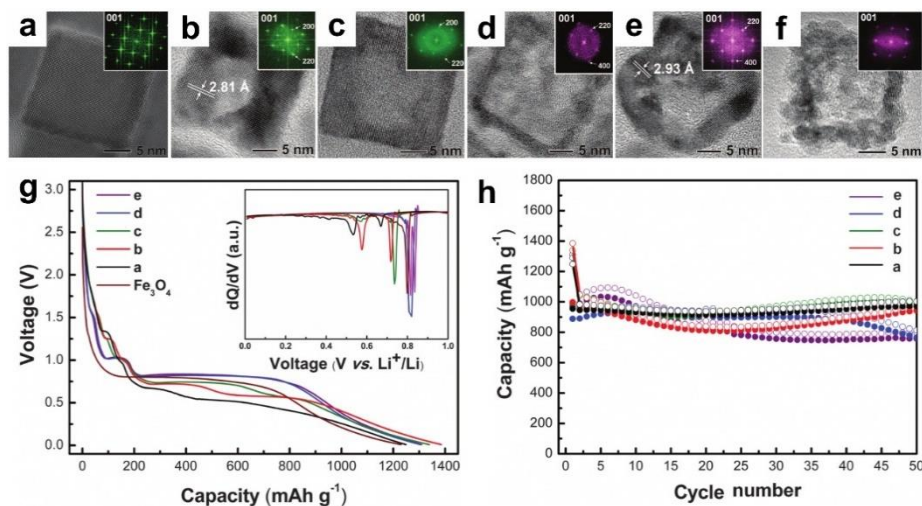


**Figure 1.11.** (a) HRTEM image of a single Mn<sub>3</sub>O<sub>4</sub> nanocrystal. (b-f) HRTEM images of the hollow nanostructures synthesized by the reaction of Mn<sub>3</sub>O<sub>4</sub> nanocrystals with 1 mL of aqueous solutions of iron (II) perchlorate having different concentrations from 0.4 M to 1.6 M. The insets of (a-f) show the corresponding FT patterns. (g) First discharge curves and corresponding differential capacities, and (h) cycle performances of carbon-coated hollow Mn<sub>3-x</sub>Fe<sub>x</sub>O<sub>4</sub>. (from Ref. [196] M. H. Oh, T. Yu, S.-H. Yu, B. Lim, K.-T. Ko, M.-G. Willinger, D.-H. Seo, B. H. Kim, M. G. Cho, J.-H. Park, K. Kang, Y.-E. Sung, N. Pinna, T. Hyeon, *Science* **2013**, 340, 964)



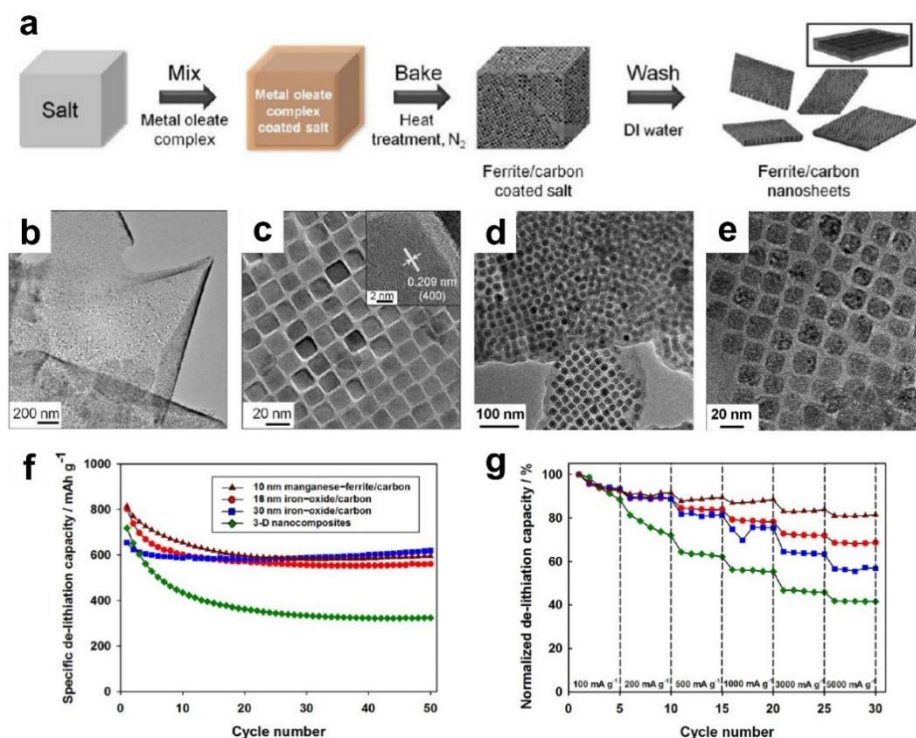


**Figure 1.12.** (a) Schematic representation of preparation of ferrite/carbon nanosheets. (b,c) TEM images of ferrite/carbon nanosheets. The inset of (c) indicates highly crystalline nature of the nanosheets. (d,e) TEM images of ferrite/carbon nanosheets after 10 cycles. (f) Cycle performance and (g) rate properties of ferrite/carbon nanosheets. (from Ref. [197] B. Jang, M. Park, O. B. Chae, S. Park, Y. Kim, S. M. Oh, Y. Piao, T. Hyeon, *J. Am. Chem. Soc.* **2012**, 134, 15010)

### 1.3. Summary and Outlook

Various nanostructured transition metal oxides react with lithium through a conversion reaction to form transition metal nanoclusters and  $\text{Li}_2\text{O}$  matrixes. These conversion reaction-based oxides are considered as promising anode candidates to replace the currently used graphite due to their high theoretical capacity. A comprehensive review of recent progress and development on conversion reaction-based transition metal oxides has been provided.

Here, I emphasize some important aspects and development directions for designing high performance anodes based on conversion reactions: (1) Transition metal oxides should be carefully chosen because many properties, such as working voltage, theoretical capacity, and electrical conductivity, are dependent on the species and phases. In addition, composites with other suitable materials such as carbonaceous materials, or use of mixed metal oxides can overcome the problems associated with single-component transition metal oxides. Although chapter I focus on metal oxides, the anionic species can significantly affect the electrochemical properties, including the reaction potential and voltage hysteresis, in various conversion reaction-based  $\text{M}_x\text{A}_y$  compounds ( $\text{M}$  = transition metal, and  $\text{A}$  = N, F,

S, P, or H).<sup>[210]</sup>

(2) The morphology significantly influences the electrochemical performance of electrode materials. There is great potential for the design of nanostructure morphologies with advantages in all the following aspects. First, the transport of both electrons and lithium ions is influenced by the morphology of the nanomaterials.<sup>[211]</sup> Specifically, lithium ion diffusion is directly affected by the particle size. For ion transport via solid-state diffusion in electrode materials, the following relationship can be established:

$$\tau = L^2/D \quad (18)$$

where  $\tau$  is the characteristic time constant for diffusion,  $L$  is the diffusion length, and  $D$  is the ion diffusion coefficient. Therefore, nano-sized electrode materials can exhibit high rate capabilities by decreasing the diffusion length of the lithium ion within the active materials. Moreover, nanostructured electrode materials have high surface-to-volume ratios, which can increase the contact area between the electrode and the electrolyte, thereby enhancing the utilization of the active material because the electrochemical reaction occurs primarily on the particle surface. Second, nanostructures with high surface-to-volume ratios exhibit many side reactions on the electrode

surface, which can consume the lithium ions and electrolytes. The byproduct of excessive SEI formation can lead to additional side reactions and safety problems. Third, most conversion reaction-based materials undergo large volume changes during cycling, resulting in rapid cycle fading. This issue can be alleviated by the design of an appropriate morphology that can provide empty spaces to accommodate the volume expansion.

(3) The proper design of nanostructures is critical to enhance the electrochemical performance of anode materials, as mentioned above. In addition, the electrochemical performance can be strongly affected by the measurement conditions, such as the mass loading, the electrode composition, the type and size of the battery cell, and the current density. Among the various measurement conditions, the mass loading and electrode composition should be considered for actual energy density. To some extent, the utilization of active materials decreases as the loading level of the electrode and/or the ratio of the active materials increases. Maintaining the electrochemical properties of nanomaterials with a high loading level of active materials and a low amount of additives is highly challenging. I hope this summary is a useful resource for understanding conversion reaction-based transition

metal oxide anodes, and will provide some insight into the development of advanced energy storage materials.

\* The contents of this chapter was published on *Small*.<sup>[212]</sup>

## 1.4 References

- [1] J.-M. Tarascon, M. Armand, *Nature* **2001**, 414, 359.
- [2] K. Kang, Y. S. Meng, J. Bréger, C. P. Grey, G. Ceder, *Science* **2006**, 311, 977.
- [3] M. S. Whittingham, *Chem. Rev.* **2004**, 104, 4271.
- [4] V. Etacheri, R. Marom, R. Elazari, G. Salitra, D. Aurbach, *Energy Environ. Sci.* **2011**, 4, 3243.
- [5] B. Scrosati, J. Hassoun, Y.-K. Sun, *Energy Environ. Sci.* **2011**, 4, 3287.
- [6] P. G. Bruce, S. A. Freunberger, L. J. Hardwick, J.-M. Tarascon, *Nat. Mater.* **2012**, 11, 19.
- [7] A. Kraytsberg, Y. Ein-Eli, *Adv. Energy Mater.* **2012**, 2, 922.
- [8] M. Hu, X. Pang, Z. Zhou, *J. Power Sources* **2013**, 237, 229.
- [9] N. Nitta, G. Yushin, *Part. Part. Syst. Charact.* **2014**, 31, 317.
- [10] C. Liang, M. Gao, H. Pan, Y. Liu, M. Yan, *J. Alloys Comp.* **2013**, 575, 246.
- [11] A. Magasinski, P. Dixon, B. Hertzberg, A. Kvit, J. Ayala, G. Yushin, *Nat. Mater.* **2010**, 9, 353.
- [12] J. S. Chen, X. W. Lou, *Small* **2013**, 9, 1877.
- [13] N. Liu, Z. Lu, J. Zhao, M. T. McDowell, H.-W. Lee, W. Zhao, Y. Cui, *Nat. Nanotechnol.* **2014**, 9, 187.

- [14] S.-H. Yu, A. Pucci, T. Herntrich, M.-G. Willinger, S.-H. Baek, Y.-E. Sung, N. Pinna, *J. Mater. Chem.* **2011**, *21*, 806.
- [15] S.-H. Yu, M. Park, H. S. Kim, A. Jin, M. Shokouhimehr, T.-Y. Ahn, Y.-W. Kim, T. Hyeon, Y.-E. Sung, *RSC Adv.* **2014**, *4*, 12087.
- [16] Y. Huang, X.-l. Huang, J.-s. Lian, D. Xu, L.-m. Wang, X.-b. Zhang, *J. Mater. Chem.* **2012**, *22*, 2844.
- [17] H. Wang, D. Ma, X. Huang, Y. Huang, X. Zhang, *Sci. Rep.* **2012**, *2*, 701.
- [18] D.-l. Ma, Z.-y. Cao, H.-g. Wang, X.-l. Huang, L.-m. Wang, X.-b. Zhang, *Energy Environ. Sci.* **2012**, *5*, 8538.
- [19] X.-l. Huang, X. Zhao, Z.-l. Wang, L.-m. Wang, X.-b. Zhang, *J. Mater. Chem.* **2012**, *22*, 3764.
- [20] X.-l. Huang, J. Chai, T. Jiang, Y.-J. Wei, G. Chen, W.-q. Liu, D. Han, L. Niu, L. Wang, X.-b. Zhang, *J. Mater. Chem.* **2012**, *22*, 3404.
- [21] P. Poizot, S. Laruelle, S. Grugeon, L. Dupont, J.-M. Tarascon, *Nature* **2000**, *407*, 496.
- [22] J. Cabana, L. Monconduit, D. Larcher, M. R. Palacín, *Adv. Mater.* **2010**, *22*, E170.
- [23] JR. Malini, U. Uma, T. Sheela, M. Ganesan, N. G. Renganathan, *Ionics* **2009**, *15*, 301.
- [24] M. V. Reddy, G. V. Subba Rao, B. V. R. Chowdari, *Chem. Rev.* **2013**,

113, 5364.

- [25] A. S. Aricò, P. Bruce, B. Scrosati, J.-M. Tarascon, W. V. Schalkwijk, *Nat. Mater.* **2005**, *4*, 366.
- [26] P. Bruce, B. Scrosati, J.-M. Tarascon, *Angew. Chem. Int. Ed.* **2008**, *47*, 2930.
- [27] R. Mukherjee, R. Krishnan, T.-M. Lu, N. Koratkar, *Nano Energy* **2012**, *1*, 518.
- [28] L. Ji, Z. Lin, M. Alcoutlabi, X. Zhang, *Energy Environ. Sci.* **2011**, *4*, 2682.
- [29] C. Yuan, H. B. Wu, Y. Xie, X. W. Lou, *Angew. Chem. Int. Ed.* **2014**, *53*, 1488.
- [30] N. A. Godshall, I. D. Raistrick, R. A. Huggins, *Mater. Res. Bull.* **1980**, *15*, 561.
- [31] W.-M. Zhang, X.-L. Wu, J.-S. Hu, Y.-G. Guo, L.-J. Wan, *Adv. Funct. Mater.* **2008**, *18*, 3941.
- [32] P. G. Bruce, B. Scrosati, J.-M. Tarascon, *Angew. Chem. Int. Ed.* **2008**, *47*, 2930.
- [33] H. S. Kim, Y. Piao, S. H. Kang, T. Hyeon, Y.-E. Sung, *Electrochem. Commun.* **2010**, *12*, 382.
- [34] N. Kang, J. H. Park, J. Choi, J. Jin, J. Chun, I. G. Jung, J. Jeong, J.-G.



- Park, S. M. Lee, H. J. Kim, S. U. Son, *Angew. Chem. Int. Ed.* **2012**, *51*, 6626.
- [35] Z. Wang, D. Luan, S. Madhavi, Y. Hu, X. W. Lou, *Energy Environ. Sci.* **2012**, *5*, 5252.
- [36] B. Wang, J. S. Chen, H. B. Wu, Z. Wang, X. W. Lou, *J. Am. Chem. Soc.* **2011**, *133*, 17146.
- [37] L. Zhang, H. B. Wu, X. W. Lou, *J. Am. Chem. Soc.* **2013**, *135*, 10664.
- [38] L. Zhang, H. B. Wu, S. Madhavi, H. H. Hng, X. W. Lou, *J. Am. Chem. Soc.* **2012**, *134*, 17388.
- [39] S. Zeng, K. Tang, T. Li, Z. Liang, D. Wang, Y. Wang, W. Zhou, *J. Phys. Chem. C* **2007**, *111*, 10217.
- [40] B. Koo, H. Xiong, M. D. Slater, V. B. Prakapenka, M. Balasubramanian, P. Podsiadlo, C. S. Johnson, T. Rajh, E. V. Shevchenko, *Nano Lett.* **2012**, *12*, 2429.
- [41] S. Xu, C. M. Hessel, H. Ren, R. Yu, Q. Jin, M. Yang, H. Zhao, D. Wang, *Energy Environ. Sci.* **2014**, *7*, 632.
- [42] H. Zhang, L. Zhou, O. Noonan, D. J. Martin, A. K. Whittaker, C. Yu, *Adv. Funct. Mater.* **2014**, *24*, 4337.
- [43] X. Zhu, Y. Zhu, S. Murali, M. D. Stollers, R. S. Ruoff, *ACS Nano* **2011**, *5*, 3333.

- [44] S.-H. Yu, X. Guo, D. Ling, D. Y. Chung, A. Jin, M. Shokouhimehr, T. Hyeon, Y.-E. Sung, *RSC Adv.* **2014**, *4*, 37365.
- [45] P. C. Wang, H. P. Ding, T. Bark, C. H. Chen, *Electrochim. Acta* **2007**, *52*, 6650.
- [46] X.-L. Wu, Y.-G. Guo, L.-J. Wan, C.-W. Hu, *J. Phys. Chem. C* **2008**, *112*, 16824.
- [47] F. Jiao, J.-C. Jumas, M. Womes, A. V. Chadwick, A. Harrison, P. G. Bruce, *J. Am. Chem. Soc.* **2006**, *128*, 12905.
- [48] X. Xu, R. Cao, S. Jeong, J. Cho, *Nano Lett.* **2012**, *12*, 4988.
- [49] S. Laruelle, S. Grugeon, P. Poizot, M. Dollé, L. Dupont, J.-M. Tarascon, *J. Electrochem. Soc.* **2002**, *149*, A627.
- [50] M. V. Reddy, T. Yu, C. H. Sow, Z. X. Shen, C. T. Lim, G. V. Subba Rao, B. V. R. Chowdari, *Adv. Funct. Mater.* **2007**, *17*, 2792.
- [51] E. Hosono, S. Fujihara, I. Honma, M. Ichihara, H. Zhou, *J. Electrochem. Soc.* **2006**, *153*, A1273.
- [52] B. Wang, H. B. Wu, L. Zhang, X. W. Lou, *Angew. Chem. Int. Ed.* **2013**, *52*, 4165.
- [53] S. H. Lee, S.-H. Yu, J. E. Lee, A. Jin, D. J. Lee, N. Lee, H. Jo, K. Shin, T. Y. Ahn, Y. W. Kim, H. Choe, Y.-E. Sung, T. Hyeon, *Nano Lett.* **2013**, *13*, 4249.

- [54] S.-H. Yu, D. E. Conte, S. Baek, D.-C. Lee, S.-K. Park, K. J. Lee, Y. Piao, Y.-E. Sung, N. Pinna, *Adv. Funct. Mater.* **2013**, 23, 4293.
- [55] G. Zhou, D.-W. Wang, F. Li, L. Zhang, N. Li, Z.-S. Wu, L. Wen, G. Q. Lu, H.-M. Cheng, *Chem. Mater.* **2010**, 22, 5306.
- [56] J. Luo, J. Liu, Z. Zeng, C. F. Ng, L. Ma, H. Zhang, J. Lin, Z. Shen, H. J. Fan, *Nano Lett.* **2013**, 13, 6136.
- [57] S. K. Behera, *Chem. Commun.* **2011**, 47, 10371.
- [58] Y. Wu, Y. Wei, J. Wang, K. Jiang, S. Fan, *Nano Lett.* **2013**, 13, 818.
- [59] C. Ban, Z. Wu, D. T. Gillaspie, L. Chen, Y. Yan, J. L. Blackburn, A. C. Dillon, *Adv. Mater.* **2010**, 22, E145.
- [60] Y. Piao, H. S. Kim, Y.-E. Sung, T. Hyeon, *Chem. Commun.* **2010**, 46, 118.
- [61] T. Muraliganth, A. V. Murugan, A. Manthiram, *Chem. Commun.* **2009**, 7360.
- [62] J. E. Lee, S.-H. Yu, D. J. Lee, D.-C. Lee, S. I. Han, Y.-E. Sung, T. Hyeon, *Energy Environ. Sci.* **2012**, 5, 9528.
- [63] E. Kang, Y. S. Jung, A. S. Cavanagh, G.-H. Kim, S. M. George, A. C. Dillon, J. K. Kim, J. Lee, *Adv. Funct. Mater.* **2011**, 21, 2430.
- [64] C. He, S. Wu, N. Zhao, C. Shi, E. Liu, J. Li, *ACS Nano* **2013**, 7, 4459.
- [65] Z.-M. Cui, L.-Y. Jiang, W.-G. Song, Y.-G. Guo, *Chem. Mater.* **2009**,

21, 1162.

- [66] X. Qin, H. Zhang, J. Wu, X. Chu, Y.-B. He, C. Han, C. Miao, S. Wang, B. Li, F. Kang, *Carbon* **2015**, 87, 347.
- [67] P. L. Taberna, S. Mitra, P. Poizot, P. Simon, J.-M. Tarascon, *Nat. Mater.* **2006**, 5, 567.
- [68] J. Park, K. An, Y. Hwang, J.-G. Park, H.-J. Noh, J.-Y. Kim, J.-H. Park, N.-M. Hwang, T. Hyeon, *Nat. Mater.* **2004**, 3, 891.
- [69] Y. Deng, L. Wan, Y. Xie, X. Qin, G. Chen, *RSC Adv.* **2014**, 4, 23914.
- [70] H. Wang, L.-F. Cui, Y. Yang, H. S. Casalongue, J. T. Robinson, Y. Liang, Y. Cui, H. Dai, *J. Am. Chem. Soc.* **2010**, 132, 13978.
- [71] X. H. Liu, J. W. Wang, S. Huang, F. Fan, X. Huang, Y. Liu, S. Krylyuk, J. Yoo, S. A. Dayeh, A. V. Davydov, S. X. Mao, S. T. Picraux, S. Zhang, J. Li, T. Zhu, J. Y. Huang, *Nat. Nanotechnol.* **2012**, 7, 749.
- [72] M. A. Lowe, J. Gao, H. D. Abruña, *J. Mater. Chem. A* **2013**, 1, 2094.
- [73] K. Zhong, B. Zhang, S. Luo, W. Wen, H. Li, X. Huang, L. Chen, *J. Power Sources* **2011**, 196, 6802.
- [74] M. Ebner, F. Marone, M. Stampanoni, V. Wood, *Science* **2013**, 342, 716.
- [75] J. Zhang, R. Wang, X. Yang, W. Lu, X. Wu, X. Wang, H. Li, L. Chen, *Nano Lett.* **2012**, 12, 2153.
- [76] W. Luo, X. Hu, Y. Sun, Y. Huang, *ACS Appl. Mater. Interfaces* **2013**, 5,

1997.

- [77] H. Jiang, Y. Hu, S. Guo, C. Yan, P. S. Lee, C. Li, *ACS Nano* **2014**, 8, 6038.
- [78] Y. Ma, C. Fang, B. Ding, G. Ji, J. Y. Lee, *Adv. Mater.* **2013**, 25, 4646.
- [79] J. Guo, Q. Liu, C. Wang, M. R. Zachariah, *Adv. Funct. Mater.* **2012**, 22, 803.
- [80] Y. Wang, Z. J. Han, S. F. Yu, R. R. Song, H. H. Song, K. Ostrikov, H. Y. Yang, *Carbon* **2013**, 64, 230.
- [81] S.-Y. Liu, J. Xie, Y.-X. Zheng, G.-S. Cao, T.-J. Zhu, X.-B. Zhao, *Electrochim. Acta* **2012**, 66, 271.
- [82] C. Yang, Q. Gao, W. Tian, Y. Tan, T. Zhang, K. Yang, L. Zhu, *J. Mater. Chem. A* **2014**, 2, 19975.
- [83] Y. Li, Q. Zhang, J. Zhu, X.-L. Wei, P. K. Shen, *J. Mater. Chem. A* **2014**, 2, 3163.
- [84] R.-C. Lee, Y.-P. Lin, Y.-T. Weng, H.-A. Pan, J.-F. Lee, N.-L. Wu, *J. Power Sources* **2014**, 253, 373.
- [85] A. L. M. Reddy, M. M. Shaijumon, S. R. Gowda, P. M. Ajayan, *Nano Lett.* **2009**, 9, 1002.
- [86] S. Wang, Y. Ren, G. Liu, Y. Xing, S. Zhang, *Nanoscale* **2014**, 6, 3508.
- [87] C. Zhu, N. Sheng, T. Akiyama, *RSC Adv.* **2015**, 5, 21066.

- [88] Z. Cai, L. Xu, M. Yan, C. Han, L. He, K. M. Hercule, C. Niu, Z. Yuan, W. Xu, L. Qu, K. Zhao, L. Mai, *Nano Lett.* **2015**, *15*, 738.
- [89] X. Sun, Y. Xu, P. Ding, G. Chen, X. Zheng, R. Zhang, L. Li, *J. Power Sources* **2014**, *255*, 163.
- [90] X. Sun, Y. Xu, P. Ding, M. Jia, G. Ceder, *J. Power Sources* **2013**, *244*, 690.
- [91] J. Qin, Q. Zhang, Z. Cao, X. Li, C. Hu, B. Wei, *Nano Energy* **2013**, *2*, 733.
- [92] L. Li, A.–R. O. Raji, J. M. Tour, *Adv. Mater.* **2013**, *25*, 6298.
- [93] C. X. Guo, M. Wang, T. Chen, X. W. Lou, C. M. Li, *Adv. Energy Mater.* **2011**, *1*, 736.
- [94] Y. Sun, X. Hu, W. Luo, F. Xia, Y. Huang, *Adv. Funct. Mater.* **2013**, *23*, 2436.
- [95] N. Lavoie, P. R. L. Malenfant, F. M. Courtel, Y. Abu–Lebdeh, I. J. Davidson, *J. Power Sources* **2012**, *213*, 249.
- [96] I. Nam, N. D. Kim, G.–P. Kim, J. Park, J. Yi, *J. Power Sources* **2013**, *244*, 56.
- [97] Y. Xiao, X. Wang, W. Wang, D. Zhao, M. Cao, *ACS Appl. Mater. Interfaces* **2014**, *6*, 2051.
- [98] H. Liu, Z. Li, Y. Liang, R. Fu, D. Wu, *Carbon* **2015**, *84*, 419.

- [99] G. Lu, S. Qiu, H. Lv, Y. Fu, J. Liu, X. Li, Y.-J. Bai, *Electrochim. Acta* **2014**, *146*, 249.
- [100] B. P. Vinayan, N. I. Schwarzburger, M. Fichtner, *J. Mater. Chem. A* **2015**, *3*, 6810.
- [101] T. Qiu, J. Wang, Y. Lu, W. Yang, *RSC Adv.* **2014**, *4*, 23027.
- [102] J. Zang, H. Qian, Z. Wei, Y. Cao, M. Zheng, Q. Dong, *Electrochim. Acta* **2014**, *118*, 112.
- [103] Y. J. Mai, D. Zhang, Y. Q. Qiao, C. D. Gu, X. L. Wang, J. P. Tu, *J. Power Sources* **2012**, *216*, 201.
- [104] Y. Cao, X. Lin, C. Zhang, C. Yang, Q. Zhang, W. Hu, M. Zheng, Q. Dong, *RSC Adv.* **2014**, *4*, 30150.
- [105] Z. Bai, N. Fan, Z. Ju, C. Guo, Y. Qian, B. Tang, S. Xiong, *J. Mater. Chem. A* **2013**, *1*, 10985.
- [106] Y. S. Yun, J. M. Kim, H. H. Park, J. Lee, Y. S. Huh, H.-J. Jin, *J. Power Sources* **2013**, *244*, 747.
- [107] Y. Ren, A. R. Armstrong, F. Jiao, P. G. Bruce, *J. Am. Chem. Soc.* **2010**, *132*, 996.
- [108] S.-Z. Huang, Y. Cai, J. Jin, J. Liu, Y. Li, Y. Yu, H.-E. Wang, L.-H. Chen, B.-L. Su, *Nano Energy* **2015**, *12*, 833.
- [109] R. Liu, S. Zhao, M. Zhang, F. Feng, Q. Shen, *Chem. Commun.* **2015**, *51*,

5728.

- [110] J. Yue, X. Gu, L. Chen, N. Wang, X. Jiang, H. Xu, J. Yang, Y. Qian, *J. Mater. Chem. A* **2014**, *2*, 17421.
- [111] H. Sun, G. Xin, T. Hu, M. Yu, D. Shao, X. Sun, J. Lian, *Nat. Commun.* **2014**, *5*, 4526.
- [112] Y. Deng, Z. Li, Z. Shi, H. Xu, F. Peng, G. Chen, *RSC Adv.* **2012**, *2*, 4645.
- [113] L. Chang, L. Mai, X. Xu, Q. An, Y. Zhao, D. Wang, X. Feng, *RSC Adv.* **2013**, *3*, 1947.
- [114] Y. Dai, H. Jiang, Y. Hu, C. Li, *RSC Adv.* **2013**, *3*, 19778.
- [115] S. Yuan, D.-I. Ma, S. Wang, Y. Liu, X. Yang, Z. Cao, *Mater. Lett.* **2015**, *145*, 104.
- [116] Y. Qiu, G.-L. Xu, K. Yan, H. Sun, J. Xiao, S. Yang, S.-G. Sun, L. Jin, H. Deng, *J. Mater. Chem.* **2011**, *21*, 6346.
- [117] X. Zhang, Y. Qian, Y. Zhu, K. Tang, *Nanoscale* **2014**, *6*, 1725.
- [118] Y. Zhang, Y. Yan, X. Wang, G. Li, D. Deng, L. Jiang, C. Shu, C. Wang, *Chem. Eur. J.* **2014**, *20*, 6126.
- [119] H. Guan, X. Wang, H. Li, C. Zhi, T. Zhai, Y. Bando, D. Golberg, *Chem. Commun.* **2012**, *48*, 4878.
- [120] B. Guo, C. Li, Z.-Y. Yuan, *J. Phys. Chem. C* **2010**, *114*, 12805.



- [121] D. Larcher, G. Sudant, J.-B. Leriche, Y. Chabre, J.-M. Tarascon, *J. Electrochem. Soc.* **2002**, *149*, A234.
- [122] X. W. Lou, D. Deng, J. Y. Lee, J. Feng, L. A. Archer, *Adv. Mater.* **2008**, *20*, 258.
- [123] L. Luo, J. Wu, J. Xu, V. P. Dravid, *ACS Nano* **2014**, *8*, 11560.
- [124] Q. Su, J. Zhang, Y. Wu, G. Du, *Nano Energy* **2014**, *9*, 264.
- [125] S. Grugeon, S. Laruelle, L. Dupont, J.-M. Tarascon, *Solid State Sci.* **2003**, *5*, 895.
- [126] Y. Mao, H. Duan, B. Xu, L. Zhang, Y. Hu, C. Zhao, Z. Wang, L. Chen, Y. Yang, *Energy Environ. Sci.* **2012**, *5*, 7950.
- [127] P. Balaya, A. J. Bhattacharyya, J. Jamnik, Y. F. Zhukovskii, E. A. Kotomin, J. Maier, *J. Power Sources* **2006**, *159*, 171.
- [128] A. Ponrouch, P.-L. Taberna, P. Simon, M. R. Palacín, *Electrochim. Acta* **2012**, *61*, 13.
- [129] G. Wang, H. Liu, J. Horvat, B. Wang, S. Qiao, J. Park, H. Ahn, *Chem. Eur. J.* **2010**, *16*, 11020.
- [130] Y. Wang, H. Xia, L. Lu, J. Lin, *ACS Nano* **2010**, *4*, 1425.
- [131] J. Jiang, J. Liu, R. Ding, X. Ji, Y. Hu, X. Li, A. Hu, F. Wu, Z. Zhu, X. Huang, *J. Phys. Chem. C* **2010**, *114*, 929.
- [132] Y. Li, B. Tan, Y. Wu, *Nano Lett.* **2008**, *8*, 265.

- [133] K. T. Nam, D.-W. Kim, P. J. Yoo, C.-Y. Chiang, N. Meethong, P. T. Hammond, Y.-M. Chiang, A. M. Belcher, *Science* **2006**, *312*, 885.
- [134] L. He, Z. Li, Z. Zhang, *Nanotechnology*. **2008**, *19*, 155606.
- [135] J. Wang, N. Yang, H. Tang, Z. Dong, Q. Jin, M. Yang, D. Kisailus, H. Zhao, Z. Tang, D. Wang, *Angew. Chem. Int. Ed.* **2013**, *52*, 6417.
- [136] Y. Kim, J.-H. Lee, S. Cho, Y. Kwon, I. In, J. Lee, N.-H. You, E. Reichmanis, H. Ko, K.-T. Lee, H. -K. Kwon, D.-H. Ko, H. Yang, B. Park, *ACS Nano* **2014**, *8*, 6701.
- [137] X. Wang, X.-L. Wu, Y.-G. Guo, Y. Zhong, X. Cao, Y. Ma, J. Yao, *Adv. Funct. Mater.* **2010**, *20*, 1680.
- [138] F. Zhan, B. Geng, Y. Guo, *Chem. Eur. J.* **2009**, *15*, 6169.
- [139] M. Xu, F. Wang, M. Zhao, S. Yang, X. Song, *Electrochim. Acta* **2011**, *56*, 4876.
- [140] J. Liu, H. Xia, L. Lu, D. Xue, *J. Mater. Chem.* **2010**, *20*, 1506.
- [141] B. Liu, X. Zhang, H. Shioyama, T. Mukai, T. Sakai, Q. Xu, *J. Power Sources* **2010**, *195*, 857.
- [142] N. Yan, L. Hu, Y. Li, Y. Wang, H. Zhong, X. Hu, X. Kong, Q. Chen, *J. Phys. Chem. C* **2012**, *116*, 7227.
- [143] X. Yang, K. Fan, Y. Zhu, J. Shen, X. Jiang, P. Zhao, S. Luan, C. Li, *ACS Appl. Mater. Interfaces* **2013**, *5*, 997.

- [144] C. Peng, B. Chen, Y. Qin, S. Yang, C. Li, Y. Zuo, S. Liu, J. Yang, *ACS Nano* **2012**, *6*, 1074.
- [145] Z.-S. Wu, W. Ren, L. Wen, L. Gao, J. Zhao, Z. Chen, G. M. Zhou, F. Li, H.-M. Cheng, *ACS Nano* **2010**, *4*, 3187.
- [146] X.-l. Huang, R.-z. Wang, D. Xu, Z.-l. Wang, H.-g. Wang, J.-j. Xu, Z. Wu, Q.-c. Liu, Y. Zhang, X.-b. Zhang, *Adv. Funct. Mater.* **2013**, *23*, 4345.
- [147] H. Kim, D.-H. Seo, S.-W. Kim, J. Kim, K. Kang, *Carbon* **2011**, *49*, 326.
- [148] S. Yang, G. Cui, S. Pang, Q. Cao, U. Kolb, X. Feng, J. Maier, K. Müllen, *ChemSusChem* **2010**, *3*, 236.
- [149] J. Zhu, Y. K. Sharma, Z. Zeng, X. Zhang, M. Srinivasan, S. Mhaisalkar, H. Zhang, H. H. Hng, Q. Yan, *J. Phys. Chem. C* **2011**, *115*, 8400.
- [150] F. D. Wu, Y. Wang, *J. Mater. Chem.* **2011**, *21*, 6636.
- [151] N. Du, H. Zhang, B. Chen, J. Wu, X. Ma, Z. Liu, Y. Zhang, D. Yang, X. Huang, J. Tu, *Adv. Mater.* **2007**, *19*, 4505.
- [152] H.-j. Liu, S.-h. Bo, W.-j. Cui, F. Li, C.-x. Wang, Y.-y. Xia, *Electrochim. Acta* **2008**, *53*, 6497.
- [153] L. Zhi, Y.-S. Hu, B. E. Hamaoui, X. Wang, I. Lieberwirth, U. Kolb, J. Maier, K. Müllen, *Adv. Mater.* **2008**, *20*, 1727.
- [154] S. Abouali, M. A. Garakani, B. Zhang, H. Luo, Z.-L. Xu, J.-Q. Huang,

- J. Huang, J.-K. Kim, *J. Mater. Chem. A* **2014**, *2*, 16939.
- [155] X. Wang, H. Guan, S. Chen, H. Li, T. Zhai, D. Tang, Y. Bando, D. Golberg, *Chem. Commun.* **2011**, *47*, 12280.
- [156] L. Zhang, H. B. Wu, X. W. Lou, *Adv. Energy Mater.* **2014**, *4*, 1300958.
- [157] S. J. Yang, S. Nam, T. Kim, J. H. Im, H. Jung, J. H. Kang, S. Wi, B. Park, C. R. Park, *J. Am. Chem. Soc.* **2013**, *135*, 7394.
- [158] B. V. L'vov, *Thermochim. Acta* **2000**, *360*, 109.
- [159] D. C. Marcano, D. V. Kosynkin, J. M. Berlin, A. Sinitskii, Z. Sun, A. Slesarev, L. B. Alemany, W. Lu, J. M. Tour, *ACS Nano* **2010**, *4*, 4806.
- [160] C. Q. Zhang, J. P. Tu, Y. F. Yuan, X. H. Huang, X. T. Chen, F. Mao, *J. Electrochem. Soc.* **2007**, *154*, A65.
- [161] L. Xiao, D. Mei, M. Cao, D. Qu, B. Deng, *J. Alloys Comp.* **2015**, *627*, 455.
- [162] Z. Ren, Z. Wang, C. Chen, J. Wang, X. Fu, C. Fan, G. Qian, *Electrochim. Acta* **2014**, *146*, 52.
- [163] Shilpa, B. M. Basavaraja, S. B. Majumder, A. Sharma, *J. Mater. Chem. A* **2015**, *3*, 5344.
- [164] X. Shen, D. Mu, S. Chen, B. Wu, F. Wu, *ACS Appl. Mater. Interfaces* **2013**, *5*, 3118.
- [165] H. Yue, Z. Shi, Q. Wang, Z. Cao, H. Dong, Y. Qiao, Y. Yin, S. Yang,

- ACS Appl. Mater. Interfaces* **2014**, *6*, 17067.
- [166] G. Zhang, S. Hou, H. Zhang, W. Zeng, F. Yan, C. C. Li, H. Duan, *Adv. Mater.* **2015**, *27*, 2400.
- [167] R. Guo, W. Yue, Y. An, Y. Ren, X. Yan, *Electrochim. Acta* **2014**, *135*, 161.
- [168] Z. Zhou, K. Zhang, J. Liu, H. Peng, G. Li, *J. Power Sources* **2015**, 285, 406.
- [169] M. Yu, D. Shao, F. Lu, X. Sun, H. Sun, T. Hu, G. Wang, S. Sawyer, H. Qiu, J. Lian, *Electrochem. Commun.* **2013**, *34*, 312.
- [170] N. Li, S. X. Jin, Y. Liao, C. X. Wang, *ACS Appl. Mater. Interfaces* **2014**, *6*, 20590.
- [171] S. Li, Y. Xiao, X. Wang, M. Cao, *Phys. Chem. Chem. Phys.* **2014**, *16*, 25846.
- [172] M. Yu, A. Wang, Y. Wang, C. Li, G. Shi, *Nanoscale* **2014**, *6*, 11419.
- [173] K. E. Gregorczyk, Y. Liu, J. P. Sullivan, G. W. Rubloff, *ACS Nano* **2013**, *7*, 6354.
- [174] Y.-Y. Hu, Z. Liu, K.-W. Nam, O. J. Borkiewicz, J. Cheng, X. Hua, M. T. Dunstan, X. Yu, K. M. Wiaderek, L.-S. Du, K. W. Chapman, P. J. Chupas, X.-Q. Yang, C. P. Grey, *Nat. Mater.* **2013**, *12*, 1130.
- [175] P. Balaya, H. Li, L. Kienle, J. Maier, *Adv. Funct. Mater.* **2003**, *13*, 621.

- [176] M. Mao, A. Nie, J. Liu, H. Wang, S. X. Mao, Q. Wang, K. Li, X.-X. Zhang, *Nanotechnology* **2015**, 26, 125404.
- [177] Y. Kim, S. Muhammad, H. Kim, Y. -H. Cho, H. Kim, J. M. Kim, W.-S. Yoon, *ChemSusChem*. **2015**, DOI: 10.1002/cssc.201403488.
- [178] A. S. Hassan, A. Navulla, L. Meda, B. R. Ramachandran, C. D. Wick, *J. Phys. Chem. C*. **2015**, 119, 9705.
- [179] K. E. Gregorczyk, A. C. Kozen, X. Chen, M. A. Schroeder, M. Noked, A. Cao, L. Hu, G. W. Rubloff, *ACS Nano*. **2015**, 9, 464.
- [180] K. Yu, Z. Wu, Q. Zhao, B. Li, Y. Xie, *J. Phys. Chem. C* **2008**, 112, 2244.
- [181] A. Birkel, Y.-G. Lee, D. Koll, X. V. Meerbeek, S. Frank, M. J. Choi, Y. S. Kang, K. Char, W. Tremel, *Energy Environ. Sci.* **2012**, 5, 5392.
- [182] C. Marichy, N. Donato, M.-G. Willinger, M. Latino, D. Karpinsky, S.-H. Yu, G. Neri, N. Pinna, *Adv. Funct. Mater.* **2011**, 21, 658.
- [183] H. Kim, G. O. Park, Y. Kim, S. Muhammad, J. Yoo, M. Balasubramanian, Y.-H. Cho, M.-G. Kim, B. Lee, K. Kang, H. Kim, J. M. Kim, W.-S. Yoon, *Chem. Mater.* **2014**, 26, 6361.
- [184] C. Kim, M. Noh, M. Choi, J. Cho, B. Park, *Chem. Mater.* **2005**, 17, 3297.
- [185] C. Wang, Y. Zhou, M. Ge, X. Xu, Z. Zhang, J. Z. Jiang, *J. Am. Chem. Soc.* **2010**, 132, 46.

- [186] Z. Wang, D. Luan, F. Y. Boey, X. W. Lou, *J. Am. Chem. Soc.* **2011**, *133*, 4738.
- [187] H. Kim, J. Cho, *J. Mater. Chem.* **2008**, *18*, 771.
- [188] J. S. Chen, L. A. Archer, X. Wen Lou, *J. Mater. Chem.* **2011**, *21*, 9912.
- [189] M. S. Park, G. X. Wang, Y. M. Kang, D. Wexler, S. X. Dou, H. K. Liu, *Angew. Chem. Int. Ed.* **2007**, *46*, 750.
- [190] Y. Su, S. Li, D. Wu, F. Zhang, H. Liang, P. Gao, C. Cheng, X. Feng, *ACS Nano* **2012**, *6*, 8349.
- [191] L. Wang, D. Wang, Z. Dong, F. Zhang, J. Jin, *Nano Lett.* **2013**, *13*, 1711.
- [192] J. Liang, X. Y. Yu, H. Zhou, H. B. Wu, S. Ding, X. W. Lou, *Angew. Chem. Int. Ed.* **2014**, *53*, 12803.
- [193] J. Kong, W. A. Yee, L. Yang, Y. Wei, S. L. Phua, H. G. Ong, J. M. Ang, X. Li, X. Lu, *Chem. Commun.* **2012**, *48*, 10316.
- [194] F. Han, W.-C. Li, M.-R. Li, A.-H. Lu, *J. Mater. Chem.* **2012**, *22*, 9645.
- [195] A. Jahel, C. M. Ghimbeu, L. Monconduit, C. Vix-Guterl, *Adv. Energy Mater.* **2014**, *4*, 1400025.
- [196] M. H. Oh, T. Yu, S.-H. Yu, B. Lim, K.-T. Ko, M.-G. Willinger, D.-H. Seo, B. H. Kim, M. G. Cho, J.-H. Park, K. Kang, Y.-E. Sung, N. Pinna, T. Hyeon, *Science* **2013**, *340*, 964.
- [197] B. Jang, M. Park, O. B. Chae, S. Park, Y. Kim, S. M. Oh, Y. Piao, T.

- Hyeon, *J. Am. Chem. Soc.* **2012**, *134*, 15010.
- [198] S. Liu, J. Xie, Q. Su, G. Du, S. Zhang, G. Cao, T. Zhu, X. Zhao, *Nano Energy* **2014**, *8*, 84.
- [199] E. K. Heidari, B. Zhang, M. H. Sohi, A. Ataie, J.-K. Kim, *J. Mater. Chem. A* **2014**, *2*, 8314.
- [200] Z. Xing, Z. Ju, J. Yang, H. Xu, Y. Qia, *Nano Res.* **2012**, *5*, 477.
- [201] L. Yu, L. Zhang, H. B. Wu, G. Zhang, X. W. Lou, *Energy Environ. Sci.* **2013**, *6*, 2664.
- [202] S. M. Hwang, S. Y. Kim, J.-G. Kim, K. J. Kim, J.-W. Lee, M.-S. Park, Y.-J. Kim, M. Shahabuddin, Y. Yamauchi, J. H. Kim, *Nanoscale* **2015**, *6*, 8351.
- [203] S.-W. Kim, H.-W. Lee, P. Muralidharan, D.-H. Seo, W.-S. Yoon, D. K. Kim, K. Kang, *Nano Res.* **2011**, *4*, 505.
- [204] L. Shen, L. Yu, X.-Y. Yu, X. Zhang, X. W. Lou, *Angew. Chem. Int. Ed.* **2015**, *54*, 1868.
- [205] J. Li, S. Xiong, Y. Liu, Z. Ju, Y. Qian, *ACS Appl. Mater. Interfaces* **2013**, *5*, 981.
- [206] H. Kim, D.-H. Seo, H. Kim, I. Park, J. Hong, K.-Y. Park, K. Kang, *Chem. Mater.* **2012**, *24*, 720.
- [207] P. Lavela, J. L. Tirado, C. Vidal-Abarca, *Electrochim. Acta* **2007**, *52*,



7986.

- [208] Y. Sharma, N. Sharma, G. V. S. Rao, B. V. R. Chowdari, *Adv. Funct. Mater* **2007**, *17*, 2855.
- [209] Y. Sharma, N. Sharma, G. V. S. Rao, B. V. R. Chowdari, *Solid State Ionics* **2008**, *179*, 587.
- [210] Y. Oumellal, A. Rougier, G. A. nazri, J.-M. Tarascon, L. Aymard, *Nat. Mater.* **2008**, *7*, 916.
- [211] L. Mai, X. Tian, X. Xu, L. Chang, L. Xu, *Chem. Rev.* **2014**, *114*, 11828.
- [212] S.-H. Yu, S. H. Lee, D. J. Lee, Y.-E. Sung, T. Hyeon, *Small*, DOI: 10.1002/sml.201502299

## **Chapter 2. Hybrid Cellular Nanosheets for High-Performance Lithium Ion Battery Anodes**

### **2.1 Introduction**

The development of the next-generation energy-storage devices is of primary importance to meet the challenges in electronics and automobile industries in the near future.<sup>[1-6]</sup> In particular, there has been increasing interest in the development of new multicomponent nanomaterials that can overcome a number of intrinsic limitations of single-component electrode materials for lithium ion batteries (LIBs).<sup>[7-11]</sup> The considerable volume changes of the active materials from lithiation and de-lithiation lead to the mechanical deformation, causing the high internal resistance and low cycle stability. This is especially pronounced for the high-capacity anode materials such as Si,<sup>[12-16]</sup> Ge,<sup>[17-19]</sup> Sn,<sup>[20]</sup> SnO<sub>2</sub>,<sup>[21-24]</sup> and Fe<sub>2</sub>O<sub>3</sub><sup>[25-28]</sup> because they have very large volume change during cycling. Also, the side reactions at the interface between the electrolyte and the active material can decrease in the Coulombic efficiency and cause safety problems.<sup>[29-31]</sup> Since the early 2000s, multicomponent nanostructures that consist of

hollow carbon shell encapsulating active materials have attracted strong interest because they can provide very effective solutions to these limitations of anode materials.<sup>[32-42]</sup> In this structure, the carbon shell confines the active material within a closed volume so that the loss of capacity due to pulverization and agglomeration can be minimized and good electric contact with the active material can be ensured during cycling. Furthermore, assembled structure of carbon shells can reduce the contact area between the electrolyte and the active materials inside of the shell, reducing the formation of the solid-electrolyte interphase (SEI). Also, the extended carbon network of the assembled structure can facilitate the electron transport.<sup>[43,44]</sup> So far, various carbon-based multicomponent hybrid nanostructures for LIB anodes have been reported to exhibit high electrochemical performance either in long stability, high capacity, or high rate capability.<sup>[45-50]</sup> Based on these previous reports, an ideal hybrid nanostructure that combines key aspects of the electrode materials including cycling stability, specific capacity, and rate performance is highly anticipated.

Herein, a new synthetic method of carbon-based hybrid nanosheets that exhibit outstanding performance in many key aspects

of the LIB anode is reported. While the synthetic procedure is simple and straightforward without any separate assembly process, as-prepared nanosheets have close-packed uniform cubic empty “cells” of ~12 nm side length that are enclosed by 3.5 nm-thick carbon walls. The inorganic anode materials are incorporated into the empty cells by simple vapor deposition. Our preparation method is easier and simpler than that of the previously reported hybrid nanomaterials.<sup>[45-50]</sup> The cubic cells enclosed by the carbon walls provide enough space for the volume change of the inorganic active material inside and retain the mechanical integrity during lithiation and de-lithiation. Also, the cubic shape ensures the maximum packing density and the larger contact area with the active material compared to the spherical shape with the same volume. The nanosheet structure provides short diffusion length of lithium ions in the thickness direction and facile electron transport through its carbon network which is as large as hundreds of square micrometers. As a model system, the electrochemical properties of hybrid cellular nanosheets loaded with tin dioxide nanoparticles (SnO<sub>2</sub> NPs) were investigated. The cell tests showed that the high specific capacity of 913.9 mAh g<sup>-1</sup> in average with excellent cycle retention of 97.0% during 300 cycles when applied to LIB anodes. Also, when the

cycling current density was increased from 200 mA g<sup>-1</sup> to 3000 mA g<sup>-1</sup>, the reversible capacity was decreased by only 20% from 941.3 mAh g<sup>-1</sup> to 745.5 mAh g<sup>-1</sup>. As a result, our hybrid cellular nanosheets showed outstanding performances in the key aspects of the LIB anode by the well-optimized carbon-based hybrid structure.

## **2.2 Experimental Section**

### **2.2.1 Chemicals**

$\text{MnCl}_2 \cdot 4\text{H}_2\text{O}$ ,  $\text{FeCl}_3 \cdot 6\text{H}_2\text{O}$ ,  $\text{Na}_2\text{SO}_4$ , and  $\text{SnCl}_2$  were purchased from Sigma-Aldrich. Sodium oleate and tetraphenyltin were purchased from TCI and Alfa-Aesar, respectively. All reagents were used without further purification.

### **2.2.2 Preparation of Carbon Cellular Nanosheets.**

Iron-oleate and manganese-oleate precursors were synthesized following a previously reported method.<sup>[51,52]</sup> For the synthesis of carbon cellular nanosheets, 18.0 g (20 mmol) of iron-oleate and 6.2 g (10 mmol) of manganese-oleate were mixed with 150 g of  $\text{Na}_2\text{SO}_4$  and the mixture was heated at 500 °C under argon flow (100 sccm) for 5 hr. After heating, carbon nanosheets embedded with manganese ferrite ( $\text{MnFe}_2\text{O}_4$ ) nanocubes were washed with hot water for 2 hr to remove  $\text{Na}_2\text{SO}_4$  and  $\text{MnFe}_2\text{O}_4$  nanocubes were etched with hydrochloric acid. Carbon cellular nanosheets were collected from the aqueous suspension by centrifugation and thermally treated at 800 °C for 5 hr to improve the conductivity of carbon.

### **2.2.3 Synthesis of SnO<sub>2</sub>-Carbon Cellular Nanosheets and SnO<sub>2</sub> Nanosheets.**

In vapor deposition method, 100 mg of carbon cellular nanosheets and 800 mg of tetraphenyltin were mixed with mortar and pestle. The mixture was heated at 350 °C for 3 hr under vacuum. As-synthesized SnO<sub>2</sub>-carbon nanosheets were used without additional purification. SnO<sub>2</sub> nanosheets were prepared by annealing SnO<sub>2</sub>-carbon hybrid cellular nanosheets at 500 °C for 5 hr under air.

### **2.2.4 Characterization.**

TEM analysis was performed using a JEOL JEM-2100F (Jeol). STEM and EDS mapping images were obtained with a Tecnai F20 (FEI) equipped with EDAX Tecnai 136-5 detector. SEM analysis was carried out on a SUPRA 55VP FE-SEM (Carl Zeiss). XPS measurement was done by a Sigma Probe instrument (ThermoFisher Scientific) with Al  $K\alpha$  (1486.8 eV) as X-ray source. The pass energy is 100 eV for wide scan and 20 eV for narrow scan. XPS data analysis was performed using Avantage software. X-ray diffraction was measured by a D/Max-3C diffractometer (Rigaku) equipped with a

rotating anode and a Cu  $K\alpha$  radiation source ( $\lambda = 0.15418$  nm), nitrogen isotherm by a 3FLEX surface characterization analyzer (Micromeritics), Raman spectrum by a T64000 spectrometer (Horiba scientific) with an excitation wavelength of 514 nm, and TGA by a Q5000 IR thermogravimetric analyzer (TA Instruments). Small-angle X-ray scattering (SAXS) data was measured in 4C beamline of Pohang Light Source (PLS-II, South Korea).

### **2.2.5 Electrochemical Characterization.**

Working electrodes were prepared by coating copper foil with a slurry made of active material, super P, and polyvinylidene fluoride (70: 15: 15 wt%) in *n*-methyl-2-pyrrolidinone solvent and drying in a vacuum oven. After cooling, the electrode film on the foil was compressed with a press roller to improve the packing of active material. 2016 type coin cells were assembled in an argon-filled glove box. The electrolyte was 1.0 M  $\text{LiPF}_6$  dissolved in ethylene carbonate and diethyl carbonate with 1:1 volume ratio. The coin cells were galvanostatically charged and discharged in the voltage range of 0.01–3.0 V (vs.  $\text{Li}^+/\text{Li}$ ) with a WBCS3000 cycler (WanA Tech). Cyclic voltammetry was measured using the same instrument. The coin cell



tests were carried out at 25 °C. Electrochemical impedance spectroscopy measurements were obtained with an AC signal amplitude of 5 mV over the frequency range from 100 kHz to 10 mHz. In order to observe the TEM images before and after electrochemical test, 2032 type coin cell was assembled using TEM grid loaded with SnO<sub>2</sub>-carbon hybrid cellular nanosheets as working electrode. The TEM grid was removed from cell after electrochemical test and washed with diethyl carbonate. After drying the TEM grid, TEM images after electrochemical test were obtained.

#### **2.2.6 *In situ* XANES Measurement.**

X-ray absorption spectroscopy was measured at the 8C nano-probe XAFS beamline (BL8C) of PLS-II in the 3.0 GeV storage ring with a ring current of 300 mA. The beam source was a tapered in-vacuum-undulator and a Si(111) double crystal monochromator was used. A secondary source aperture was used to adjust the beam size to be 0.3 mm (v) × 1 mm (h) in front of the ionization chambers. A high voltage of 3000 V was applied to the ionization chambers which were filled with a mixture gas of N<sub>2</sub> and Ar to measure X-ray intensity. Modified 2032 type coin cells were used for *in situ* XANES

experiments. The coin cell was positioned so that the incident angle of the X-ray beam with respect to the surface of the electrode is  $45^\circ$ . A passivated implanted planar silicon (PIPS) detector was mounted at the sample stage at  $90^\circ$  position with respect to the incident beam. Sn *K* edge signal was measured using metallic Sn foil as a reference and each scan took about 23 min. Data processing and analysis were performed using ATHENA of IFEFFIT XAS data analysis suite.

## 2.3 Result and Discussion

### 2.3.1 Synthesis of Hybrid Cellular Nanosheets.

The synthesis of carbon cellular nanosheets is accomplished by a modification of the previously reported method from our group.<sup>[51,52]</sup> In the first step, carbon nanosheets embedded with  $\text{MnFe}_2\text{O}_4$  nanocubes are synthesized by heating a mixture of manganese- and iron-oleate precursors and sodium sulfate ( $\text{Na}_2\text{SO}_4$ ) powder at 500 °C for 5 h under inert atmosphere (**Figure 2.1a-c**). During the heating process, both the formation of  $\text{MnFe}_2\text{O}_4$  nanocubes and their self-assembly take place at the surface of the sodium salt particles. At the same time, oleate ligands that cover the surface of the nanocubes are carbonized into the nanosheets. After the heating procedure,  $\text{Na}_2\text{SO}_4$  powder and  $\text{MnFe}_2\text{O}_4$  nanocubes are removed by washing with water and acid etching, respectively, leaving the carbon cellular nanosheets (see Experimental Section for experimental detail). Compared to  $\text{MnFe}_2\text{O}_4$ -carbon hybrid nanosheets synthesized using only iron-oleate complex, smaller-sized nanocubes can be obtained using the mixture of manganese- and iron-oleate complexes,<sup>[52]</sup> which is advantageous for LIB application.

The porous structure of the carbon cellular nanosheets consists of uniform cubic empty “cells” of ~12 nm side length that are enclosed by 3.5 nm-thick carbon walls (**Figure 2.2a,b**). The cells form ordered arrays over the whole area of the nanosheets that is as large as hundreds of square micrometers. The cross-section of a nanosheet in scanning electron microscopy (SEM) image (**Figure 2.2c**) shows that the thickness is ~100 nm, which corresponds to <10 layers of the cells (see **Figures 2.1d-f** and 2.3 for additional electron microscopy images and small-angle X-ray scattering data of the carbon cellular nanosheets). Actually, this structure resembles the plant leaf tissue that is composed of the two-dimensional array of cells partitioned by cell walls (**Figure 2.2d-f**).

Hybrid cellular nanosheets were prepared by introducing SnO<sub>2</sub> as high capacity anode material inside the carbon cells via vapor deposition using tetraphenyltin [Sn(C<sub>6</sub>H<sub>5</sub>)<sub>4</sub>] as a precursor. This method is inspired from the well-known “ship-in-a-bottle” approach which is used for incorporation of various materials into the pores/cages of zeolites<sup>[53]</sup> or mesoporous materials.<sup>[54]</sup> The carbon cellular nanosheets are mixed with tetraphenyltin and heated at 350 °C for 3 h under vacuum. In this condition, vaporized tin precursor

infiltrated inside of the cells and subsequently turns into SnO<sub>2</sub> NPs via thermal decomposition. The remaining unreacted precursor is evaporated away, leaving no residue on the exterior surface of the nanosheets. **Figure 2.4a** shows transmission electron microscopy (TEM) image of SnO<sub>2</sub> NPs formed in the cells. The statistics of the size of SnO<sub>2</sub> NPs, the side length of the empty cells, and the wall thickness are shown in **Figure 2.4b**. The size of the NPs is far smaller than the cavity volume of the cells. Since the lithiation of SnO<sub>2</sub> NPs increases the volume by 300%, such a large difference in the cavity volume and the NPs is beneficial for better mechanical stability and reversible capacity of the electrode, as discussed below.

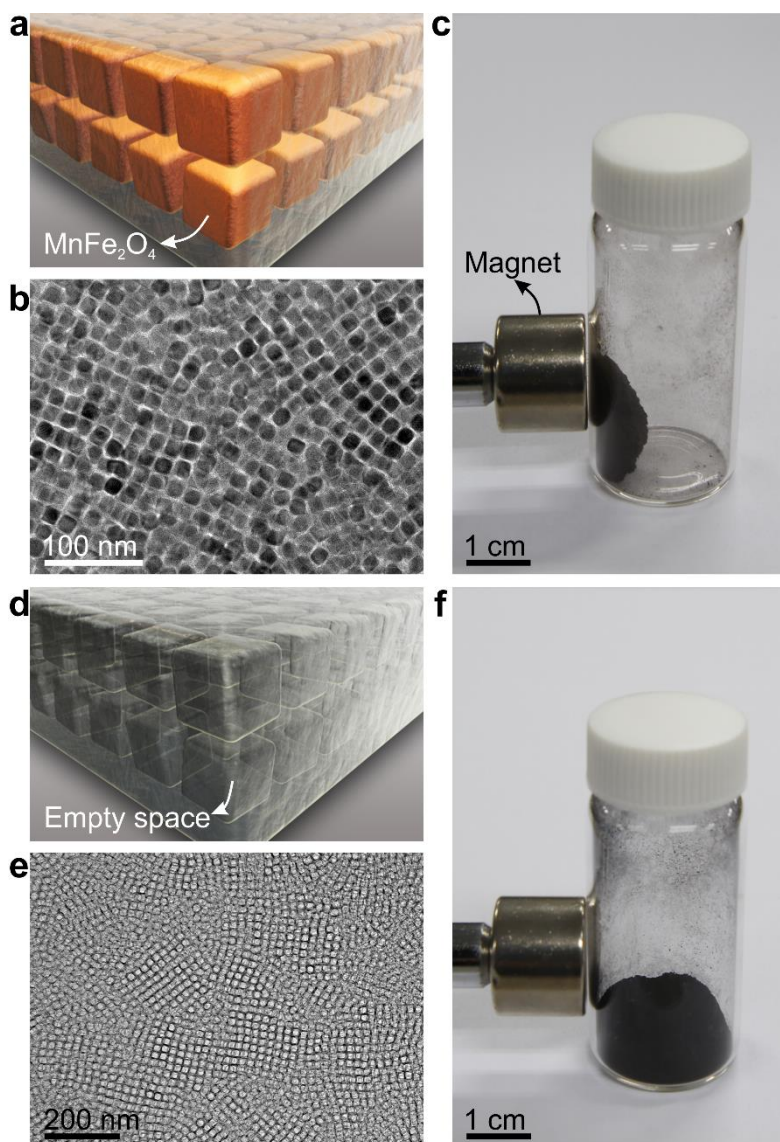


**Figure 2.1.** (a,d) Graphic illustrations and (b,e) the corresponding TEM images of the carbon cellular nanosheets before and after etching  $\text{MnFe}_2\text{O}_4$  nanocubes. Pictures in (c,f) show that powder of the nanosheets was not attracted by a magnet after acid etching.

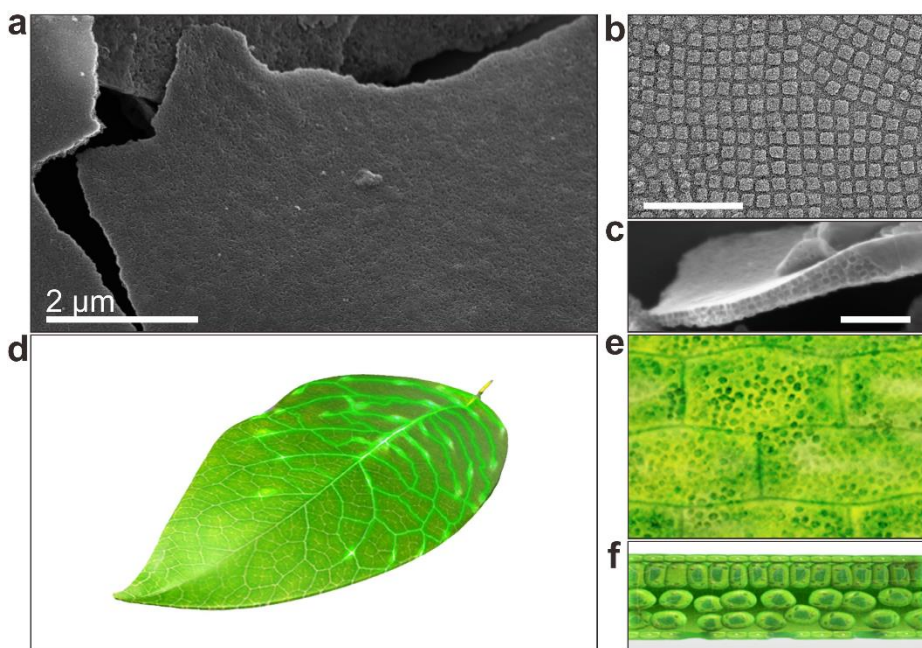


**Figure 2.2.** Carbon and SnO<sub>2</sub>-carbon cellular nanosheets. (a) SEM image, (b) TEM image and (c) cross-sectional SEM image of carbon cellular nanosheets. The scale bars in (b) and (c) are 100 and 200 nm, respectively. Schematic illustration of (d) a plant leaf, (e) its top and (f) cross-sectional structures resembling the carbon cellular nanosheets.

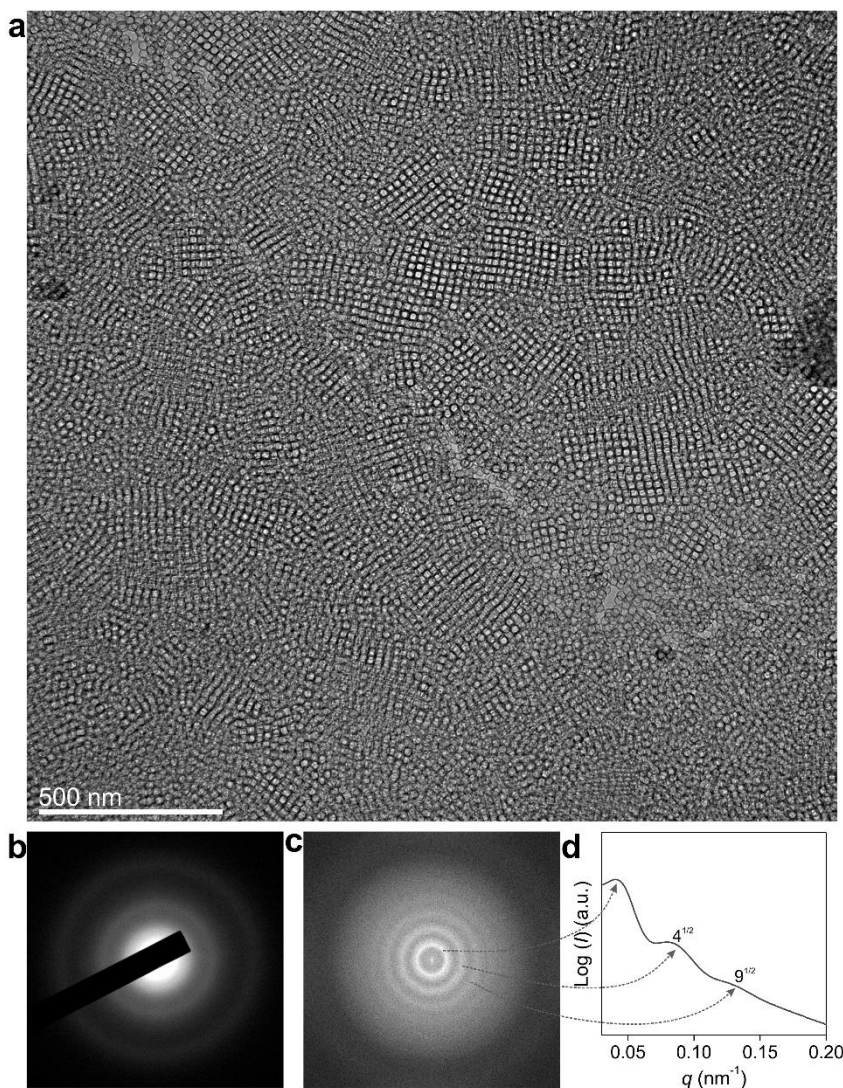


**Figure 2.3.** (a) Large-area TEM image and (b) electron diffraction pattern of carbon cellular nanosheets. (c) Fast-Fourier-transform (FFT) pattern of (a). (d) Small-angle X-ray scattering (SAXS) pattern of carbon cellular nanosheets. FFT pattern and SAXS pattern confirm the periodic mesostructure of cellular carbon nanosheets.



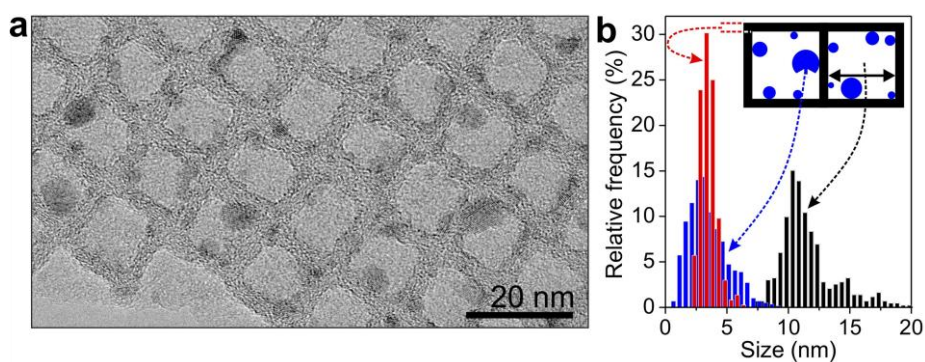


**Figure 2.4.** Carbon and SnO<sub>2</sub>-carbon cellular nanosheets. (a) TEM image of a SnO<sub>2</sub>-carbon hybrid cellular nanosheet showing SnO<sub>2</sub> NPs in the cells. (b) Statistical analysis of the size of SnO<sub>2</sub> NPs (blue), side length of the cells (black), and the thickness of the carbon walls (red).

### 2.3.2 Synthesis and Characterization of Hybrid Cellular Nanosheets.

Detailed structure analysis of the carbon cellular nanosheets before and after incorporating SnO<sub>2</sub> by “ship-in-a-bottle” method was performed by various techniques and the results are shown in **Figure 2.5** and **2.6**. The pore size and volume of the cellular nanosheets are analyzed by N<sub>2</sub> adsorption and desorption isotherm measurements (**Figure 2.5a,b**). Before the incorporation, pores with the sizes of 3.0 nm, 5.1 nm, and 14.1 nm were identified from the carbon cellular nanosheets. The size of the largest pores (14.1 nm) matches the cubic cell size measured by TEM (~12 nm). After loading the NPs, the size of the largest pores was decreased to 12.4 nm and the pore volume was changed from 0.71 cm<sup>3</sup> g<sup>-1</sup> to 0.28 cm<sup>3</sup> g<sup>-1</sup>. The reduction in both the pore size and volume is consistent with the observation from TEM that the cubic empty cells were occupied by the NPs.<sup>[55,56]</sup> X-ray diffraction (XRD) data from carbon and SnO<sub>2</sub>-carbon nanosheets are shown in **Figure 2.5c**. The two broad peaks from the carbon nanosheets at  $2\theta = 23$  and  $42^\circ$  are assigned to the (002) and (101) planes of carbon.<sup>[57]</sup> On the other hand, the pattern of SnO<sub>2</sub>-carbon nanosheets is clearly indexed to tetragonal SnO<sub>2</sub> (JCPDS card no. 41-

1445). Raman spectroscopy data show that the peak intensity ratio of D and G bands from carbon ( $I_D/I_G$ ) is almost identical in the spectra from carbon and SnO<sub>2</sub>-carbon nanosheets (**Figure 2.5d**), showing that the impregnation process does not affect the carbon structure of the nanosheets. After impregnation, signal from Sn<sup>4+</sup> is observed in Sn 3d region by X-ray photoelectron spectroscopy (XPS) confirming the presence of SnO<sub>2</sub> phase in the nanosheets (**Figure 2.6a**).<sup>[58]</sup> C 1s XPS data reveal that there are oxygen functional groups such as C–O and O–C=O in the carbon nanosheets, probably due to the acid etching treatment (**Figure 2.6b**). These oxygen functional groups can help the formation of SnO<sub>2</sub> NPs at the interior wall of the carbon cells (see **Figure 2.6c** for the corresponding wide-scan XPS of **Figure 2.6a** and f).<sup>[59,60]</sup> According to thermogravimetric analysis (TGA), the carbon nanosheets contain no inorganic impurity while the content of SnO<sub>2</sub> in SnO<sub>2</sub>-carbon nanosheets is 38.0 wt% (**Figure 2.6d**). The content of SnO<sub>2</sub> can be controlled by varying the ratio of carbon nanosheets to precursor and/or by repeating the deposition process (**Figure 2.7**).

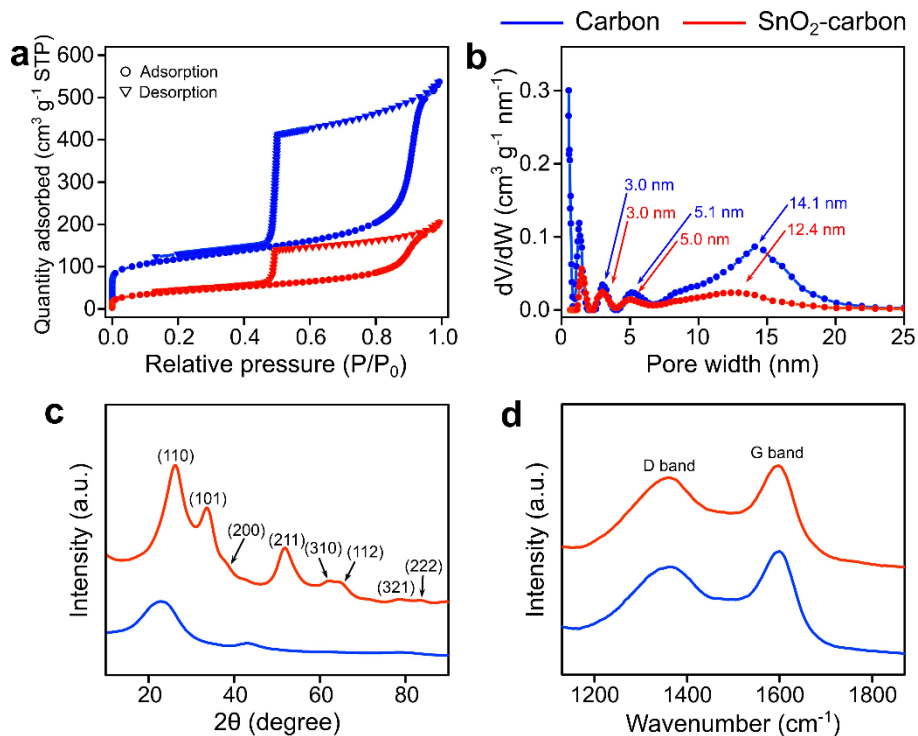


**Figure 2.5.** Structure analysis of carbon and SnO<sub>2</sub>-carbon cellular nanosheets. For all panels, blue indicates carbon cellular nanosheets and red represents SnO<sub>2</sub>-carbon cellular nanosheets. (a) N<sub>2</sub> adsorption-desorption isotherms and (b) the pore size distributions from the isotherm curves. (c) XRD plots. The diffraction peaks from SnO<sub>2</sub>-carbon nanosheets are indexed to tetragonal SnO<sub>2</sub>. (d) Raman spectra. The bands at around 1600 cm<sup>-1</sup> and 1360 cm<sup>-1</sup> are assigned to G and D bands of graphite structure.

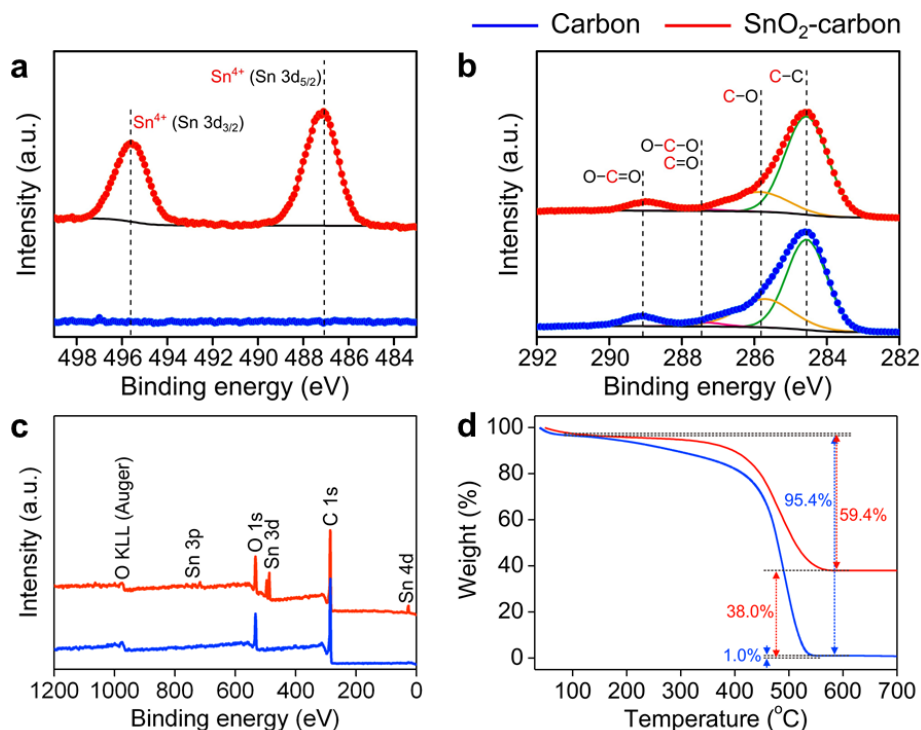


**Figure 2.6.** Structure analysis of carbon and SnO<sub>2</sub>-carbon cellular nanosheets. For all panels, blue indicates carbon cellular nanosheets and red represents SnO<sub>2</sub>-carbon cellular nanosheets. XPS spectra from (a) Sn 3d and (b) C 1s. The peaks are assigned by curve fittings indicated in different colors. (c) Wide-scan XPS spectra and (d) TGA curves of hybrid cellular nanosheets (red) and carbon cellular nanosheets (blue).

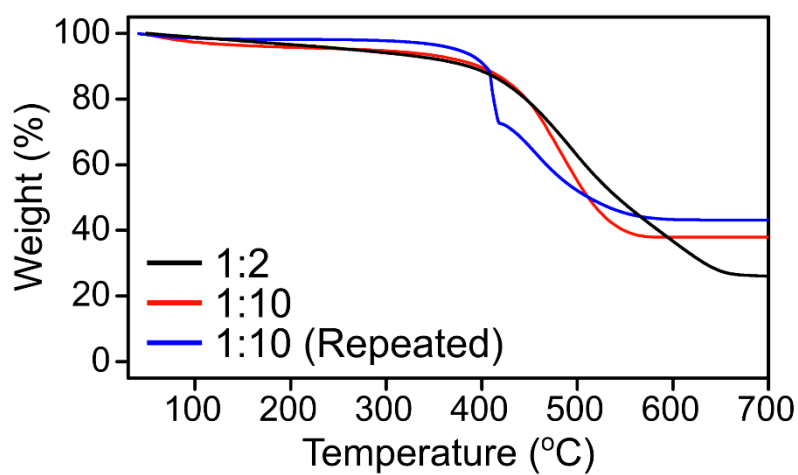


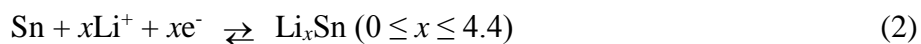
**Figure 2.7.** TGA curves of hybrid cellular nanosheets with various contents of SnO<sub>2</sub>.

### 2.3.3 Electrochemical Performance of Hybrid Cellular Nanosheets.

Electrochemical performances of SnO<sub>2</sub>-carbon hybrid cellular nanosheets were investigated by a series of experiments in comparison with the carbon cellular nanosheets and SnO<sub>2</sub> nanosheets. SnO<sub>2</sub> nanosheets are prepared by heating SnO<sub>2</sub>-carbon hybrid cellular nanosheets at 500 °C in air, leading to the formation of the nanosheets of sintered SnO<sub>2</sub> NPs (**Figure 2.8**). The electrochemical cycling stability of SnO<sub>2</sub>-carbon hybrid, carbon, and SnO<sub>2</sub> nanosheets was evaluated by galvanostatic charge–discharge in a potential range of 0.01–3.0 V (vs. Li<sup>+</sup>/Li) at a constant current density of 200 mA g<sup>-1</sup> (**Figure 2.9a**). After 300 cycles, the reversible capacity of SnO<sub>2</sub>-carbon hybrid nanosheets is changed from 941.3 mAh g<sup>-1</sup> (1st cycle) to 913.3 mAh g<sup>-1</sup> (300th cycle), showing outstanding cycle retention of 97.0%. The average capacity value of the hybrid nanosheets is higher than those from the previously reported SnO<sub>2</sub>-carbon nanostructures.<sup>[61-64]</sup> Carbon cellular nanosheets also exhibit relatively high cycling stability with the retention of 86.6% during 300 cycles and the average capacity was 463.0 mAh g<sup>-1</sup>. On the other hand, the capacity of SnO<sub>2</sub> nanosheets rapidly decreases during the first 50 cycles from 882.2 mAh g<sup>-1</sup> (1st cycle) to 141.1 mAh g<sup>-1</sup> (50th cycle).

The overall features of initial charge-discharge voltage profiles of SnO<sub>2</sub>-carbon hybrid nanosheets are similar to those of other SnO<sub>2</sub>-carbon composite materials in the previous reports (**Figure 2.10**).<sup>[49,61]</sup> The initial discharge capacity and Coulombic efficiency are 1,910.7 mAh g<sup>-1</sup> and 49.3%, respectively. As shown in **Figure 2.9b**, the voltage profiles of SnO<sub>2</sub>-carbon hybrid nanosheets are so stable that the profile plots from the 100th to the 200th cycle are almost exactly overlapped on top of each other. Even at very high current densities of 1000 and 3000 mA g<sup>-1</sup>, the hybrid cellular nanosheets exhibit high reversible capacities of 815.1 and 745.5 mAh g<sup>-1</sup>, respectively (**Figure 2.9c**). It can therefore be concluded that the electrochemical properties of hybrid cellular nanosheets are comprehensively outstanding when compared with the other SnO<sub>2</sub>-based anode materials.

The lithiation and de-lithiation of SnO<sub>2</sub> NPs in the hybrid cellular nanosheets were investigated by cyclic voltammetry and *in situ* X-ray absorption near-edge structure (XANES) spectroscopy. It is known that there are two reactions between lithium and SnO<sub>2</sub> taking place during charge and discharge processes<sup>[65]</sup>:





Usually Reaction 1 is considered to be irreversible while Reaction 2 is responsible for the theoretical reversible capacity of 782 mAh g<sup>-1</sup>. However, recently it was reported that Reaction 1 is partially reversible and contributing to the capacity of SnO<sub>2</sub>.<sup>[66,67]</sup> **Figure 2.11a** shows three initial consecutive cyclic voltammograms (CVs) of the three nanosheets. The CVs of SnO<sub>2</sub>-carbon hybrid cellular nanosheets have the features from both carbon and SnO<sub>2</sub> nanosheets. However, the anodic peaks at 0.53 and 1.23 V from SnO<sub>2</sub>-carbon nanosheets are shifted to the lower potentials compared to those from SnO<sub>2</sub> nanosheets that are observed at 0.58 and 1.25 V, respectively. The lower polarization suggests that the reaction of SnO<sub>2</sub> in the hybrid nanosheets is different from that of pure SnO<sub>2</sub>. In order to investigate the electrochemical reaction process of SnO<sub>2</sub> in detail, the temporal change in the oxidation state of Sn during cycling was investigated by *in situ* XANES measurements. As shown in **Figure 2.11b**, the white line intensity of the signals from SnO<sub>2</sub>-carbon hybrid nanosheets measured at the start and the end of the cycling are quite similar. On the other hand, the white line intensity from SnO<sub>2</sub> nanosheets becomes far weaker after one cycle. Such difference in the white line intensity is attributed to the different oxidation state of Sn in the nanosheets.

According to the linear combination fit analysis using Sn metal, SnO, and SnO<sub>2</sub> as the standards, both the hybrid nanosheets and SnO<sub>2</sub> nanosheets contain only SnO<sub>2</sub> before cycling (see **Figure 2.12** for the standard XANES data of Sn metal, SnO, and SnO<sub>2</sub>). However, after one cycle, the ratio of Sn:SnO:SnO<sub>2</sub> was changed to 0:45:55 for the hybrid nanosheets and 26:51:23 for SnO<sub>2</sub> nanosheets, demonstrating that tin oxide in the hybrid nanosheets can have better reversibility of the electrochemical reactions. In particular, it seems that a considerable amount of metallic Sn is oxidized to SnO<sub>2</sub> via Reaction 1 during de-lithiation of the hybrid nanosheets.

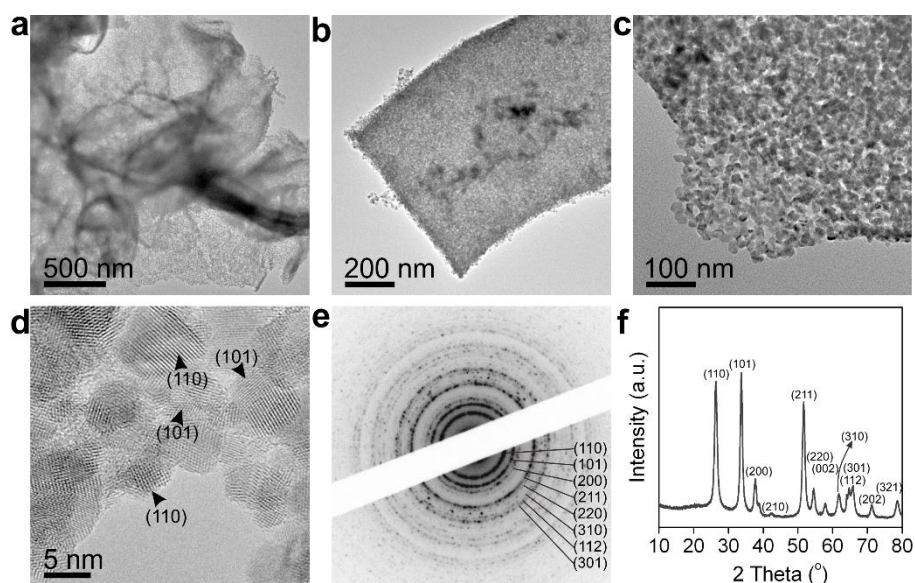


**Figure 2.8.** (a-d) TEM images, (e) SAED pattern, and (f) XRD pattern of SnO<sub>2</sub> nanosheets. SAED and XRD pattern are well indexed to tetragonal SnO<sub>2</sub>.

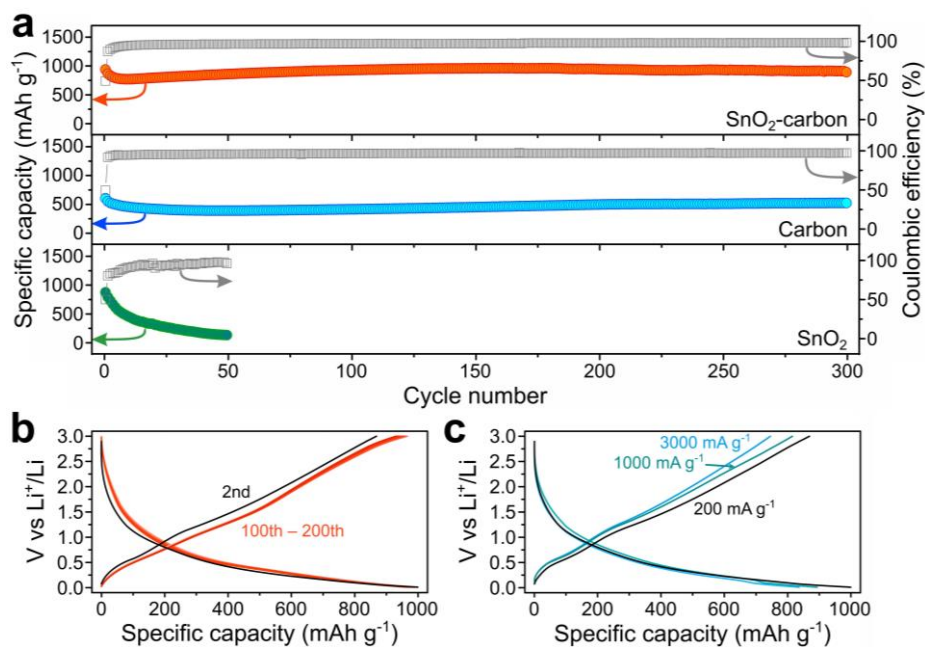


**Figure 2.9.** Electrochemical characterization of SnO<sub>2</sub>-carbon, carbon, and SnO<sub>2</sub> nanosheets for lithium ion battery anodes. (a) Cycling performance of the three kinds of nanosheets at a current density of 200 mA g<sup>-1</sup>. (b) Voltage profiles of SnO<sub>2</sub>-carbon nanosheets corresponding to the SnO<sub>2</sub>-carbon data in (a). In (b), the current density was 200 mA g<sup>-1</sup>. (c) Voltage profiles of SnO<sub>2</sub>-carbon nanosheets at three current densities in the 2nd cycle. The black profile curves in (b,c) are identical.

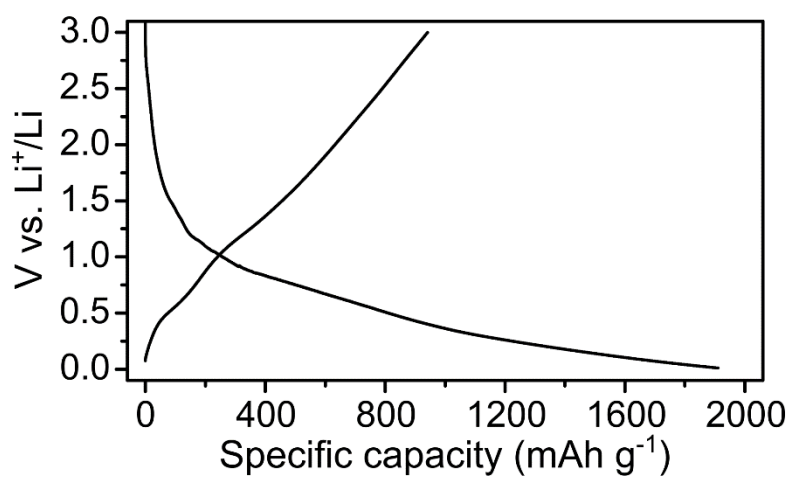


**Figure 2.10.** Initial charge-discharge voltage profiles of SnO<sub>2</sub>-carbon hybrid cellular nanosheets at a current density of 200 mA g<sup>-1</sup>.

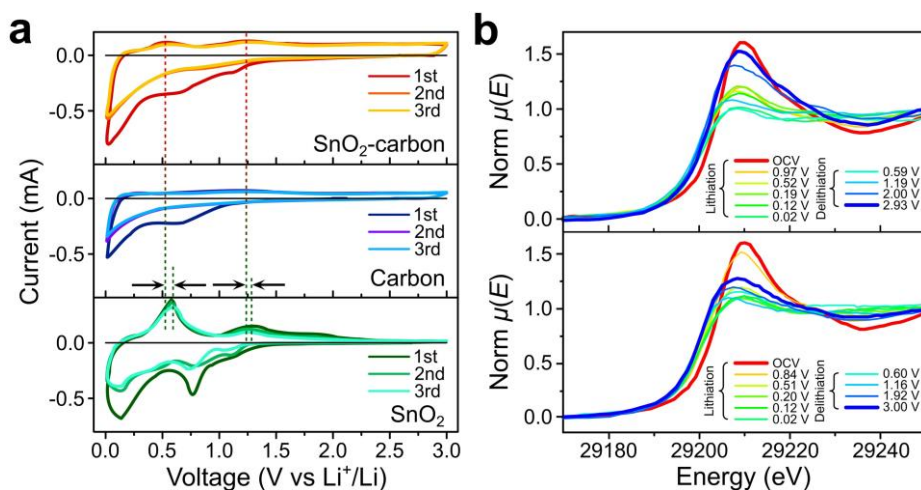


**Figure 2.11.** Electrochemical characterization of SnO<sub>2</sub>-carbon, carbon, and SnO<sub>2</sub> nanosheets for lithium ion battery anodes. (a) Cyclic voltammograms of the nanosheets. The scan rate was 0.1 mV s<sup>-1</sup>. The shift in the current peak positions is indicated with arrows. (b) *In situ* Sn *K* edge XANES data of SnO<sub>2</sub>-carbon and SnO<sub>2</sub> nanosheets measured during the 1st cycle at the current density of 200 mA g<sup>-1</sup> and the voltage range of 0.01–3.0 V (vs. Li<sup>+</sup>/Li). OCV indicates the XANES patterns measured just before starting the cycle.

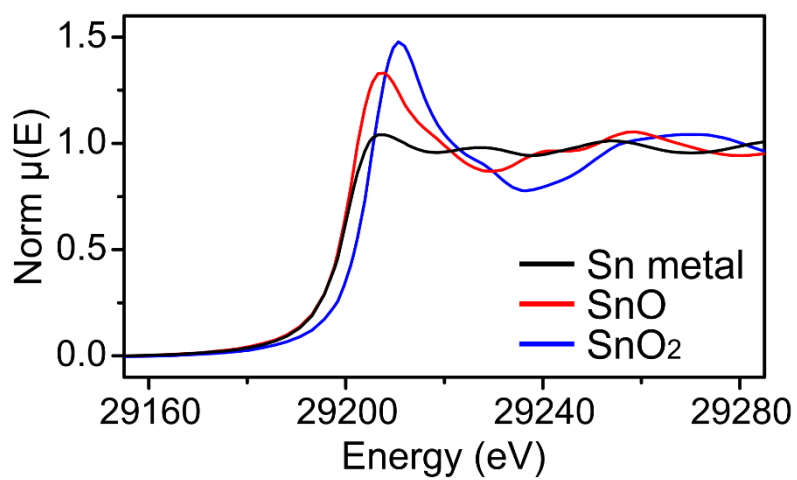


**Figure 2.12.** Standard XANES data of Sn metal, SnO, and SnO<sub>2</sub>.

### 2.3.4 Structural Change of Hybrid Cellular Nanosheets by Lithiation and De-lithiation.

Changes in the structure of SnO<sub>2</sub>-carbon hybrid cellular nanosheets induced by cycling were studied by extensive TEM analysis. As mentioned above, insertion of lithium into SnO<sub>2</sub> leads to the formation of Li<sub>x</sub>Sn ( $x \leq 4.4$ ) embedded in Li<sub>2</sub>O matrix which is accompanied by large volume expansion of ~300%. TEM images in **Figure 2.13a-c** show how the size and the morphology of SnO<sub>2</sub> NPs in the nanosheets change during the lithiation and de-lithiation. When fully lithiated (0.01 V vs. Li<sup>+</sup>/Li), SnO<sub>2</sub> NPs are expanded almost completely filling the volume of the cell (**Figure 2.13b**). Interestingly, de-lithiation does not restore the NPs with the initial size and shape. Instead, SnO<sub>2</sub>-based active material is coated inside wall of the cell after de-lithiation (**Figure 2.13c**), indicating that the active material has good affinity (low interface energy) with the surface of the carbon wall. Also, this morphology maximizes its interface area with carbon. This can also be observed in large-area TEM images (**Figure 2.14a and b**). The good affinity and large interface area of the active material can explain the low polarization of the hybrid cellular nanosheets observed in cyclic voltammetry in **Figure 2.11a**. TEM images in



**Figure 2.14c,d** were taken from the same location of the nanosheets before and after the lithiation and de-lithiation cycle. Comparing those two images, it is clearly seen that the carbon cellular structure is hardly affected by the large volume change of SnO<sub>2</sub>-based active material inside of the cells. The spatial distribution of SnO<sub>2</sub>-based active material after 20 cycles was measured by energy-dispersive X-ray spectroscopy (EDX) mapping of Sn and dark-field TEM (**Figure 2.15a-c**, see **Figure 2.16** for large-area STEM image). Both elemental mapping and dark-field images confirm that SnO<sub>2</sub>-derived active material is well confined in the cells without aggregation or leakage from the cells.

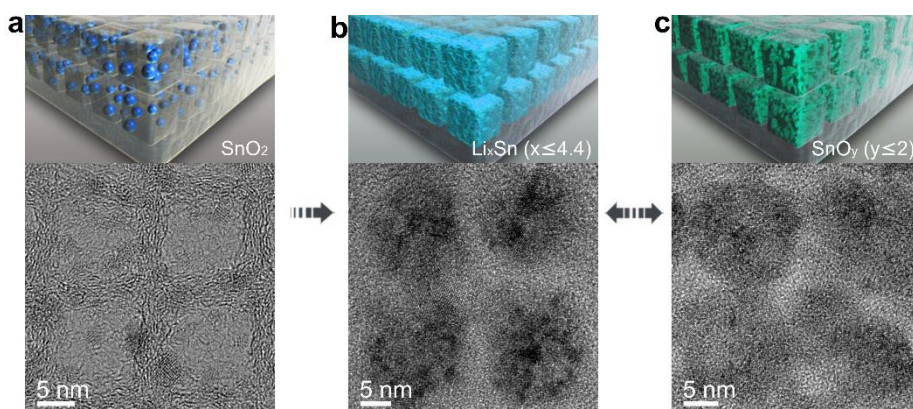


**Figure 2.13.** TEM analysis on the structural change of hybrid cellular nanosheets. Schematics of the morphology of  $\text{SnO}_2$  NPs and  $\text{SnO}_2$ -based active material structure in the carbon cells (top) and TEM images of hybrid cellular nanosheets (bottom) (a) before cycling, (b) after lithiation, and (c) de-lithiation.

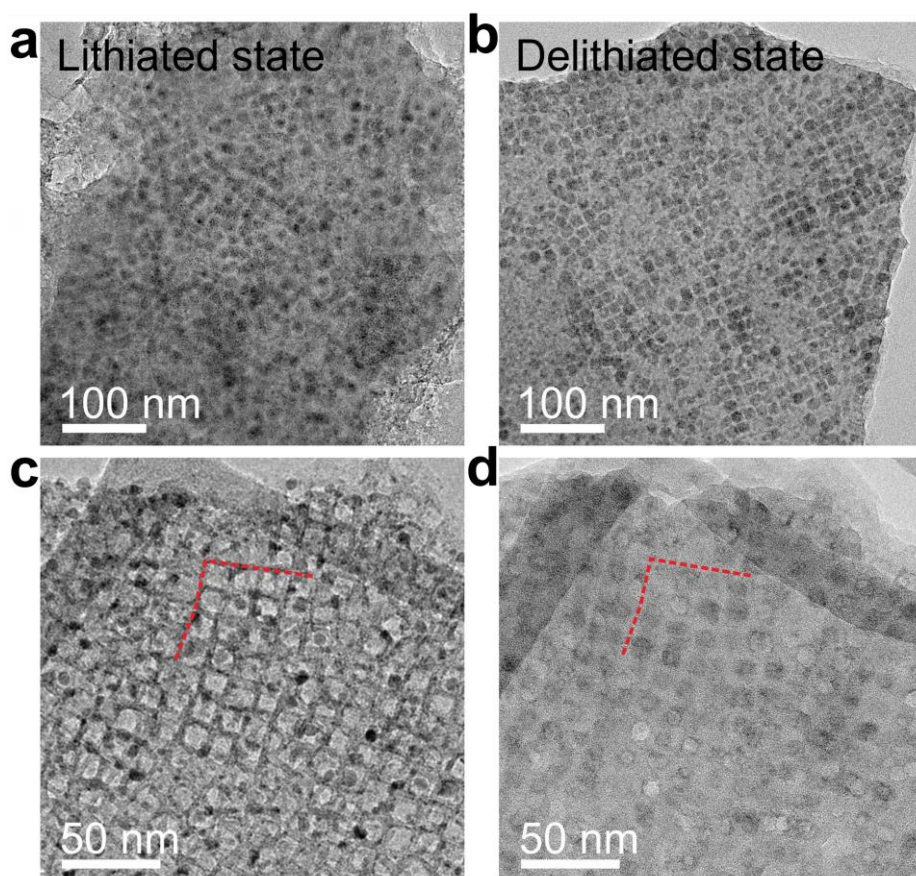


**Figure 2.14.** TEM analysis on the structural change of hybrid cellular nanosheets. TEM images of hybrid cellular nanosheets after (a) lithiation and (b) de-lithiation. TEM images of hybrid cellular nanosheets (c) before and (d) after one cycle of lithiation and de-lithiation from the same location. The red-dotted line indicates the same position on the nanosheet.

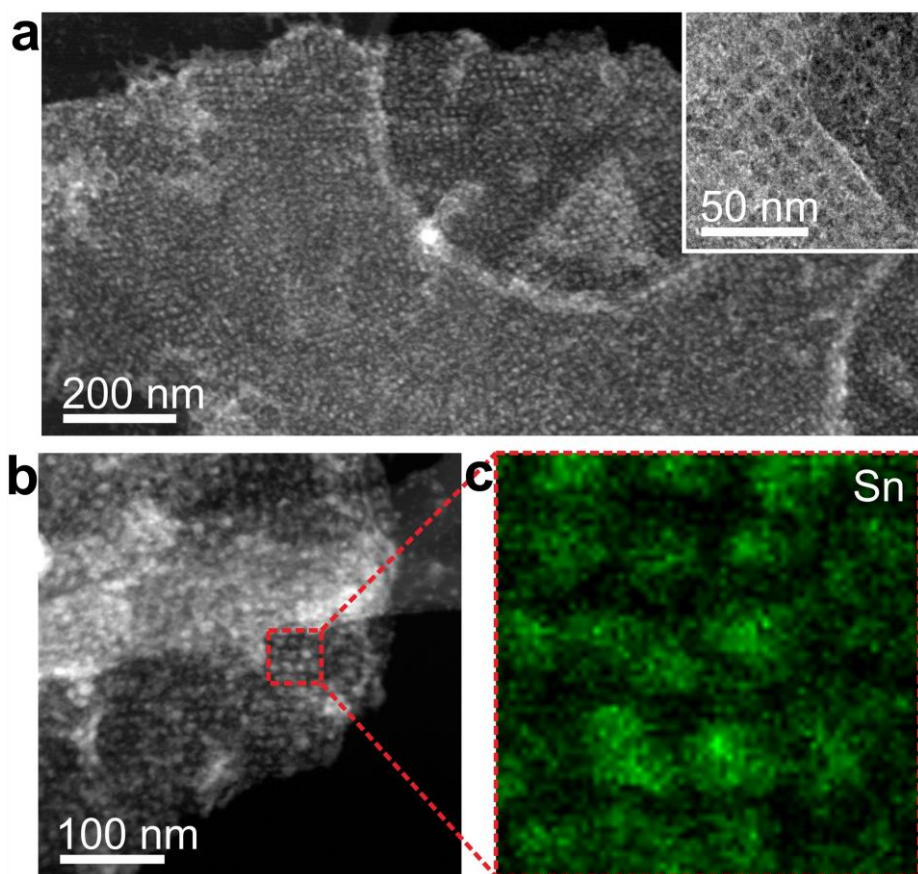


**Figure 2.15.** TEM analysis on the structural change of hybrid cellular nanosheets. (a) Dark-field scanning TEM image of hybrid cellular nanosheets after 20 cycles. The inset shows TEM image after 20 cycles. (b) Dark-field scanning TEM image and (c) EDX mapping of Sn L<sub>III</sub> edge after 20 cycles. The EDX mapping was performed in the red-dotted square in (b).

### 2.3.5 Structure-Induced Electrochemical Performances

TEM data discussed above reveal that the excellent electrochemical performances of SnO<sub>2</sub>-carbon cellular nanosheets are attributed to their unique hybrid structure (**Figure 2.17**). Because each cell has enough room for the volume change of SnO<sub>2</sub> NPs, the carbon wall does not exert mechanical stress to the SnO<sub>2</sub>-based active material confined in the cell even when the active material is fully lithiated to the maximum volume expansion. The cubic shape of the cells allows the higher packing density as well as the larger interface area of the loaded active material with carbon, compared to the spherical shape with the same volume. Well-ordered cellular structure of the nanosheets is rigid enough to confine the active material inside of the cell during cycling, keeping the mechanical integrity of the electrode film. Lithium ion diffusion length can be as short as 100 nm in the thickness direction of the nanosheets. At the same time, facile electron transport is possible through the carbon network of the nanosheets. Consequently, the structure of the hybrid cellular nanosheets is well-optimized for the high-performance anodes in terms of the specific capacity, cycling stability, and rate capability.

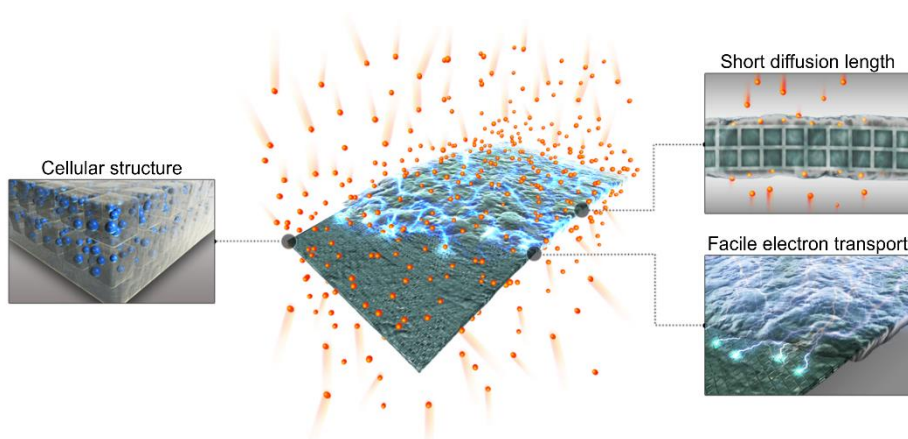


**Figure 2.16.** Illustration of a SnO<sub>2</sub>-carbon hybrid cellular nanosheet and its features that contribute to the electrochemical performance.

## 2.4 Conclusion

A practical synthetic method to prepare carbon nanosheets with cellular structure by a simple heating and etching procedure was developed. Carbon cellular nanosheets have unique cubic cavity cells forming well-ordered close-packed array. These cells can be easily loaded with inorganic active materials in various ways including “ship-in-a-bottle” method. Cellular nanosheets loaded with SnO<sub>2</sub> NPs showed outstanding electrochemical performance as LIB anodes. The specific capacity of SnO<sub>2</sub>-carbon hybrid nanosheets was 913.9 mAh g<sup>-1</sup> in average with the retention of 97.0% during 300 cycles. Also, when the cycling current density was increased from 200 mA g<sup>-1</sup> to 3000 mA g<sup>-1</sup>, the reversible capacity was decreased by only 20% from 941.3 mAh g<sup>-1</sup> to 745.5 mAh g<sup>-1</sup>. According to cyclic voltammetry, *in situ* XANES, and TEM analyses, such high performance is closely related to cellular structure of the hybrid nanosheets. The cubic cells provide enough room to accommodate the large volume change of the active material as well as the large interface area between the loaded active material and the carbon wall. As a result, the hybrid structure shows high reversibility of lithiation and de-lithiation. In addition, well-ordered rigid cellular nanosheet structure ensures the mechanical

integrity and facile lithium ion and electron transport. In conclusion, it is shown that very effective hybrid nanostructured electrode material can be prepared via a relatively simple procedure. Because the synthesis of carbon cellular nanosheets can be easily generalized to obtain various other nanostructures, it is highly expected that this approach would be applied to fabricate many kinds of hybrid nanostructured materials for extensive electrochemical device applications.

\* The contents of this chapter was published on *Journal of the American Chemical Society*.<sup>[68]</sup>



## 2.5 References

- [1] J.-M. Tarascon, M. Armand, *Nature* **2001**, 414, 359.
- [2] P. G. Bruce, S. A. Freunberger, L. J. Hardwick, J.-M. Tarascon, *Nat. Mater.* **2012**, 11, 19.
- [3] K. Kang, Y. S. Meng, J. Breger, C. P. Grey, G. Ceder, *Science* **2006**, 311, 977.
- [4] X. Zhao, B. M. Sánchez, P. J. Dobson, P. S. Grant, *Nanoscale* **2011**, 3, 839.
- [5] X. Ji, K. T. Lee, L. F. Nazar, *Nat. Mater.* **2009**, 8, 500.
- [6] Y. Chen, S. A. Freunberger, Z. Peng, O. Fontaine, P. G. Bruce, *Nat. Chem.* **2013**, 5, 489.
- [7] P. G. Bruce, B. Scrosati, J.-M. Tarascon, *Angew. Chem. Int. Ed.* **2008**, 47, 2930.
- [8] A. S. Aricò, P. Bruce, B. Scrosati, J.-M. Tarascon, W. van Schalkwijk, *Nat. Mater.* **2005**, 4, 366.
- [9] Y.-G. Guo, J.-S. Hu, L.-J. Wan, *Adv. Mater.* **2008**, 20, 2878.
- [10] H. B. Wu, J. S. Chen, H. H. Hng, X. W. Lou, *Nanoscale* **2012**, 4, 2526.
- [11] L. Ji, Z. Lin, M. Alcoutlabi, X. Zhang, *Energy Environ. Sci.* **2011**, 4, 2682.
- [12] C. K. Chan, H. Peng, G. Liu, K. McIlwrath, X. F. Zhang, R. A.

- Huggins, Y. Cui, *Nat. Nanotechnol.* **2008**, 3, 31.
- [13] R. Teki, M. K. Datta, R. Krishnan, T. C. Parker, T.-M. Lu, P. N. Kumta, N. Koratkar, *Small* **2009**, 5, 2236.
- [14] H. Wu, G. Chan, J. W. Choi, I. Ryu, Y. Yao, M. T. McDowell, S. W. Lee, A. Jackson, Y. Yang, L. Hu, Y. Cui, *Nat. Nanotechnol.* **2012**, 7, 310.
- [15] M.-H. Park, M. G. Kim, J. Joo, K. Kim, J. Kim, S. Ahn, Y. Cui, J. Cho, *Nano Lett.* **2009**, 9, 3844.
- [16] S. C. Jung, J. W. Choi, Y.-K. Han, *Nano Lett.* **2012**, 12, 5342.
- [17] X.-L. Wang, W.-Q. Han, H. Chen, J. Bai, T. A. Tyson, X.-Q. Yu, X.-J. Wang, X.-Q. Yang, *J. Am. Chem. Soc.* **2011**, 133, 20692.
- [18] M.-H. Park, Y. Cho, K. Kim, J. Kim, M. Liu, J. Cho, *Angew. Chem. Int. Ed.* **2011**, 50, 9647.
- [19] A. M. Chockla, K. C. Klavetter, C. B. Mullins, B. A. Korgel, *ACS Appl. Mater. Interfaces* **2012**, 4, 4658.
- [20] K. Kravchyk, L. Protesescu, M. I. Bodnarchuk, F. Krumeich, M. Yarema, M. Walter, C. Guntlin, M. V. Kovalenko, *J. Am. Chem. Soc.* **2013**, 135, 4199.
- [21] M.-S. Park, G.-X. Wang, Y.-M. Kang, D. Wexler, S.-X. Dou, H.-K. Liu, *Angew. Chem. Int. Ed.* **2007**, 46, 750.

- [22] X. W. Lou, Y. Wang, C. Yuan, J. Y. Lee, L. A. Archer, *Adv. Mater.* **2006**, *18*, 2325.
- [23] C. Kim, M. Noh, M. Choi, J. Cho, B. Park, *Chem. Mater.* **2005**, *17*, 3297.
- [24] J. Y. Huang, L. Zhong, C. M. Wang, J. P. Sullivan, W. Xu, L. Q. Zhang, S. X. Mao, N. S. Hudak, X. H. Liu, A. Subramanian, H. Y. Fan, L. A. Qi, A. Kushima, J. Li, *Science* **2010**, *330*, 1515.
- [25] J. Chen, L. Xu, W. Li, X. Gou, *Adv. Mater.* **2005**, *17*, 582.
- [26] M. V. Reddy, T. Yu, C. H. Sow, Z. X. Shen, C. T. Lim, G. V. Subba Rao, B. V. R. Chowdari, *Adv. Funct. Mater.* **2007**, *17*, 2792.
- [27] X.-L. Wu, Y.-G. Guo, L.-J. Wan, C.-W. Hu, *J. Phys. Chem. C* **2008**, *112*, 16824.
- [28] H. S. Kim, Y. Piao, S. H. Kang, T. Hyeon, Y.-E. Sung, *Electrochem. Commun.* **2010**, *12*, 382.
- [29] J. Vetter, P. Novák, M. R. Wagner, C. Veit, K.-C. Möller, J. O. Besenhard, M. Winter, M. Wohlfahrt-Mehrens, C. Vogler, A. Hammouche, *J. Power Sources* **2005**, *147*, 269.
- [30] P. G. Balakrishnan, R. Ramesh, T. Prem Kumar, *J. Power Sources* **2006**, *155*, 401.
- [31] P. Arora, R. E. White, M. Doyle, *J. Electrochem. Soc.* **1998**, *145*, 3647.

- [32] R. Zheng, X. Meng, F. Tang, L. Zhang, J. Ren, *J. Phys. Chem. C* **2009**, *113*, 13065.
- [33] N. Liu, H. Wu, M. T. McDowell, Y. Yao, C. Wang, Y. Cui, *Nano. Lett.* **2012**, *12*, 3315.
- [34] Z. Wang, D. Luan, S. Madhavi, Y. Hu, X. W. Lou, *Energy Environ. Sci.* **2012**, *5*, 5252.
- [35] X. W. Lou, C. M. Li, L. A. Archer, *Adv. Mater.* **2009**, *21*, 2536.
- [36] X. W. Lou, D. Deng, J. Y. Lee, L. A. Archer, *Chem. Mater.* **2008**, *20*, 6562.
- [37] Y.-S. Lin, J.-G. Duh, M.-H. Hung, *J. Phys. Chem. C* **2010**, *114*, 13136.
- [38] Y. Park, N.-S. Choi, S. Park, S. H. Woo, S. Sim, B. Y. Jang, S. M. Oh, S. Park, J. Cho, K. T. Lee, *Adv. Energy Mater.* **2013**, *3*, 206.
- [39] K. T. Lee, Y. S. Jung, S. M. Oh, *J. Am. Chem. Soc.* **2003**, *125*, 5652.
- [40] W.-M. Zhang, J.-S. Hu, Y.-G. Guo, S.-F. Zheng, L.-S. Zhong, W.-G. Song, L.-J. Wan, *Adv. Mater.* **2008**, *20*, 1160.
- [41] Y. Yu, L. Gu, C. Wang, A. Dhanabalan, P. A. van Aken, J. Maier, *Angew. Chem. Int. Ed.* **2009**, *48*, 6485.
- [42] J. Liang, X.-Y. Yu, H. Zhou, H. B. Wu, S. Ding, X. W. Lou, *Angew. Chem. Int. Ed.* **2014**, *53*, 12803.
- [43] S. Xin, Y.-G. Guo, L. J. Wan, *Acc. Chem. Res.* **2012**, *45*, 1759.

- [44] Y. Jiao, D. Han, L. Liu, L. Ji, G. Guo, J. Hu, D. Yang, A. Dong, *Angew. Chem. Int. Ed.* **2015**, *127*, 5819.
- [45] N. Liu, Z. Lu, J. Zhao, M. T. McDowell, H.-W. Lee, W. Zhao, Y. Cui, *Nat. Nanotechnol.* **2014**, *9*, 187.
- [46] A. Magasinski, P. Dixon, B. Hertzberg, A. Kvit, J. Ayala, G. Yushin, *Nat. Mater.* **2010**, *9*, 353.
- [47] S. H. Lee, S.-H. Yu, J. E. Lee, A. Jin, D. J. Lee, N. Lee, H. Jo, K. Shin, T. Y. Ahn, Y.-W. Kim, H. Choe, Y.-E. Sung, T. Hyeon, *Nano Lett.* **2013**, *13*, 4249.
- [48] X. Zhou, Y.-X. Yin, L.-J. Wan, Y.-G. Guo, *Adv. Energy Mater.* **2012**, *2*, 1086.
- [49] Y. Jiao, D. Han, Y. Ding, X. Zhang, G. Guo, J. Hu, D. Yang, A. Dong, *Nat. Commun.* **2015**, *6*, 6420.
- [50] S.-H. Yu, D. E. Conte, S. Baek, D.-C. Lee, S.-K. Park, K. J. Lee, Y. Piao, Y.-E. Sung, N. Pinna, *Adv. Funct. Mater.* **2013**, *23*, 4293.
- [51] J. Park, K. An, Y. Hwang, J.-G. Park, H.-J. Noh, J.-Y. Kim, J.-H. Park, N.-M. Hwang, T. Hyeon, *Nat. Mater.* **2004**, *3*, 891.
- [52] B. Jang, M. Park, O. B. Chae, S. Park, Y. Kim, S. M. Oh, Y. Piao, T. Hyeon, *J. Am. Chem. Soc.* **2012**, *134*, 15010.
- [53] P. Serna, B. C. Gates, *Acc. Chem. Res.* **2014**, *47*, 2612.

- [54] J. Lee, D. Lee, E. Oh, J. Kim, Y.-P. Kim, S. Jin, H.-S. Kim, Y. Hwang, J. H. Kwak, J.-G. Park, C.-H. Shin, J. Kim, T. Hyeon, *Angew. Chem. Int. Ed.* **2005**, *44*, 7427.
- [55] E. Kang, Y. S. Jung, A. S. Cavanagh, G.-H. Kim, S. M. George, A. C. Dillon, J. K. Kim, J. Lee, *Adv. Funct. Mater.* **2011**, *21*, 2430.
- [56] S. Zhu, H. Zhou, M. Hibino, I. Honma, M. Ichihara, *Adv. Funct. Mater.* **2005**, *15*, 381.
- [57] F.-D. Han, B. Yao, Y.-J. Bai, *J. Phys. Chem. C* **2011**, *115*, 8923.
- [58] C. Marichy, N. Donato, M.-G. Willinger, M. Latino, D. Karpinsky, S.-H. Yu, G. Neri, N. Pinna, *Adv. Funct. Mater.* **2011**, *21*, 658.
- [59] H. Wang, J. T. Robinson, G. Diankov, H. Dai, *J. Am. Chem. Soc.* **2010**, *132*, 3270.
- [60] D. Wang, X. Li, J. Wang, J. Yang, D. Geng, R. Li, M. Cai, T.-K. Sham, X. Sun, *J. Phys. Chem. C* **2012**, *116*, 22149.
- [61] S.-M. Paek, E. Yoo, I. Honma, *Nano Lett.* **2009**, *9*, 72.
- [62] Z. Wen, Q. Wang, Q. Zhang, J. Li, *Adv. Funct. Mater.* **2007**, *17*, 2772.
- [63] P. Wu, N. Du, H. Zhang, J. X. Yu, D. R. Yang, *J. Phys. Chem. C* **2010**, *114*, 22535.
- [64] J. Zhu, D. Lei, G. Zhang, Q. Li, B. Lu, T. Wang, *Nanoscale* **2013**, *5*, 5499.

- [65] I. A. Courtney, J. R. Dahn, *J. Electrochem. Soc.* **1997**, *144*, 2045.
- [66] F. Han, W.-C. Li, M.-R. Li, A.-H. Lu, *J. Mater. Chem.* **2012**, *22*, 9645.
- [67] H. Kim, G. O. Park, Y. Kim, S. Muhammad, J. Yoo, M. Balasubramanian, Y.-H. Cho, M.-G. Kim, B. Lee, K. Kang, H. Kim, J. M. Kim, W.-S. Yoon, *Chem. Mater.* **2014**, *26*, 6361.
- [68] S.-H. Yu, D. J. Lee, M. Park, S. G. Kwon, H. S. Lee, A. Jin, K.-S. Lee, J. E. Lee, M. H. Oh, K. Kang, Y.-E. Sung, T. Hyeon, *J. Am. Chem. Soc.* **2015**, *137*, 11954

# **Chapter 3. Facile Synthesis of Hexagon-shaped Metal (oxy)hydroxide Nanoplates and their Applications for Lithium Ion Battery Anode Materials**

## **3.1. Introduction**

The development of new electrode materials with higher energy density and improved cycling stability is being demanded by many industries to meet the increasing needs for rechargeable lithium ion batteries (LIBs).<sup>[1-8]</sup> Nanostructured transition metal oxides are considered promising candidates for LIB anode materials because they are environmentally friendly, have a high theoretical capacity, and are reasonably priced.<sup>[9-11]</sup> During lithiation, transition metal oxides are converted to metal nanoclusters and a Li<sub>2</sub>O matrix, which simultaneously leads to a huge volume expansion of ~300%.<sup>[9-11]</sup> This severe volume change during repeated lithiation and de-lithiation can cause a deterioration of the mechanical integrity of the electrode, resulting in poor capacity retention and safety problems for the cell. Hybrid nanomaterials made up of a high-capacity metal oxide core



and encapsulating carbon layers have received increasing attention as a possible solution, because they can effectively relieve mechanical stress and minimize side effects caused by structural deformation.<sup>[12-16]</sup>

Metal (oxy)hydroxides are also a focus in LIB development by many researchers because of their versatility. First, metal (oxy)hydroxide nanomaterials can act as a precursor for fabricating nanostructured metal oxides because they can be transformed to a metal oxide via a simple heat treatment.<sup>[17-24]</sup> In addition, nanocomposites of metal oxide nanocrystals and carbon can be obtained by synthesizing hybrid materials of metal (oxy)hydroxide and organic substrates followed by heat treatment.<sup>[16,25-26]</sup> Furthermore, metal (oxy) hydroxides themselves are attractive materials for energy devices including LIB electrodes,<sup>[27]</sup> supercapacitors,<sup>[28-30]</sup> and electrochemical catalysts.<sup>[31-34]</sup> Although a variety of metal (oxy)hydroxide nanostructures have been developed, these nanomaterials are generally fabricated using autoclave-based reactions that are time- and energy-consuming, thus mass production is difficult.<sup>[20-23,35-40]</sup> Besides, colloidal synthesis of multicomponent metal (oxy)hydroxide nanocrystals with controllable ratios have rarely been achieved.

Herein, we report a simple method to synthesize hexagon-shaped metal (oxy)hydroxide nanoplates and show their application to LIB anode electrodes. Metal (oxy)hydroxide nanoplates were synthesized under mild and aqueous conditions while avoiding time- and energy-consuming reactions. Moreover, this particular synthetic method is generally applicable to the fabrication of single-metallic (oxy)hydroxides (for example,  $\text{Co}(\text{OH})_2$ ,  $\text{MnO}(\text{OH})$ ,  $\text{FeO}(\text{OH})$ , and  $\text{Mg}(\text{OH})_2$ ), and mixed-metal (oxy)hydroxides. In addition, the atomic ratio of the metal species can be controlled by adjusting the precursor ratio. To utilize metal (oxy)hydroxide nanoplates as anode materials for LIBs, polydopamine was coated on  $\text{Co}(\text{OH})_2$  nanoplates in a controlled manner and converted to a nitrogen-doped carbon shell by heat treatment, where the transformation of  $\text{Co}(\text{OH})_2$  to mesoporous  $\text{CoO}$  simultaneously occurred.  $\text{CoO}@\text{C}$  nanocomposites with various carbon layer thicknesses were tested as LIB anodes in order to validate the effect of carbon coatings on electrochemical performance.  $\text{CoO}@\text{C}$  with a 6.5-nm-thick carbon shell exhibited higher reversible capacity and improved cycling stability compared with those having a thinner carbon shell. The experimental results suggest that the appropriate thickness of the carbon shell is important for improving

the cycling stability and minimizing side-reactions.

## **3.2. Experimental Section**

### **3.2.1 Chemicals**

Tetramethylammonium bromide (TMAB),  $\text{FeSO}_4 \cdot 7\text{H}_2\text{O}$ ,  $\text{MnCl}_2 \cdot 4\text{H}_2\text{O}$ ,  $\text{CoCl}_2 \cdot 6\text{H}_2\text{O}$ ,  $\text{MgSO}_4 \cdot \text{H}_2\text{O}$ , and dopamine hydrochloride were purchased from Sigma-Aldrich (USA). NaOH, hydrogen peroxide solution (34.5%) were obtained from Samchun Chemical (South Korea). Deionized water was obtained from a Milli-Q water purification system (Millipore, USA).

### **3.2.2 Synthesis of Hexagon-shaped Metal (oxy)hydroxide Nanoplates**

Before the synthesis, deionized water was degassed under vacuum to eliminate dissolved oxygen. To synthesize  $\text{Co}(\text{OH})_2$  nanoplates, 0.6 ml of NaOH aqueous solution (2 M) and 130 mg of TMAB were dissolved in 50 ml of  $\text{H}_2\text{O}$  and the solution was stirred vigorously. During the process, argon (or inert gas) was bubbled through the solution to remove dissolved air. The mixture was heated to 70 °C at a heating rate of 2 °C min<sup>-1</sup>. When the temperature reached 50 °C, 1.5 ml of  $\text{CoCl}_2$  solution (0.67 M, 238 mg of  $\text{CoCl}_2 \cdot 6\text{H}_2\text{O}$

dissolved in 1.5 ml of H<sub>2</sub>O) was quickly added. After the temperature reached 70 °C, the solution was further aged for 10 min and cooled to room temperature. To remove unreacted reagents and purify as-synthesized Co(OH)<sub>2</sub> nanoplates, the reacted solution were centrifuged and washed several times with H<sub>2</sub>O and ethanol. Finally, the product was dispersed in 50 ml of H<sub>2</sub>O. For the fabrication of various hexagon-shaped nanoplates such as MnO(OH), FeO(OH), Mg(OH)<sub>2</sub>, metal precursor was replaced to MnCl<sub>2</sub>·4H<sub>2</sub>O, FeSO<sub>4</sub>·7H<sub>2</sub>O, and MgSO<sub>4</sub>·H<sub>2</sub>O, while the other synthetic steps remained unchanged. In particular, when FeO(OH) nanoplates were prepared, 12 ml of 3% H<sub>2</sub>O<sub>2</sub> solution was added to the resulting solution containing Fe(OH)<sub>2</sub>, which led to the oxidation of Fe<sup>2+</sup> and the formation of δ-FeO(OH). For mixed-metal (oxy)hydroxide nanoplates, the desired ratio of metal precursors were mixed where the total concentration of metal ions was kept constant.

### **3.2.3 Polydopamine Coating on Metal (oxy)hydroxide Nanoplates and Transformation to Metal Oxide@Carbon Core-Shell Nanoplates**

The procedure to synthesize the MO<sub>x</sub>@C core-shell nanoplate

with ~20% carbon is as follows. Dopamine hydrochloride (72 mg) was added to the solution containing metal (oxy)hydroxide nanoplates and aged at room temperature for 20 h under rigorous stirring (For the FeO(OH)@polydopamine, 3 ml of 0.1 M NaOH solution was co-added as basic catalyst) to introduce a polymer coating on the nanoplates. After the reaction ended, the mixture was centrifuged and washed with H<sub>2</sub>O and ethanol to remove free-standing polydopamine. The final product was isolated via centrifugation and dried at 80 °C oven for 5 h. The dried powder was heated at 350 °C for 3 h under an inert atmosphere, where the metal (oxy)hydroxide and polymer were converted to metal oxide and carbon.

### **3.2.4 Characterization**

Transmission electron microscopy, scanning transmission electron microscopy, and energy-dispersive X-ray spectroscopy were performed using a JEOL JEM-2100F (Jeol) operated with Oxford EDS instrument. X-ray diffraction was carried out on a D/Max-3C diffractometer (Rigaku) equipped with a rotating anode and a Cu K $\alpha$  radiation source ( $\lambda = 1.5418 \text{ \AA}$ ). Elemental analyses were conducted by a Flash2000 elemental analyzer (Thermo scientific). Nitrogen

adsorption/desorption isotherm was measured by a 3FLEX surface characterization analyzer (Micromeritics).

### **3.2.5 Electrochemical Characterization**

Working electrodes were fabricated by coating copper foil with a slurry composed of active material, polyvinylidene fluoride (as a binder), and super P (as a conducting agent) (70:15:15 wt%) in *n*-methyl-2-pyrrolidinone (NMP) solvent, followed by drying overnight in a vacuum oven. After drying, the film on the copper foil was pressed using a roller to enhance the packing and contact of the electrode materials. To prevent air contamination, coin cells (2016 type) were assembled in a glove box under an inert atmosphere. 1.0 M LiPF<sub>6</sub> solution dissolved in a mixture of ethylene carbonate and diethyl carbonate with an equal volume ratio was used as the electrolyte. Lithium foil was used as a reference and counter electrode. The coin cells were galvanostatically charged and discharged in the potential range of 0.01–3.0 V (vs. Li<sup>+</sup>/Li) with a WBCS3000 cycler (WanA Tech, Korea). All the coin cell tests were carried out at a constant temperature of 25 °C.

### 3.3 Result and Discussion

#### 3.3.1 Synthesis and Characterization of Hexagon-shaped Metal (oxy)hydroxide Nanoplates

**Figure 3.1a** shows the transmission electron microscopy (TEM) image of hexagon-shaped  $\beta$ -Co(OH)<sub>2</sub> nanoplates, which were synthesized via a modified precipitation method under mild and aqueous conditions. When CoCl<sub>2</sub> was injected into the solution containing NaOH and tetramethylammonium bromide in an oxygen-free reaction medium, the Co<sup>2+</sup> cation rapidly reacted with the OH<sup>-</sup> anion, resulting in the formation of pink-colored  $\beta$ -Co(OH)<sub>2</sub> nanoplates. The average diameter and thickness of the  $\beta$ -Co(OH)<sub>2</sub> nanoplates were measured to be 122 and 9 nm, respectively. The X-ray diffraction (XRD) pattern of the  $\beta$ -Co(OH)<sub>2</sub> nanoplates clearly matched hexagonal  $\beta$ -Co(OH)<sub>2</sub> crystal structure (**Figure 3.1d**, JCPDS card no. 30-0443). It is worth mentioning that the full-width at half maximum (FWHM) of the peaks are different and depend on the (hkl) index of the peak. This discrepancy in the FWHM indicates a highly anisotropic structure for the  $\beta$ -Co(OH)<sub>2</sub> nanoplates.<sup>[41]</sup> A high-resolution TEM image demonstrated that the lateral face of the



hexagon-shaped nanoplates correlated with the (110) plane with a plane distance, where the lateral edge was matched with the [100] direction of  $\beta\text{-Co(OH)}_2$  (**Figure 3.1b**). Interestingly, a selected area electron diffraction (SAED) pattern of a single  $\beta\text{-Co(OH)}_2$  nanoplate has a six-fold point pattern, which indicates a highly crystalline nature for the  $\beta\text{-Co(OH)}_2$  nanoplates (**Figure 3.1c**). In addition to  $\beta\text{-Co(OH)}_2$  nanoplates, (oxy)hydroxide nanoplates consist of other metal components could also be synthesized only by changing the metal precursor while keeping other synthetic conditions unchanged. **Figure 3.2a-c** show TEM images of hexagon-shaped  $\text{MnO(OH)}$ ,  $\text{FeO(OH)}$ , and  $\text{Mg(OH)}_2$  nanoplates. Similar to  $\beta\text{-Co(OH)}_2$  nanoplates, other metal (oxy)hydroxide also have hexagonal shapes and high crystallinity. For manganese oxyhydroxide, as-synthesized  $\text{Mn(OH)}_2$  nanoplates were oxidized during the washing step, which was confirmed by the color change of products from milk-white to brown.<sup>[42]</sup> When as-synthesized  $\text{Fe(OH)}_2$  nanoplates were exposed to air, an undesirable dissolution-recrystallization process of iron hydroxide took place, which led to the deformation of the original structure.<sup>[43]</sup> To prevent structural degradation, a hydrogen peroxide solution was added to the reacted solution to oxidize the as-

synthesized  $\text{Fe}(\text{OH})_2$  and terminate the dissolution-recrystallization process, resulting in the formation of  $\delta\text{-FeO}(\text{OH})$  without any noticeable structural deformation. Crystal structures of (oxy)hydroxide nanoplates were characterized by XRD measurements (**Figure 3.3a-c**). During the formation of metal (oxy)hydroxide nanoplates, the elimination of oxygen from the reaction media is necessary. When the same procedure was performed in air, a mixture of nanoplates and nanoparticles was obtained. XRD data confirmed that metal oxides were formed rather than metal (oxy)hydroxide (**Figure 3.4**). Reactions of metal ions with hydroxide ions in an aqueous solution are shown in Eq. (1), (2), and (3).<sup>[44]</sup>



In the absence of oxygen, reaction (2) and (3) are hardly noticeable, and metal hydroxide was the main product. In the presence of oxygen, however, reaction (2) and (3) were accelerated, resulting in the formation of metal oxide.

Interestingly, mixed-metal (oxy)hydroxides could be synthesized using the same procedure with a mixture of metal precursors at a

specific ratio. TEM images of mixed-metal (oxy)hydroxides demonstrated that all of the mixed-metal (oxy)hydroxide nanoplates have hexagonal shapes (**Figure 3.2d-i** for Co-Mn, Co-Fe, Mn-Fe, Co-Mg, Co-Mn-Fe, and Co-Mn-Fe-Mg (oxy)hydroxide nanoplates, respectively). XRD patterns of multi-metal (oxy)hydroxides in **Figure 3.3d-i** also show that there was no evidence of the heterogeneous formation of (oxy)hydroxides. Energy-dispersive X-ray spectroscopy (EDX) elemental mapping for mixed-metal (oxy)hydroxides indicate that metal species are uniformly distributed in the nanoplates (**Figure 3.5 and 3.6**). We concluded that the growth kinetics and lattice mismatches of metal hydroxides are in a comparable range, where distinct difference in the kinetics and/or lattice parameters results in the formation of separate (oxy)hydroxides or heterogeneous (oxy)hydroxides. Ratios between the metal species in multi-metal (oxy)hydroxides measured by EDX are close to the initial values. These results corroborate the versatility of a synthetic method that is easy, reproducible, scalable, and applicable for fabricating various metal (oxy)hydroxide nanoplates. To further investigate the homogeneity of mixed-metal (oxy)hydroxides, SAED and energy-filtered TEM (EFTEM) elemental mapping were performed on a

single nanoplate of a mixed-metal (oxy)hydroxide. **Figure 3.7** and **Figure 3.8** show that every metal species are uniform distributed along a nanoplate composing single crystal structure.

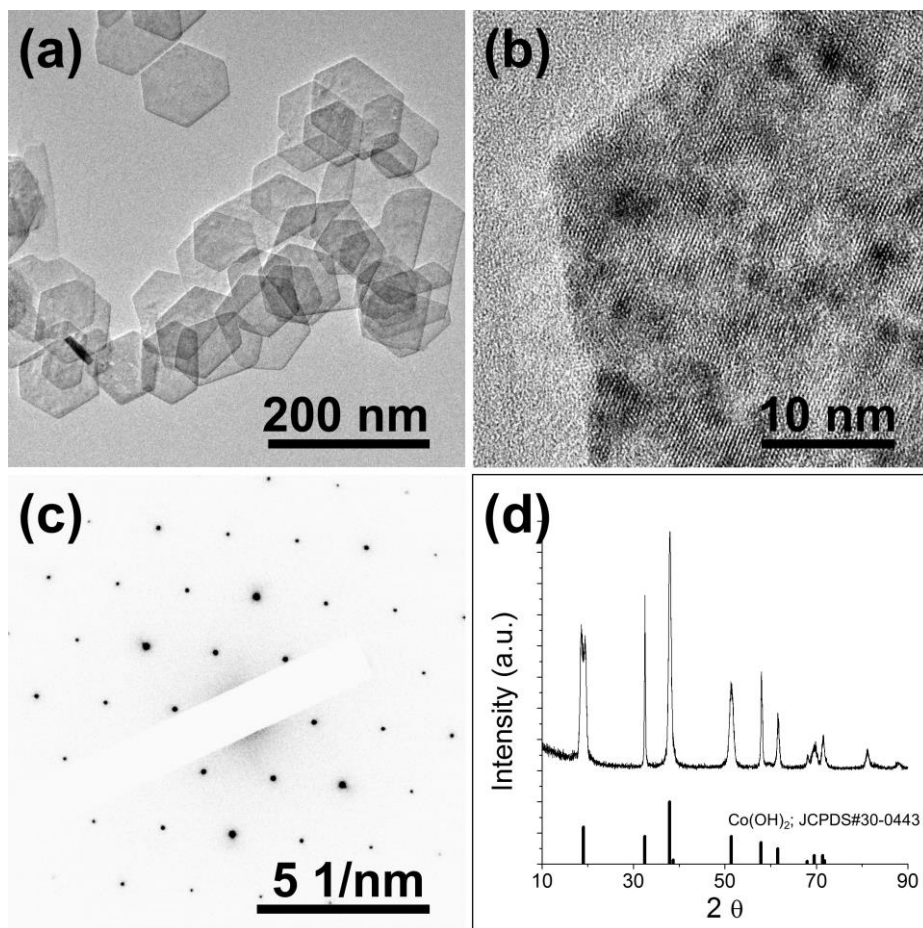


**Figure 3.1.** (a) TEM and (b) high-resolution TEM image of hexagonal-shaped  $\text{Co(OH)}_2$  nanoplates. (c) Selected-area electron diffraction (SAED) pattern of a single nanoplate. (d) XRD data of  $\text{Co(OH)}_2$  nanoplates.

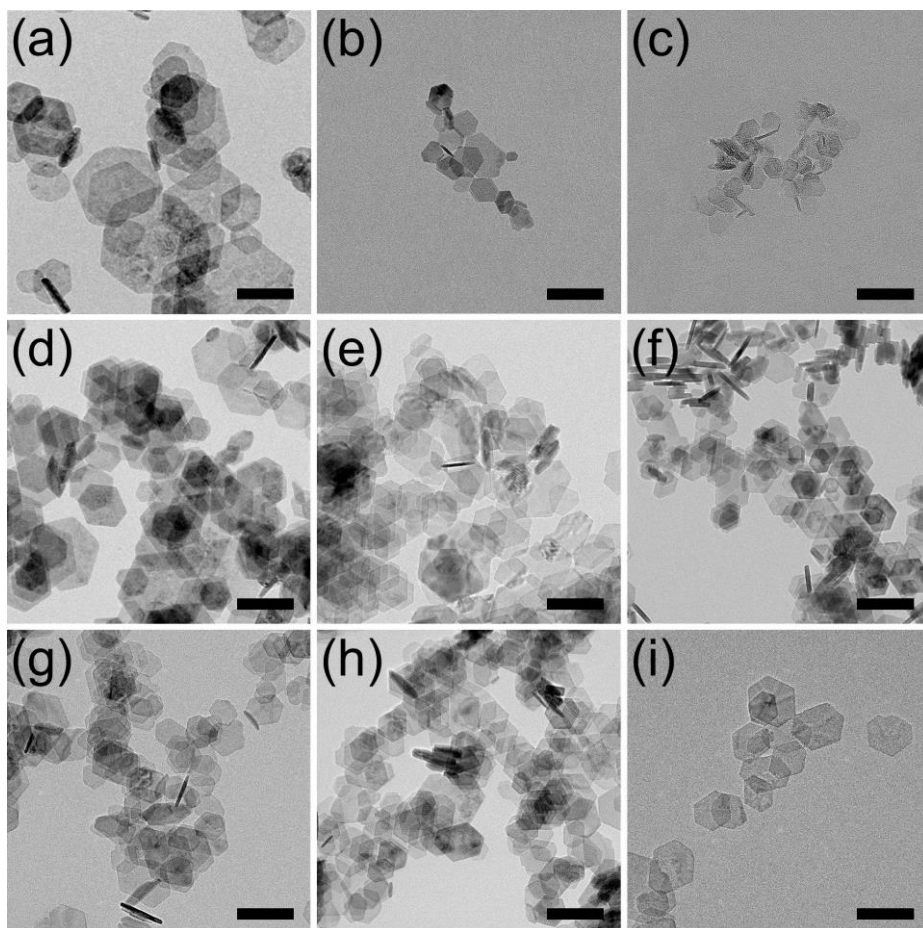


**Figure 3.2.** TEM images of metal (oxy)hydroxide nanoplates with various combination. (a) Mn, (b) Fe, (c) Mg, (d) Co-Mn, (e) Co-Fe, (f) Mn-Fe, (g) Co-Mg, (h) Co-Mn-Fe, and (i) Co-Mn-Fe-Mg. Scale bars in (a-i) indicate 100 nm.

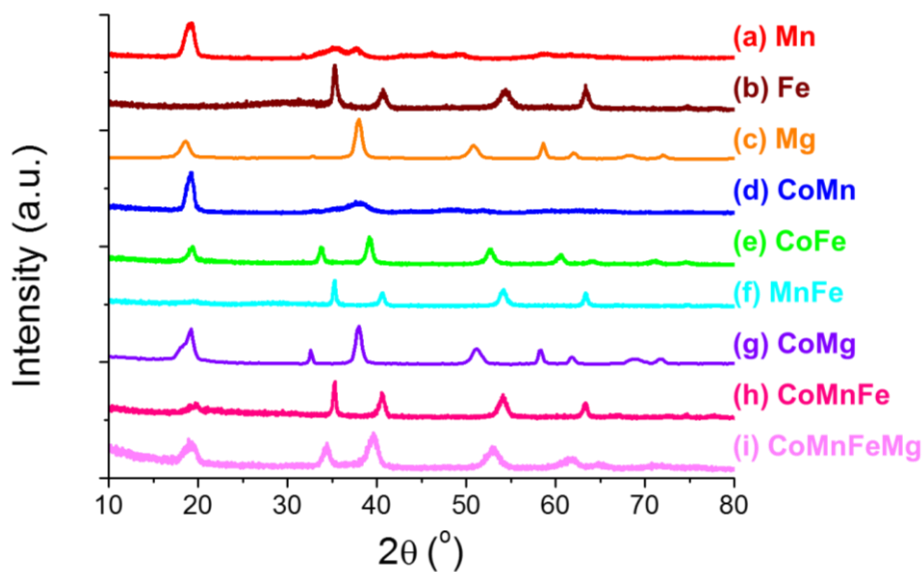


**Figure 3.3.** XRD data of various metal (oxy)hydroxide nanoplates. (a) Mn, (b) Fe, (c) Mg, (d) Co-Mn, (e) Co-Fe, (f) Mn-Fe, (g) Co-Mg, (h) Co-Mn-Fe, and (i) Co-Mn-Fe-Mg.

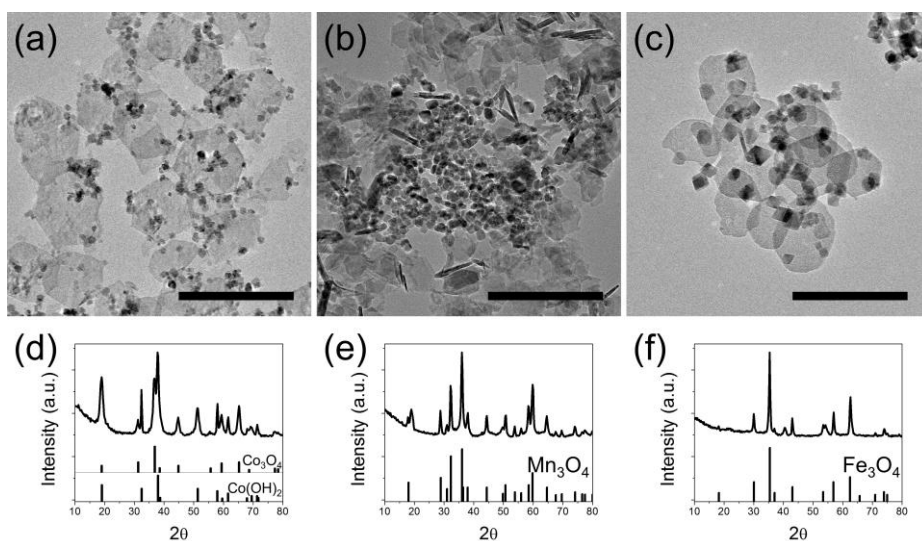


**Figure 3.4.** (a-c) TEM image and (d-f) XRD data of nanoparticles obtained under an air atmosphere. (a,d) Cobalt, (b,e) manganese, and (c,f) iron. Scale bars in (a-c) indicate 200nm.



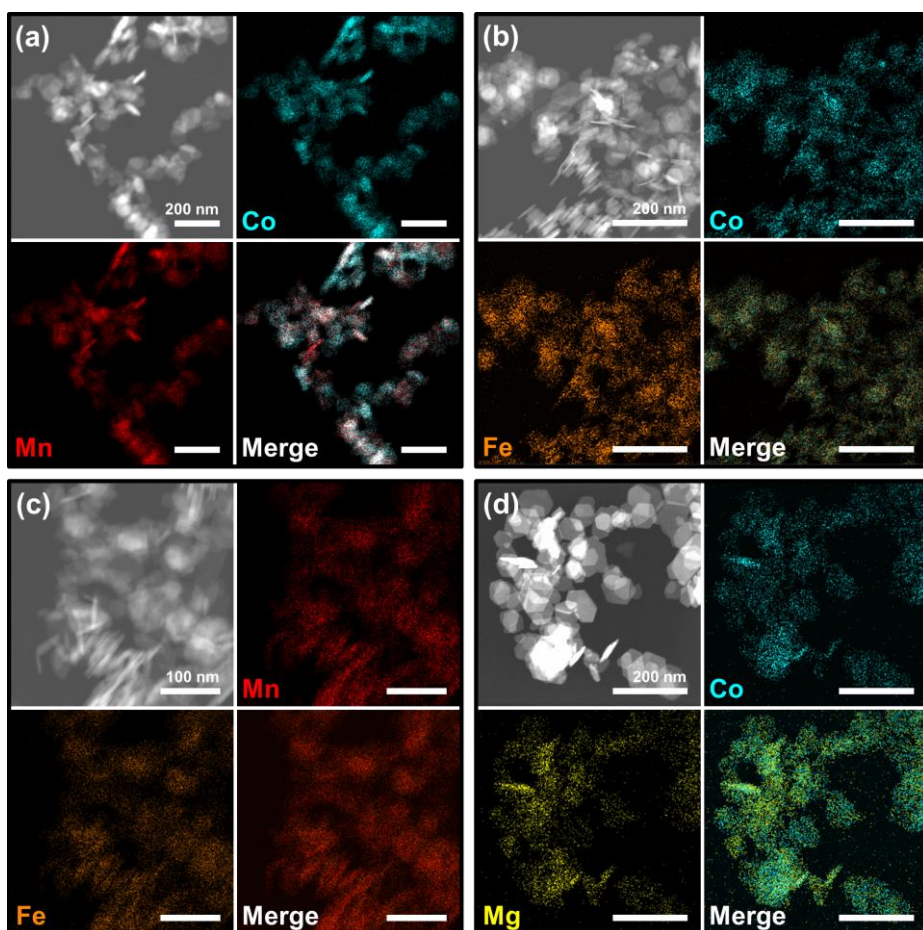


**Figure 3.5.** Dark-field STEM image and corresponding EDX elemental mapping images of various mixed-metal (oxy)hydroxide nanoplates. (a) Co-Mn, (b) Co-Fe, (c) Mn-Fe, and (d) Co-Mg.

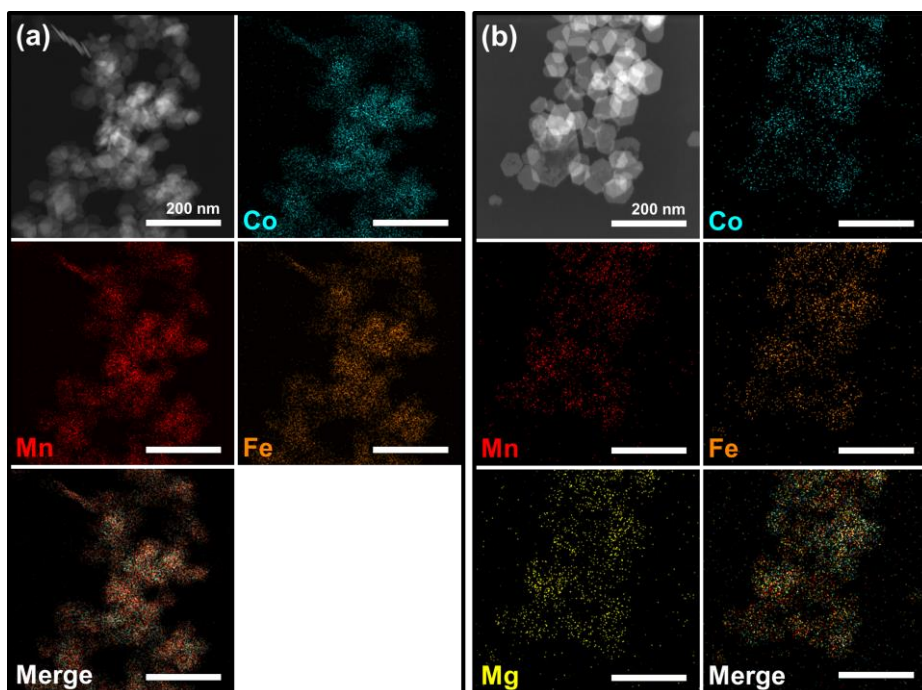


**Figure 3.6.** Dark-field STEM image and corresponding EDX elemental mapping images of various mixed-metal (oxy)hydroxide nanoplates. (a) Co-Mn-Fe and (b) Co-Mn-Fe-Mg.

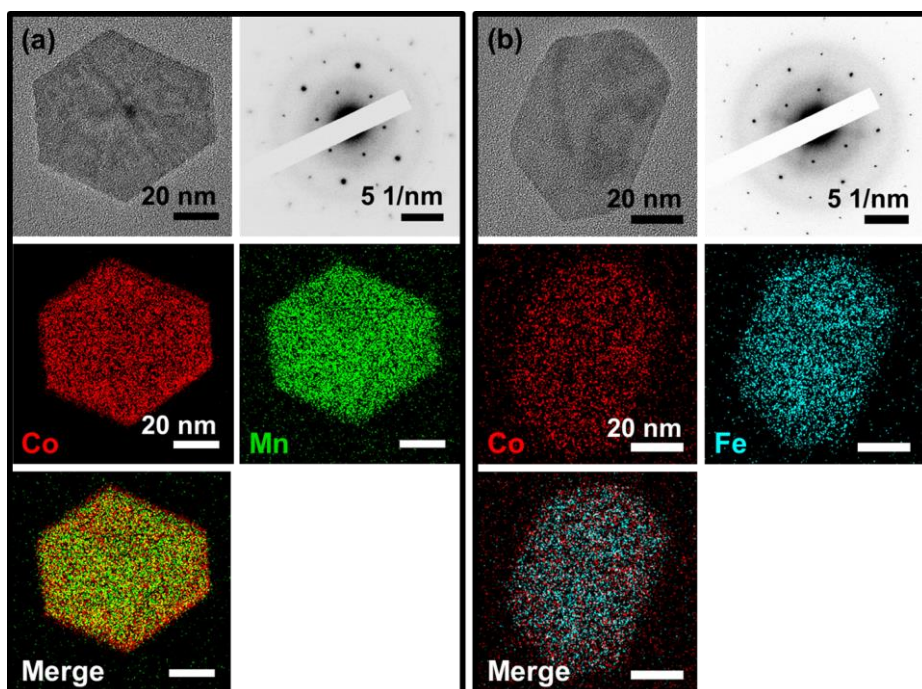


**Figure 3.7.** TEM image, SAED pattern, and corresponding EFTEM images of mixed-metal (oxy)hydroxide nanoplates. (a) Co-Mn and (b) Co-Fe.

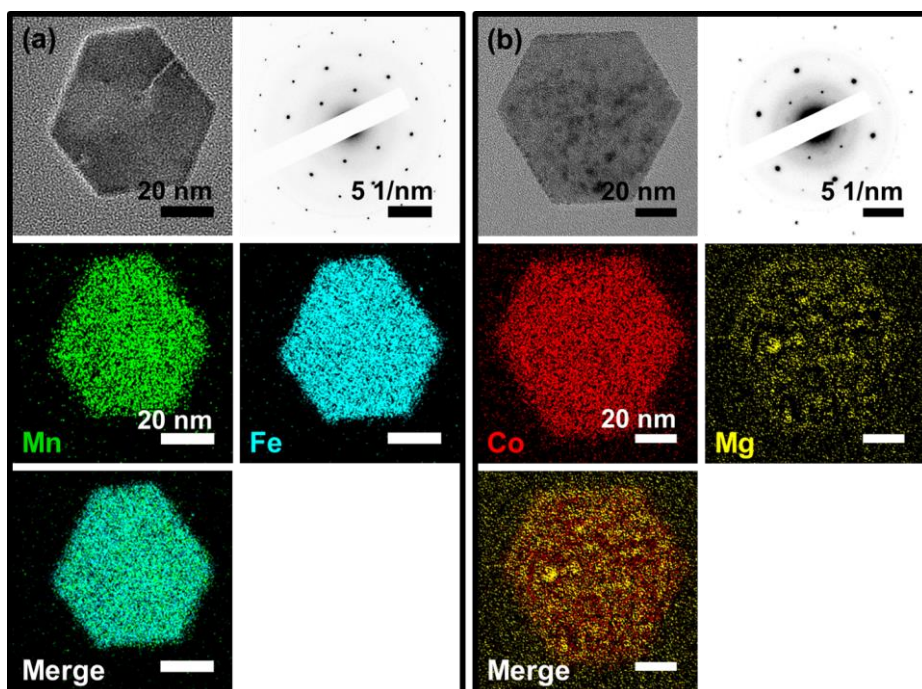


**Figure 3.8.** TEM image, SAED pattern, and corresponding EFTEM images of mixed-metal (oxy)hydroxide nanoplates. (a) Mn-Fe and (b) Co-Mg.



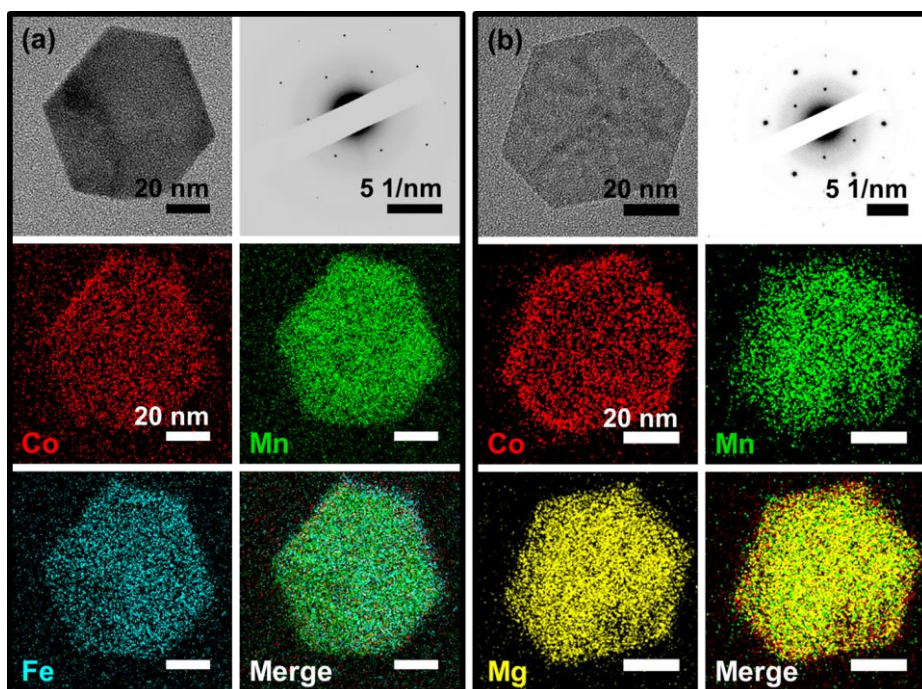


**Figure 3.9.** TEM image, SAED pattern, and corresponding EFTEM images of mixed-metal (oxy)hydroxide nanoplates. (a) Co-Mn-Fe and (b) Co-Mn-Mg.

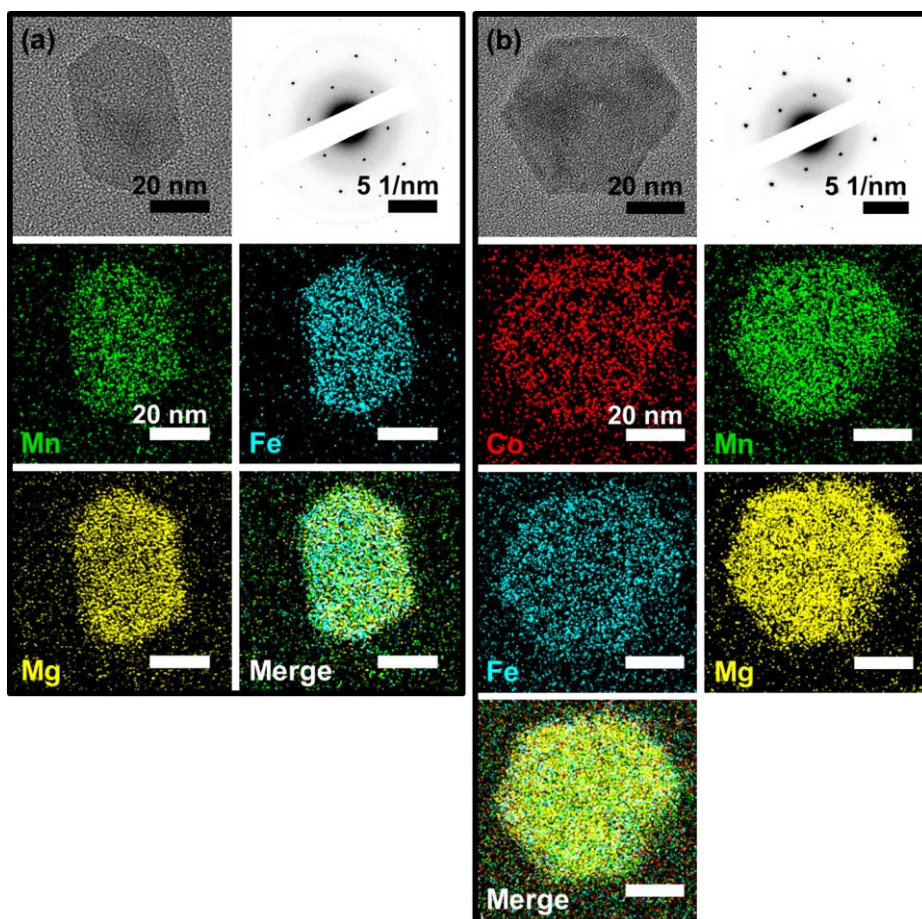


**Figure 3.10.** TEM image, SAED pattern, and corresponding EFTEM images of mixed-metal (oxy)hydroxide nanoplates. (a) Mn-Fe-Mg and (b) Co-Mn-Fe-Mg.

### 3.3.2 Synthesis of CoO@C Core–Shell Nanoplates

In addition, metal oxide nanoplates were prepared using metal (oxy)hydroxide nanoplates as precursors, and utilized as LIB anodes. As mentioned above, it is widely believed that carbon coatings on metal oxide nanocrystals can improve the cycling performance of active materials.<sup>[12-16]</sup> From this point-of-view, polydopamine is a promising carbon source. Polydopamine, a “mussel-inspired” polymer, has been widely used as a coating agent because it has good adhesion to many materials.<sup>[45-46]</sup> In addition, polydopamine is converted to nitrogen-doped carbon during heat treatment, which has been used in many energy and environmental applications, such as LIB electrodes, oxygen reduction catalysts, CO<sub>2</sub>-capturing substrates, and supercapacitors.<sup>[46]</sup> To introduce a polydopamine coating on metal (oxy)hydroxide nanoplates, dopamine hydrochloride was added to an aqueous solution containing Co(OH)<sub>2</sub> nanoplates and polymerized. Although the polymerization of dopamine normally occurs in weakly basic conditions (pH~8.5), an additional base catalyst is not required for Co(OH)<sub>2</sub> nanoplates, which demonstrates that Co(OH)<sub>2</sub> nanoplates themselves act as a catalyst for the polymerization of dopamine. **Figure 3.11a-c** and **Figure 3.12** show TEM images of polydopamine-

coated  $\text{Co}(\text{OH})_2$  nanoplates with different polydopamine thicknesses. By changing the amount of dopamine hydrochloride, different thicknesses of polydopamine coatings ranging from 2 to 12 nm were obtained. The morphology, crystal structure, and highly crystalline nature of  $\text{Co}(\text{OH})_2$  nanoplates are preserved after polymerization. In order to enhance the electrochemical properties, as-synthesized  $\text{Co}(\text{OH})_2$ @polydopamine core-shell nanoplates were heated to  $350^\circ\text{C}$ .  $\text{Co}(\text{OH})_2$  and polydopamine are converted to  $\text{CoO}$  and nitrogen-doped carbon, respectively. **Figure 3.11d-f** represent TEM images of  $\text{CoO@C}$  core-shell composites after heat treatment. Broad peaks in the XRD patterns of the final products are assigned to the cubic  $\text{CoO}$  crystal structure (JCPDS card no. 43-1004, **Figure 3.13**). Thicknesses of the carbon shells in **Figure 3.11d-f** are 1.5 nm, 3.8 nm, and 6.5 nm, respectively. ( $\text{CoO@C}$  nanocomposites with a carbon shell of 1.5 nm, 3.8 nm, and 6.5 nm thickness are denoted as  $\text{CoO@C-1}$ ,  $\text{CoO@C-2}$ , and  $\text{CoO@C-3}$ . See Table 3.1 for CHN elemental analysis data of these  $\text{CoO@C}$  nanocomposites). When the large-scale synthesis was conducted, 1.5 g of  $\text{CoO@C-3}$  can be obtained from a single batch (**Figure 3.14**). Interestingly, when  $\text{Co}(\text{OH})_2$  was converted to  $\text{CoO}$ , core  $\text{CoO}$  exhibited a mesoporous structure while hexagon-shaped and

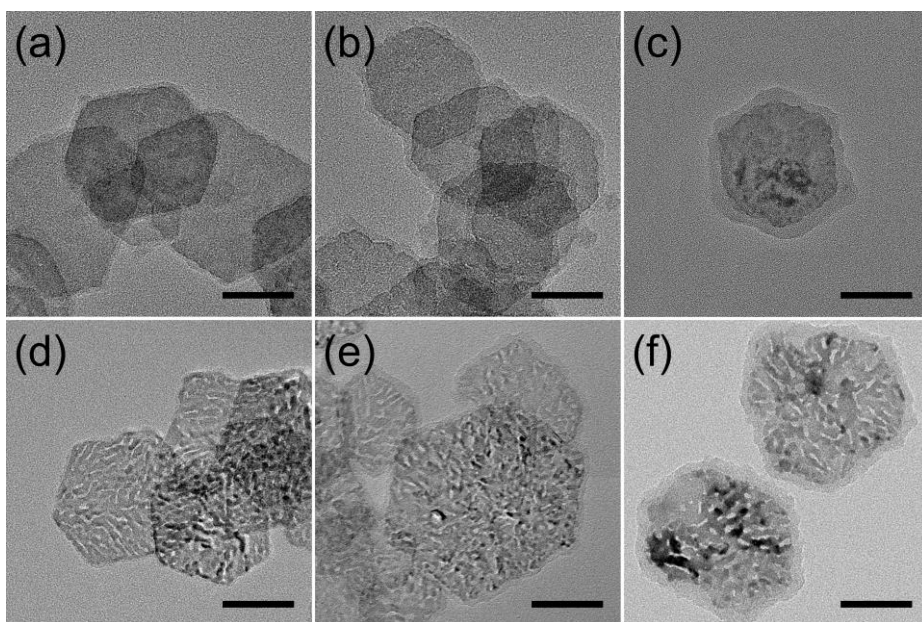


plate-like morphology were still maintained. The reason for forming mesopores in CoO nanoplates originated from the elimination of water in the crystal structure of Co(OH)<sub>2</sub>. When Co(OH)<sub>2</sub> is heated, the reaction shown in Eq. (4) takes place.



The elimination of water is simultaneously accompanied with 19.4% mass loss and 41.4% volume shrinkage, resulting in the formation of mesopores inside of the CoO nanoplates. To characterize the pore size distribution and surface area of CoO@C nanocomposites, N<sub>2</sub> adsorption and desorption isotherm measurements were carried out (**Figure 3.15**). The surface area of CoO@C-1, CoO@C-2, and CoO@C-3 are 91.8, 86.1, and 52.1 m<sup>2</sup> g<sup>-1</sup>, respectively. Mesopores sized about 3.5 nm are assigned from the Barrett-Joyner-Halenda (BJH) pore size distribution of CoO@C-1 and CoO@C-2, whereas a peak is hardly visible in a pore distribution of CoO@C-3 although a TEM image of CoO@C-3 clearly shows a mesoporous structure. This phenomena can be explained by a micropore filling effect. When N<sub>2</sub> adsorption isotherm is measured, micropores in carbonaceous materials are filled with N<sub>2</sub> molecule at a low relative pressure ( $P/P_0 < 0.2$ ), where mesopores form at a high relative pressure ( $P/P_0 > 0.8$ ).

For CoO@C with a thick carbon shell, micropores in the carbon shell are blocked before mesopores are filled up, and N<sub>2</sub> condensation in the mesopores inside the carbon shell is hampered by the thick carbon shell. It is noteworthy that the mesoporous structure with free space is advantageous when CoO@C nanocomposites are utilized as LIB anodes because the free space can better accommodate volume change during lithiation/de-lithiation.



**Figure 3.11.** (a-c) TEM image of  $\text{Co(OH)}_2$ @polydopamine with (a) 1.5 nm, (b) 3.8 nm, and (c) 6.5 nm. (d-f) TEM image of (d)  $\text{CoO@C-1}$ , (e)  $\text{CoO@C-2}$ , and (f)  $\text{CoO@C-3}$  after heat treatment. Scale bars in (a-f) indicate 50 nm.

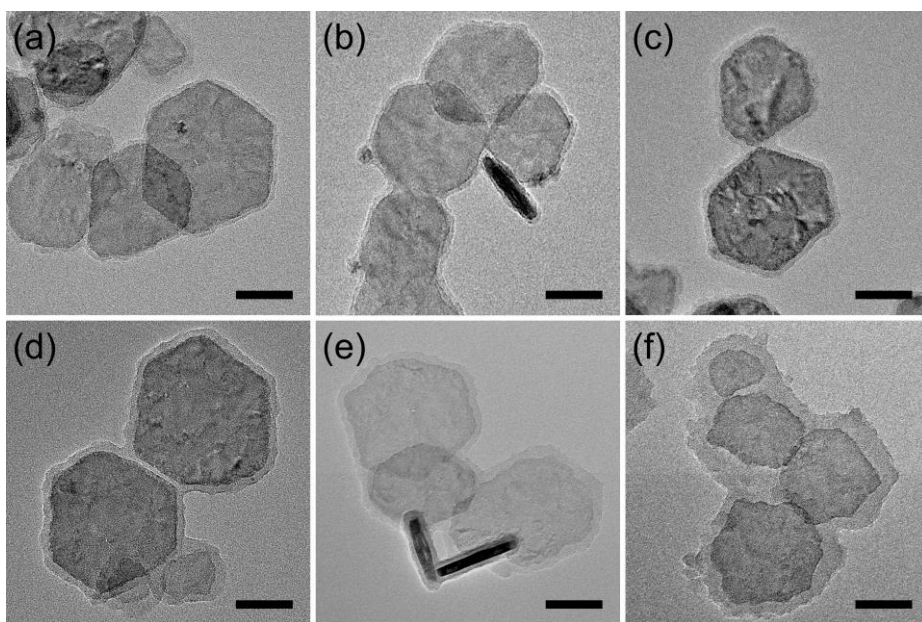


**Figure 3.12.** (a-f) TEM images of  $\text{Co(OH)}_2$ @polydopamine core-shell nanoplates with various thicknesses of the polydopamine shell. Scale bars in (a-f) indicate 50 nm.

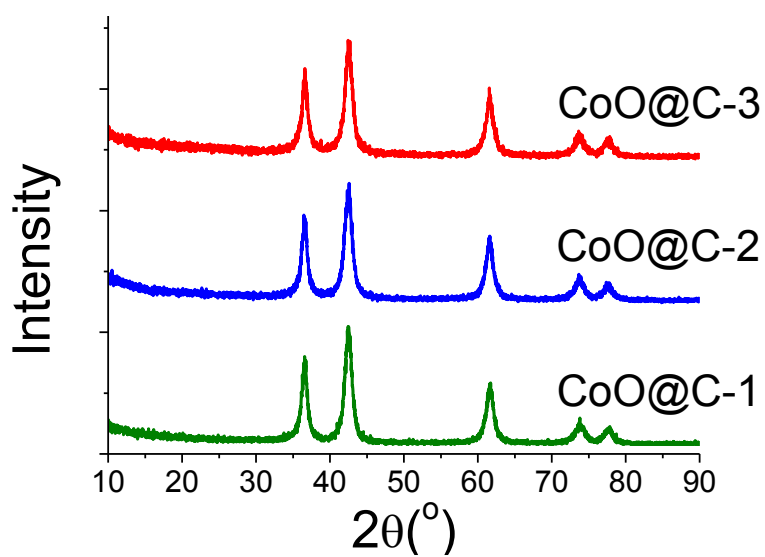


**Figure 3.13.** XRD patterns of CoO@C with various carbon shell thicknesses.

**Table 3.1.** CHN elemental analysis data for CoO@C

	Carbon (wt%)	Hydrogen (wt%)	Nitrogen (wt%)	Total (wt%)
CoO@C-1	6.286	0.423	0.834	7.543
CoO@C-2	15.071	0.758	2.020	17.869
CoO@C-3	25.404	1.161	3.346	29.911

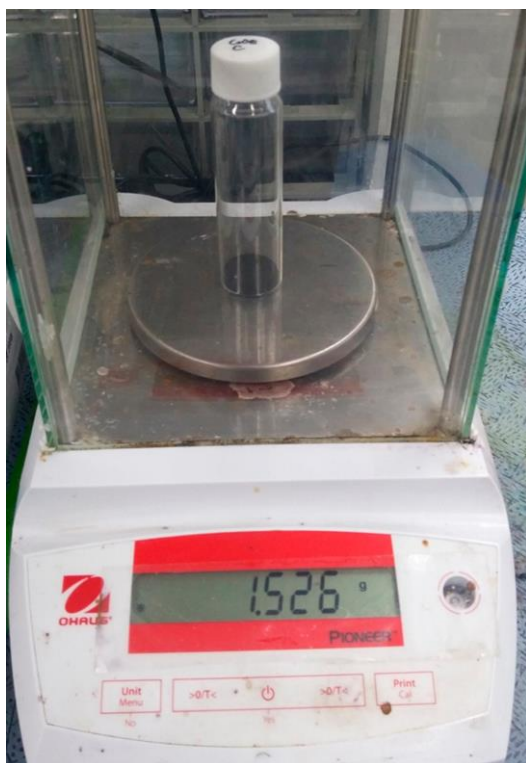


**Figure 3.14.** Large-scale synthesis of CoO@C-3. From a single batch, ~1.5 g of CoO@C was obtained.

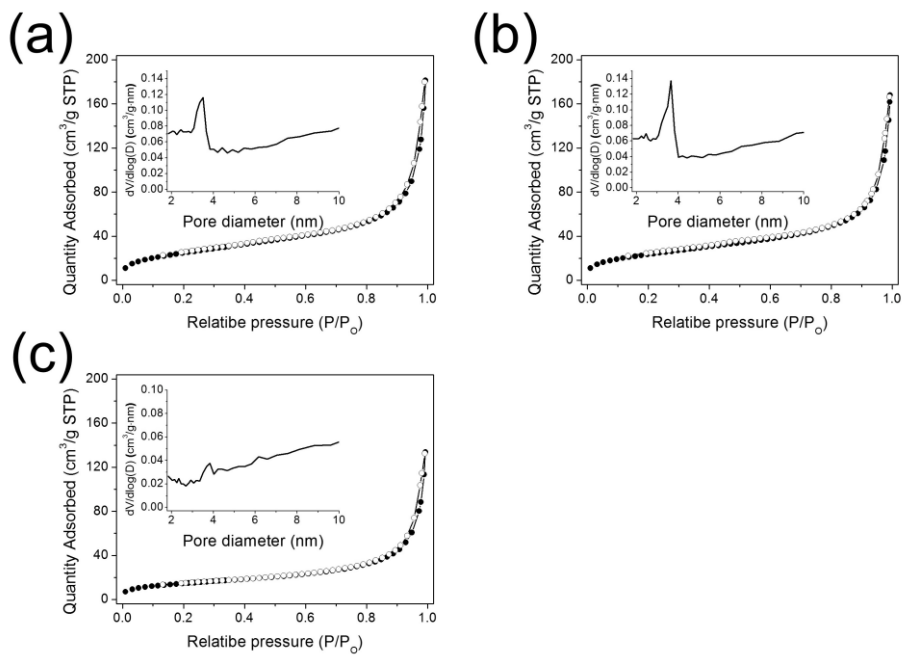


**Figure 3.15.**  $N_2$  adsorption and desorption isotherms and the corresponding pore size distribution of (a)  $CoO@C-1$ , (b)  $CoO@C-2$ , and (c)  $CoO@C-3$ .



### 3.3.3 Electrochemical performance of CoO@C

To evaluate the thickness-dependent electrochemical performance of CoO@C nanocomposites, the cycling performance and rate capability were investigated by galvanostatic charge–discharge in a voltage range of 0.01–3.0 V (vs. Li<sup>+</sup>/Li). **Figure 3.16a** shows the cycling performance of CoO@C nanocomposites at a current density of 200 mA g<sup>-1</sup> for 100 cycles. During the first several cycles, the capacity of CoO@C-1 quickly increased. This tendency has often been observed in other cobalt oxide-based LIB anode materials.<sup>[36, 47-48]</sup> After the capacity reached its highest value, the capacity continuously decreased from 1257.0 mAh g<sup>-1</sup> (18th cycle) to 314.9 mAh g<sup>-1</sup> (100th cycle). On the other hand, CoO@C-2 and CoO@C-3 did not show such a rapid change in capacity. CoO@C-2 exhibited high capacity and good cycling stability during early cycling, demonstrating 1013.1 mAh g<sup>-1</sup> of discharge capacity at the 50th cycle. However, after the 50th cycle, the capacity gradually declined and reached to 632.6 mAh g<sup>-1</sup> at the 100th cycle. In comparison with CoO@C-1 and CoO@C-2, CoO@C-3 with a 6.5-nm-thick carbon shell showed a higher capacity and excellent cycling stability during 100 cycles, resulting in 1016.2 mAh g<sup>-1</sup> of specific capacity at the

100th cycle and an average capacity of 992.9 mAh g<sup>-1</sup> during that period. To examine the rate performance of CoO@C nanocomposites, current densities were varied from 100 to 200, 400, 800, and 1600 mA g<sup>-1</sup> (**Figure 3.16b**). At lower current densities, the capacity of CoO@C-1 gradually increased, where similar phenomena was observed in **Figure 3.16a**. However, at higher current densities, the capacity dramatically decreased to 454 mAh g<sup>-1</sup> (at 800 mA g<sup>-1</sup>) and 215 mAh g<sup>-1</sup> (at 1600 mA g<sup>-1</sup>) on average. In contrast, CoO@C-3 retained its capacities, yielding 943 mAh g<sup>-1</sup>, 920 mAh g<sup>-1</sup>, 882 mAh g<sup>-1</sup>, 801 mAh g<sup>-1</sup>, and 603 mAh g<sup>-1</sup> on average at current densities of 100 mA g<sup>-1</sup>, 200 mA g<sup>-1</sup>, 400 mA g<sup>-1</sup>, 800 mA g<sup>-1</sup>, and 1600 mA g<sup>-1</sup>, respectively. Interestingly, when a current density recovered to 100 mA g<sup>-1</sup> after the 50<sup>th</sup> cycle, CoO@C-3 exhibited stable capacity retention over 1000 mAh g<sup>-1</sup>, while the capacity of CoO@C-1 continuously decreased.

This improved electrochemical performance can be explained by the thickness-dependent morphology retention of CoO@C nanocomposites. It has been widely known that the conversion reaction induces a huge amount of volume change (~300%) during lithiation/de-lithiation, and generally causes the deterioration of

capacity upon cycling. In addition, mechanical stress can cause the fracture or pulverization of active materials, which causes undesired capacity increases by capturing lithium ions, which generates an SEI layer on newly exposed surfaces. Carbon coating can effectively prevent the pulverization or cracking of active materials and results in enhanced electrochemical properties.

In order to directly observe cycling-induced morphological changes, TEM analysis was conducted after cycling. **Figure 3.17a-f** show TEM images of CoO@C-1 and CoO@C-3 after 50 cycles of lithiation/de-lithiation. As can be seen in these TEM images, all samples lose their original mesoporous structure and are converted to small nanoparticles in the surrounding matrix, indicating the conversion reaction took place. For CoO@C-1, the core CoO nanoplates are collapsed and the original hexagonal shapes are not found in spite of the 1.5-nm-thick carbon shell (**Figure 3.17a-c**). It is considered that the thin carbon shell is not sufficient to resist the volume change-induced mechanical stress, hence the breakage during repeated lithiation/de-lithiation. When the active materials are broken up, a newly exposed interface is generated. Lithium ions and electrolyte are additionally consumed to form a new SEI layer on the

interface, resulting in a lower Coulombic efficiency. This breakage also causes the pulverization and aggregation of CoO, and the capacity of the electrode gradually declines. On the other hand, TEM images of CoO@C-3 reveal that plate-like morphology and hexagonal shape of core CoO are well maintained even after 50 cycles (**Figure 3.17d-f**). The dark-field STEM image and corresponding EDX elemental mappings also confirm that no significant deformation or pulverization was observed in cobalt-based active materials (**Figure 3.17g-i**). This result is the reason why CoO@C-3 shows enhanced electrochemical performance, in terms of cycling stability and Coulombic efficiency, compared with CoO@C nanocomposites with a thinner carbon shell. This result suggests that a certain thickness of carbon shell is required to resist the mechanical stress that is built during the conversion reaction. In addition to the CoO@C nanocomposites, MnO@C and Fe<sub>3</sub>O<sub>4</sub>@C nanocomposites were also prepared and tested as LIB anodes (**Figure 3.18**).

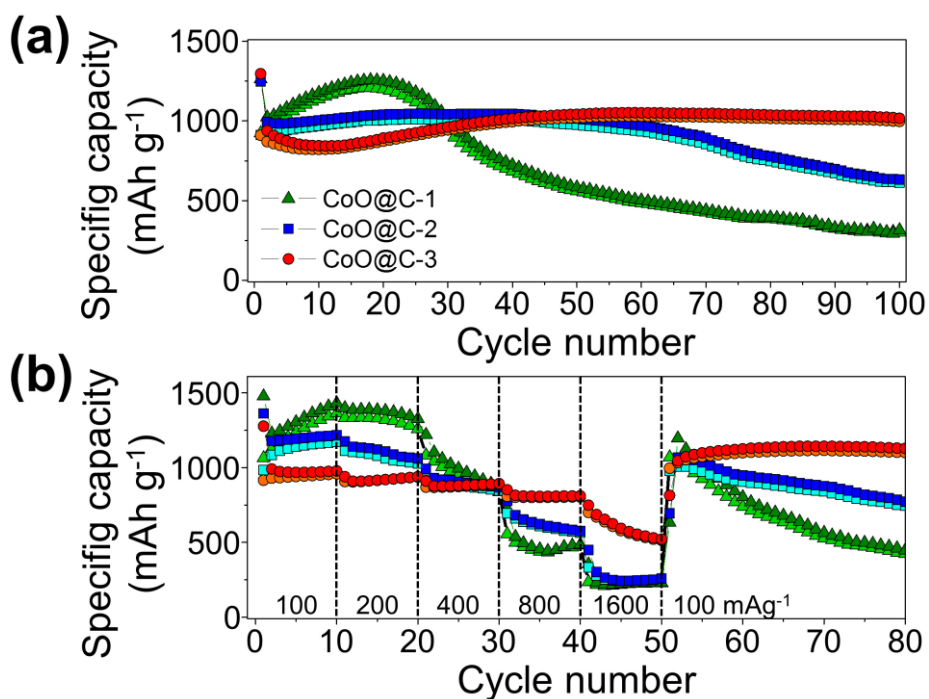


**Figure 3.16.** Electrochemical performance of CoO@C-1, CoO@C-2, and CoO@C-3. (a) Cycling performance at a current density of 200 mA g<sup>-1</sup>, and (b) rate performance at current densities from 100 to 1600 mA g<sup>-1</sup>.

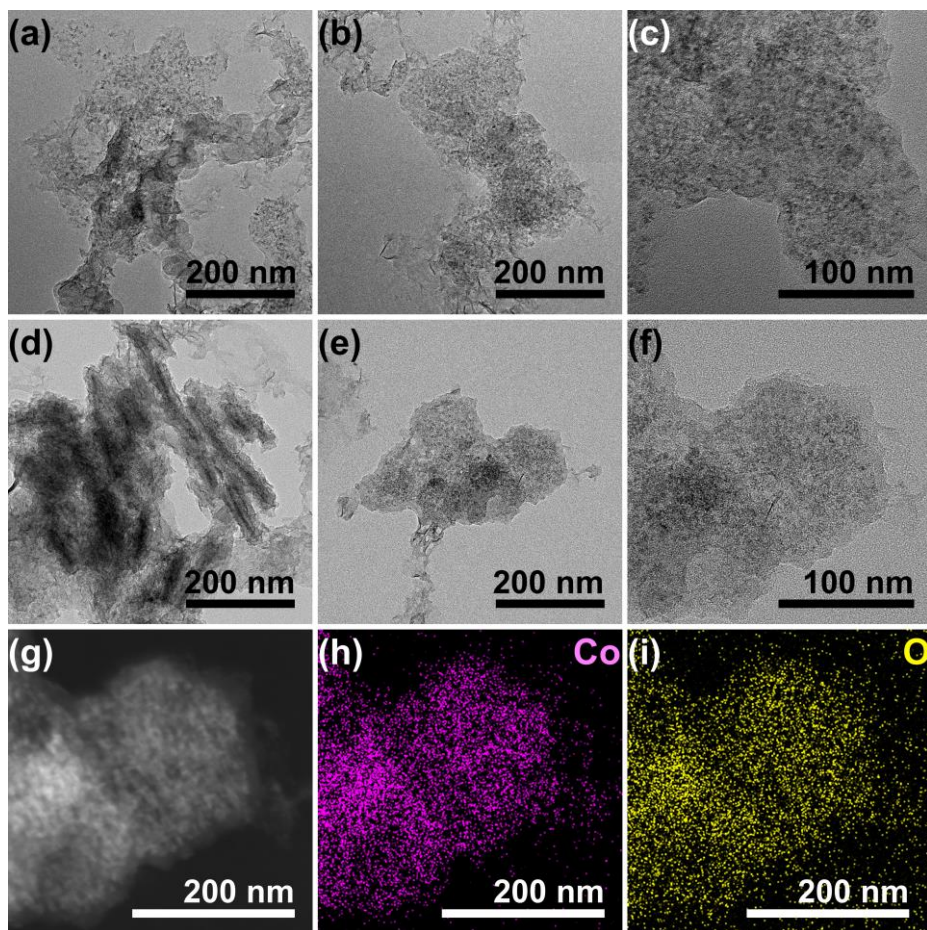


**Figure 3.17.** (a-f) TEM images of (a-c) CoO@C-1 and (d-f) CoO@C-3 after 50 cycles. (g) Dark-field STEM image and elemental mapping of (h) cobalt K edge and (i) oxygen K edge of CoO@C-3 after cycles.

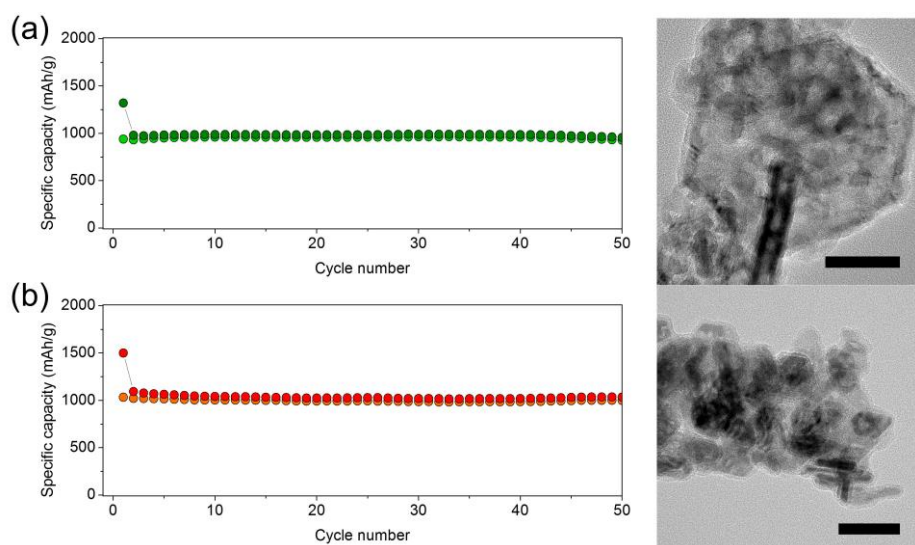


**Figure 3.18.** Cycling performance and TEM image of (a) MnO@C and (b) Fe<sub>3</sub>O<sub>4</sub>@C. Scale bars indicate 50 nm.

### 3.4. Conclusion

In conclusion, we developed a facile synthetic method for hexagon-shaped metal (oxy)hydroxide nanoplates under aqueous and mild condition without time- and energy-wasting reactions. It should be noted that this synthetic method can be generally applied to fabricate various nanoplates, including single-metallic (oxy)hydroxides ( $\text{Co}(\text{OH})_2$ ,  $\text{MnO}(\text{OH})$ ,  $\text{FeO}(\text{OH})$ , and  $\text{Mg}(\text{OH})_2$ ) and (oxy)hydroxides with two or more metal ions. Metal components were homogeneously distributed over the entire mixed-metal (oxy)hydroxide nanoplate, not forming separate nanoplates or heterogeneous nanostructures. This result was confirmed by TEM, EDS, XRD, and EFTEM. To use synthesized hexagon-shaped  $\text{Co}(\text{OH})_2$  nanoplates as the anode electrode of LIBs, polydopamine was coated on the nanoplates and  $\text{Co}(\text{OH})_2$ @polydopamine nanoplates were heated to obtain mesoporous  $\text{CoO@C}$  core-shell nanoplates. Owing to its straightforward chemistry, the thickness of the carbon shell was controlled from 1.5 nm to 6.5 nm or thicker, and the thickness-dependent electrochemical performance of  $\text{CoO@C}$  was evaluated.  $\text{CoO@C}$  with a 6.5-nm-thick carbon coating exhibited good cycling performance and a higher rechargeable capacity of 997



mAh g<sup>-1</sup> after 100 cycles at a current density of 200 mA g<sup>-1</sup>, while CoO@C with 1.5 nm-thick carbon shell only showed a capacity of 315 mAh g<sup>-1</sup> at the 100th cycle with poor cycling stability. TEM images taken after cycling also supported that there is a direct relationship between the thickness of the carbon layer and the morphological deformation of the core CoO. Since this synthesis method can be generally adaptable for various metals, such as cobalt, manganese, iron, magnesium, and mixed-metal (oxy)hydroxide nanoplates, it is expected that this synthesis can be used for many energy storage/conversion applications including supercapacitors, batteries, and electrochemical catalysts.

### 3.5. Reference

- [1] V. Aravindan, Y.-S. Lee, S. Madhavi, *Adv. Energy Mater.* **2015**, 5, 1402225.
- [2] A. Kraytsberg, Y. Ein-Eli, *Adv. Energy Mater.* **2012**, 2, 922.
- [3] M. V. Reddy, G. V. Subba Rao, B. V. Chowdari, *Chem. Rev.* **2013**, 113, 5364.
- [4] L. Ji, Z. Lin, M. Alcoutlabi, X. Zhang, *Energy Environ. Sci.* **2011**, 4, 2682.
- [5] S. Goriparti, E. Miele, F. De Angelis, E. Di Fabrizio, R. Proietti Zaccaria, C. Capiglia, *J. Power Sources* **2014**, 257, 421.
- [6] H. B. Wu, J. S. Chen, H. H. Hng, X. W. Lou, *Nanoscale* **2012**, 4, 2526.
- [7] M. Armand, J. M. Tarascon, *Nature* **2008**, 451, 652.
- [8] N. Nitta, G. Yushin, *Part. Part. Syst. Charact* **2014**, 31, 317.
- [9] J. Cabana, L. Monconduit, D. Larcher, M. R. Palacin, *Adv. Mater.* **2010**, 22, E170.
- [10] P. Poizot, S. Laruelle, S. Grugeon, L. Dupont, J. M. Tarascon, *Nature* **2000**, 407, 496.
- [11] R. Malini, U. Uma, T. Sheela, M. Ganesan, N. G. Renganathan, *Ionics* **2008**, 15, 301.
- [12] L. Zhang, G. Zhang, H. B. Wu, L. Yu, X. W. Lou, *Adv. Mater.* **2013**, 25,

2589.

- [13] W.-M. Zhang, X.-L. Wu, J.-S. Hu, Y.-G. Guo, L.-J. Wan, *Adv. Funct. Mater.* **2008**, *18*, 3941.
- [14] X. W. Lou, C. M. Li, L. A. Archer, *Adv. Mater.* **2009**, *21*, 2536.
- [15] X. W. Lou, J. S. Chen, P. Chen, L. A. Archer, *Chem. Mater.* **2009**, *21*, 2868.
- [16] J. E. Lee, S.-H. Yu, D. J. Lee, D.-C. Lee, S. I. Han, Y.-E. Sung, T. Hyeon, *Energy Environ. Sci.* **2012**, *5*, 9528.
- [17] Y. Chen, M. Zhuo, J. Deng, Z. Xu, Q. Li, T. Wang, *J. Mater. Chem. A* **2014**, *2*, 4449.
- [18] X. Zhang, Z. Xing, L. Wang, Y. Zhu, Q. Li, J. Liang, Y. Yu, T. Huang, K. Tang, Y. Qian, X. Shen, *J. Mater. Chem.* **2012**, *22*, 17864.
- [19] C. Nethravathi, C. R. Rajamathi, M. Rajamathi, X. Wang, U. K. Gautam, D. Golberg, Y. Bando, *ACS Nano* **2014**, *8*, 2755.
- [20] Y. L. Hou, H. Kondoh, M. Shimojo, T. Kogure, T. Ohta, *J. Phys. Chem. B* **2005**, *109*, 19094.
- [21] W. Yao, J. Yang, J. Wang, Y. Nuli, *J. Electrochem. Soc.* **2008**, *155*, A903.
- [22] D. Su, M. Ford, G. Wang, *Sci. Rep.* **2012**, *2*, 924.
- [23] D. Su, X. Xie, P. Munroe, S. Dou, G. Wang, *Sci. Rep.* **2014**, *4*, 6519.

- [24] P. Li, D. Wang, Q. Peng, Y. Li, *Cryst. Growth Des.* **2013**, *13*, 1949.
- [25] Y. Piao, H. S. Kim, Y. E. Sung, T. Hyeon, *Chem. Commun.* **2010**, *46*, 118.
- [26] X. Gu, J. Yue, L. Chen, S. Liu, H. Xu, J. Yang, Y. Qian, X. Zhao, *J. Mater. Chem. A* **2015**, *3*, 1037.
- [27] L. Yu, S. Xi, C. Wei, W. Zhang, Y. Du, Q. Yan, Z. Xu, *Adv. Energy Mater.* **2015**, *5*, 1401517.
- [28] S. Gao, Y. Sun, F. Lei, L. Liang, J. Liu, W. Bi, B. Pan, Y. Xie, *Angew. Chem. Int. Ed.* **2014**, *53*, 12789.
- [29] X. Li, S. Xiong, J. Li, J. Bai, Y. Qian, *J. Mater. Chem.* **2012**, *22*, 14276.
- [30] C. Yuan, X. Zhang, L. Hou, L. Shen, D. Li, F. Zhang, C. Fan, J. Li, *J. Mater. Chem.* **2010**, *20*, 10809.
- [31] M. S. Burke, M. G. Kast, L. Trotochaud, A. M. Smith, S. W. Boettcher, *J. Am. Chem. Soc.* **2015**, *137*, 3638.
- [32] M. Gong, Y. Li, H. Wang, Y. Liang, J. Z. Wu, J. Zhou, J. Wang, T. Regier, F. Wei, H. Dai, *J. Am. Chem. Soc.* **2013**, *135*, 8452.
- [33] C. G. Silva, Y. Bouizi, V. Fornes, H. Garcia, *J. Am. Chem. Soc.* **2009**, *131*, 13833.
- [34] K. Y. Niu, F. Lin, S. Jung, L. Fang, D. Nordlund, C. C. McCrory, T. C. Weng, P. Ercius, M. M. Doeff, H. Zheng, *Nano Lett.* **2015**, *15*, 2498.

- [35] J. Jiang, J. Liu, R. Ding, J. Zhu, Y. Li, A. Hu, X. Li, X. Huang, *ACS Appl. Mater. Interfaces* **2011**, 3, 99.
- [36] S. Xiong, J. S. Chen, X. W. Lou, H. C. Zeng, *Adv. Funct. Mater.* **2012**, 22, 861.
- [37] Z. Lu, Z. Chang, W. Zhu, X. Sun, *Chem. Commun.* **2011**, 47, 9651.
- [38] X. Su, Y. Xu, J. Liu, R. Wang, *CrystEngComm* **2015**, 17, 4859.
- [39] J. Wu, H. Zhang, N. Du, X. Ma, D. Yang, *J. Phys. Chem. B* **2006**, 110, 11196.
- [40] J. C. Yu, A. W. Xu, L. Z. Zhang, R. Q. Song, L. Wu, *J. Phys. Chem. B* **2004**, 108, 64.
- [41] L. Chen, X. Yang, J. Chen, J. Liu, H. Wu, H. Zhan, C. Liang, M. Wu, *Inorg. Chem.* **2010**, 49, 8411.
- [42] D. Liu, B. B. Garcia, Q. Zhang, Q. Guo, Y. Zhang, S. Sepehri, G. Cao, *Adv. Funct. Mater.* **2009**, 19, 1015.
- [43] E. R. Encina, M. Distaso, R. N. Klupp Taylor, W. Peukert, *Cryst. Growth Des.* **2015**, 15, 194.
- [44] X. Li, L. Zhou, J. Gao, H. Miao, H. Zhang, J. Xu, *Powder Technol.* **2009**, 190, 324.
- [45] H. Lee, S. M. Dellatore, W. M. Miller, P. B. Messersmith, *Science* **2007**, 318, 426.

- [46] Y. Liu, K. Ai, L. Lu, *Chem. Rev.* **2014**, *114*, 5057.
- [47] J. Wang, G. Du, R. Zeng, B. Niu, Z. Chen, Z. Guo, S. Dou,  
*Electrochim. Acta* **2010**, *55*, 4805.
- [48] G. Wang, H. Liu, J. Horvat, B. Wang, S. Qiao, J. Park, H. Ahn, *Chem.*  
*Eur. J.* **2010**, *16*, 11020.



# Bibliography

## 1. Journal Publications

1) Donghee Son, Jongha Lee, **Dong Jun Lee** (*co-first author*), Roozbeh Ghaffari, Sumin Yun, Seok Joo Kim, Ji Eun Lee, Hye Rim Cho, Soonho Yoon, Shixuan Yang, Seunghyun Lee, Shutao Qiao, Daishun Ling, Sanghun Shin, Jun-Kyul Song, Jaemin Kim, Taeho Kim, Hakyong Lee, Jonghoon Kim, Min Soh, Nohyun Lee, Cheol Seong Hwang, Sangwook Nam, Nanshu Lu, Taeghwan Hyeon, Seung Hong Choi, and Dae-Hyeong Kim  
“Bioresorbable Electronic Stent Integrated with Therapeutic Nanoparticles for Endovascular Diseases”  
*ACS Nano*, **2015**, 9, 5937-5946.

2) Seung-Ho Yu, **Dong Jun Lee** (*co-first author*), Mihyun Park, Soon Gu Kwon, Hyeon Seok Lee, Aihua Jin, Kug-Seung Lee, Ji Eun Lee, Myoung Hwan Oh, Kisuk Kang, Yung-Eun Sung, and Taeghwan Hyeon  
“Hybrid Cellular Nanosheets for High-Performance Lithium Ion Battery Anodes”  
*Journal of the American Chemical Society*, **2015**, 137, 11954-



11961

3) Seung-Ho Yu, Soo Hong Lee, **Dong Jun Lee** (*co-first author*),  
Yung-Eun Sung, and Taeghwan Hyeon

“Conversion Reaction-Based Oxide Nanomaterials for Lithium  
Ion Battery Anodes”

*Small*, DOI:10.1002/sml.201502299

4) Ji Eun Lee, **Dong Jun Lee**, Nohyun Lee, Byung Hyo Kim,  
Seung Hong Choi, and Taeghwan Hyeon

“Multifunctional Mesoporous Silica Nanocomposite  
Nanoparticles for pH Controlled Drug Release and Dual Modal  
Imaging”

*Journal of Material Science*, **2011**, *21*, 16869-16872

5) Ji Eun Lee, Seung-Ho Yu, **Dong Jun Lee**, Dong-Chan Lee,  
Sang Ihn Han, Yung-Eun Sung and Taeghwan Hyeon

“Facile and Economical Synthesis of Hierarchical Carbon-coated  
Magnetite Nanocomposite Particles and their Applications in  
Lithium Ion Battery Anodes”

*Energy & Environmental Science*, **2012**, 5, 9528-9533

6) Samuel Woojoo Jun, Mohammadreza Shokouhimehr, **Dong Jun Lee**, Youngjin Jang, Jinkyung Park and Taeghwan Hyeon

“One-pot Synthesis of Magnetically Recyclable Mesoporous Silica Supported Acid-base Catalysts for Tandem Reactions”

*Chemical Communications*, **2013**, 49, 7821-7823

7) Soo Hong Lee, Seung-Ho Yu, Ji Eun Lee, Aihua Jin, **Dong Jun Lee**, Nohyun Lee, Hyungyung Jo, Kwangsoo Shin, Tae-Young Ahn, Young-Woon Kim, Heeman Choe, Yung-Eun Sung, and Taeghwan Hyeon

“Self-Assembled Fe<sub>3</sub>O<sub>4</sub> Nanoparticle Clusters as High Performance Anodes for Lithium-Ion Batteries via Geometric Confinement”

*Nano Letters*, **2013**, 13, 4249-4256

8) Donghee Son, Jongha Lee, Shutao Qiao, Roozbeh Ghaffari, Jaemin Kim, Ji Eun Lee, Changyeong Song, Seok Joo Kim, **Dong Jun Lee**, Samuel Woojoo Jun, Shixuan Yang, Minjoon Park, Jiho

Shin, Kyungsik Do, Mincheol Lee, Kwanghun Kang, Cheol Seong Hwang, Nanshu Lu, Taeghwan Hyeon, and Dae-Hyeong Kim

“Multifunctional Wearable Devices for Diagnosis and Therapy of Movement Disorders”

*Nature Nanotechnology*, **2014**, 9, 397-404

9) Sumin Lim, Donghee Son, Jaemin Kim, Young Bum Lee, Jun-Kyul Song, Suji Choi, **Dong Jun Lee**, Ji Hoon Kim, Minbaek Lee, Taeghwan Hyeon, and Dae-Hyeong Kim

“Transparent and Stretchable Interactive Human Machine Interface Based on Patterned Graphene Heterostructures”

*Advanced Functional Materials*, **2015**, 25, 375-383

10) Moon Kee Choi, Ok Kyu Park, Changsoon Choi, Shutao Qiao, Roozbeh Ghaffari, Jaemin Kim, **Dong Jun Lee**, Myungbin Kim, Wonji Hyun, Seok Joo Kim, Hye Jin Hwang, Seung-Hae Kwon, Taeghwan Hyeon, Nanshu Lu, and Dae-Hyeong Kim

“Cephalopod-Inspired Miniaturized Suction Cups for Smart Medical Skin”

*Advanced Healthcare Materials*, **2016**, 5, 80-87

11) Jaemin Kim, Donghee Son, Mincheol Lee, Changyeong Song, Jun-Kyul Song, Ja Hoon Koo, **Dong Jun Lee**, Hyung Joon Shim, Ji Hoon Kim, Minbaek Lee, Taeghwan Hyeon and Dae-Hyeong Kim

“A Wearable Multiplexed Silicon Nonvolatile Memory Array using Nanocrystal Charge Confinement”

*Science Advances*, **2016**, 2, e1501101

## **2. International Conference Presentations**

1) **Dong Jun Lee**, Donghee Son, Jongha Lee, Dae-Hyeong Kim, and Taeghwan Hyeon

“Bioresorbable smart stent incorporated with therapeutic nanoparticles for endovascular diseases”

250th American Chemical Society National Meeting & Exposition,  
Boston Convention & Exhibition Center, Boston, Massachusetts,  
USA, August 16-20, 2015

2) **Dong Jun Lee**, Donghee Son, Jongha Lee, Jonghoon Kim, Dae-Hyeong Kim, and Taeghwan Hyeon

“Biodegradable Stent Integrated with Therapeutic Nanoparticles

and Electronic devices for Endovascular Diseases”

45th IUPAC World Chemistry Congress (IUPAC-2015), BEXCO,  
Busan, Korea, August 9-14, 2015

3) **Dong Jun Lee**, Seung-Ho Yu, Yung-Eun Sung, and Taeghwan  
Hyeon

“Hybrid Cellular Nanosheets for High-Performance Anode  
Materials of Lithium Ion Battery”

The 9th International Conference on Advanced Materials and  
Device (ICAMD 2015), Ramada Plaxza Hotel, Jeju, Korea,  
December 7-9, 2015

### **3. Domestic Conference Presentations**

1) **Dong Jun Lee**, Ji Eun Lee, Seung-Ho Yu, Dong-Chan Lee,  
Sang Ihn Han, Yung-Eun Sung, and Taeghwan Hyeon

“Facile and Economical Synthesis of Hierarchical Carbon-coated  
Magnetite Nanocomposite Particles and their Applications to  
Lithium Ion Battery Anodes”

NANO KOREA 2013 Symposium, COEX, Seoul, Korea, July 10-  
12, 2013

## 초 록

최근 전기 자동차 시장을 포함한 다양한 산업분야에서 차세대 리튬 이온전지에 대한 수요가 급증하고 있다. 이를 해결하기 위해서는 더 높은 에너지 밀도를 가지고 향상된 안정성을 가지는 리튬 이온전지용 전극재료의 개발이 필수적이다. 전이금속 산화물, 실리콘, 주석, 산화주석 등의 고용량 음극 재료는 충방전동안 큰 부피 변화를 동반하는데, 이를 억제하는 것이 고성능 음극재료를 개발하는데 있어 중요하다. 실질적인 상업화를 위해 손쉽고 대용량화가 가능한 합성법의 개발 역시 고려되어야 한다. 이 학위 논문에서는 부피 변화에 의한 전극 변화를 효과적으로 억제하는 기능성 하이브리드 나노물질의 합성에 관하여 기술한다.

먼저, 리튬 이온전지 음극재료로써 다방면에서 뛰어난 성능을 보이는, 탄소 나노시트와 산화주석 나노입자로 구성된 하이브리드 나노시트를 개발하였다. 탄소 나노시트는 입방체 모양의 빈칸이 정렬된 형태를 가지는데, 각각의 빈칸은 탄소벽에 의해 분리되어 있다. 추가적인 자기조립 과정 없이 정렬구조를 제조할 수 있다는 점에서 여러 분야로 응용함에

이점을 가진다. “쉽-인-어-보틀” 합성법을 통해 빈칸의 내부에 무기물 나노입자를 도입하였다. 충방전동안 산화주석의 부피팽창이 하이브리드 나노시트의 빈칸 내부에만 국한되기 때문에 전극의 전체적인 물리적 특성이 유지되고, 뛰어난 충방전 안정성과 고속충방전 성능을 나타내는데, 이는 넓고 얇은 카본시트의 그 구조적인 특징 때문이다.

다음으로 간단하고 방법을 이용한 육각형 모양을 가지는 단일금속 및 다금속 수산화물 나노판의 합성을 개발하였다. 이를 리튬 이온전지 음극재료로 응용하기 위해, 도파민수지를 나노판 표면에 코팅하고 열처리를 통해 다공성 산화코발트-탄소 핵-껍질 나노판을 합성하는데 성공하였다. 탄소코팅 두께에 따른 전기화학적 성능 평가를 통하여 전지성능 향상에 있어 일정량의 탄소코팅이 필수적이라는 결과를 얻을 수 있었다. 뿐만 아니라, 금속 수산화물 나노판이 다른 에너지 저장/변환물질로 응용될 것이라 기대할 수 있다.

**주요어:** 리튬 이온 전지, 음극 재료, 나노복합체, 금속 산화물 나노입자, 에너지 저장.

**학번:** 2009-21011